Evaluation of velocity interferometry for high energetic materials using a VISAR

by

Athernia Nomahlubi Thunyiswa

Submitted in partial fulfilment of the requirements for degree of

MAGISTER SCIENTIAE

In the Faculty of Natural & Agriculture Sciences

University of Pretoria

Pretoria

February 2020

Declaration

I, Athernia Nomahlubi Thunyiswa declare that the dissertation, which I hereby submit for the degree of MSc Physics at the university of Pretoria, is my own work and has not previously been submitted by me for a degree at this or any other tertiary institution.

SIGNATURE: ……..

DATE: ……..

Abstract

In this study, a cylinder expansion test was performed using a square prism OFHC copper with a cylindrical extrusion filled with Comp B explosive charge. A Valyn VISAR was used as a measuring tool to record the expansion history of the cylinder by Doppler shift of the light reflected off its surface, which subsequently was used to obtain the velocity history of the square prism cylinder.

Quadrature fringe signals obtained from the square prism cylinder test were analysed using the results still showing some traces of fringe jumps. Whereas the hands-on calculations were more precise in correcting the jumps. This introduced some shifts in the velocity results VISAR Push-Pull reduction software and hands-on calculations. The outcome of the two velocity graphs (reduction software and manual) did not correspond. This might be due to the software velocity which caused the variation in the two velocity results. Overall, both software and manual methods resulted in velocity values that were difficult to draw conclusions from.

In an attempt to further understand the test results, the displacement curve were also reduced from the velocity graphs. Although the trend of the displacement graph obtained from the reduction software is comparable to the displacement graph published in literature for the same test, the magnitudes of the values are still difficult to explain.

The cylinder design used in this study was tested for the first time and numerous challenges rose up during setup and execution and are discussed. It is important for another test to be conducted with an improved setup in order to achieve a reliable interpretation of the cylinder test results.

Aknowledgement

I would like to express my deep gratitude to Professor Chris Theron and Dr Bathusile Masina, my research supervisors, for their enthusiastic encouragement, advice and assistance on my schedule, patient guidance and constructive criticism during the course of this research work. Both my supervisors were always there in every aspect of this research. I would not have asked for better supervision.

I would like to also thank Mr Conrad Mahlase for his valuable support, useful and constructive recommendations on this research. Conrad has also supported me with my CSIR contract, I sincerely appreciate his support. Thank you to Dr Frikkie Mostert for his support and constructive inputs to my project.

I salute the CSIR Landward Sciences for supporting this research; my colleagues for their encouragement, patience and technical support. Thank you to the scientist, engineers and technicians at the CSIR Landward science, CSIR DBEL testing range and National Laser Cenre who were involved during the test for my project. From proving the concept in the laboratory, designing the equipments to the execution of the test. It was not an easy task, I am truly grateful for their support. I wish to thank Mr Zane Barker of Valyn Inc for his support in the experiment part of this project. I also extend my gratitude to Mr Denis Lafont of DGA Terrestrial Techniques for sharing his knowledge of the VISAR system with my team.

I would like to thank Dr Ajith Gopal, Dr Tleyane Sono and the CSIR studentship office for giving me the opportunity of doing an MSc while working and for the financial support for my project. I felt quite priviledged.

Finally, I would like to express my gratitude to my family and friends. I dedicate this study to my mother who always uses me as a point of reference when encouraging my niblings to prioratize education. Foremost, I would like to thank God for the wisdom and strength He gave me throughout the course of this study.

Contents

List of figures

List of tables

List of abbreviations

.WFM	file extension for Tektronix files
AMBS/FC	adjustable multi-beam splitter and fibre coupler
AMO	amplified monitoring oscilloscope
BIM	beam intensity Monitor
BK 7	borosilicate crown optical glass
BKW	Beker-Kistiakowsky-Wilson
BNC	Boyonet Neil Concelman
CJ	Chapman Joguet
CAD	computer aided drawing
CSIR	council for scientific and industrial research
Cu	copper
CW	continuous wave
DBEL	detonics, ballistics and explosives laboratory
EOS	equation of state
FPI	Fabry Perot interferometer
IED	improvised explosive device
JCZ	Jacobs-Cowperthwaite- Zwisler
JWL	Jones Wilkins-Lee
LJD	Lennard-Jones-Devonshire

LLNL	Lawrence Livermore National Laboratory
MZI	Mach Zehnder interferometer
OFHC	oxygen free high conductivity
PDV	photo Doppler velocimeter
PMT	photomultiplier tube
POD-4	housing unit for four PMTs
PVC	polyvinyl chloride
PZAT	piezoelectric translator/aligner
RDX	preferred IUPAC name “1,3,5-Trinitro-1,3,5-triazinane” (popular known as royal demolition eXplosive)
ST	straight tip
SNR	signal to noise ratio
TNT	trinitrololuene (preferred IUPAC name 2,4,6-Trinitrotoluene)
UHSC	utral high speed camera
UNBP	ultra-narrow bandpass
VISAR	velocity interferometer system for any reflector
VOD	velocity of detonation
VPF	velocity per fringe
WAMI	wild angle michelson interferometer

List of symbols and units

ε	quadrature error
Ω	unit for load resistance (ohm)
π	180 degrees in radians
ϕ	phase angle
µs	microseconds
ms	milliseconds
kHz	kilohertz
g	grams
mm	millimetres
s	seconds
GHz/S	gigahertz per sample
MHz/S	megahertz per sample
MS/s	megasamples per second
S	sample
mV	millivolts
W	watt

Chapter 1

Introduction and Background

1.1. Introduction

In a variety of instances, explosive weapons are used in populated areas in terror campaigns to cause death and injury to civilians. Hence, more active and effective human responses are needed to enhance civilian protection. Amongst the explosive weapons, there are Improvised Explosive Devices (IEDs). An IED is a homemade device used to destroy, incapacitate, harass and destruct[1]. IEDs come in various sizes ranging from the size of a food tin to the size of gas tanks. These are easily transported from point to point with low risk of detection in the civilian environment. Figure 1.1 shows that the most prevailing IED attacks occur on the roads[2], presenting a real risk to civilians.

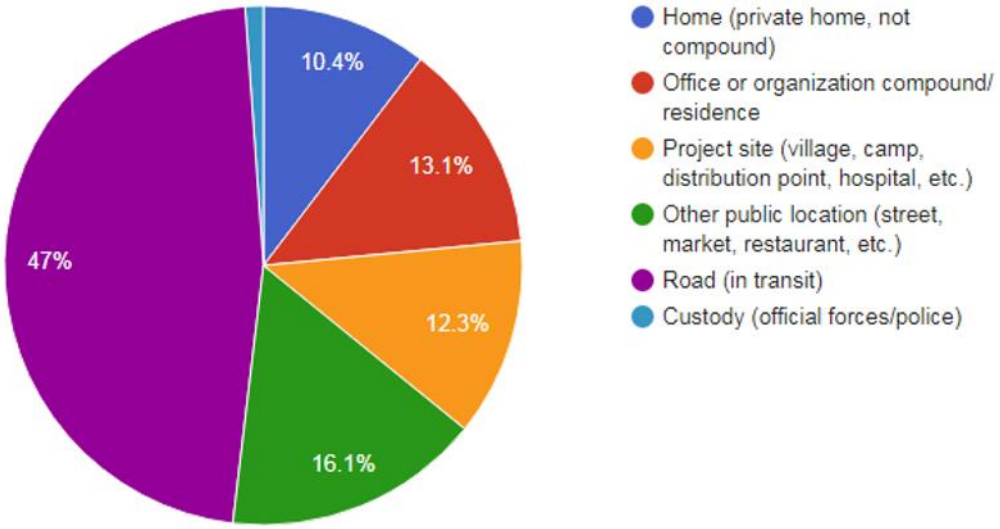

Figure 1.1: " Location of attacks (1997-2017)"[3]

As shown in Figure 1.2 during the years 2011 to 2015 the use of explosives as a weapon increased, with 25 explosives used in the year 2013. Between 2011 and 2013, about 4300 IED events led to an estimated 65 400 number of casualties recorded in 66 countries (Wilkinson, Turns et al. 2017). In 2017 the recorded number of major incidents against humanitarian operations was 158 which affected 313 aid workers in 22 countries[4].

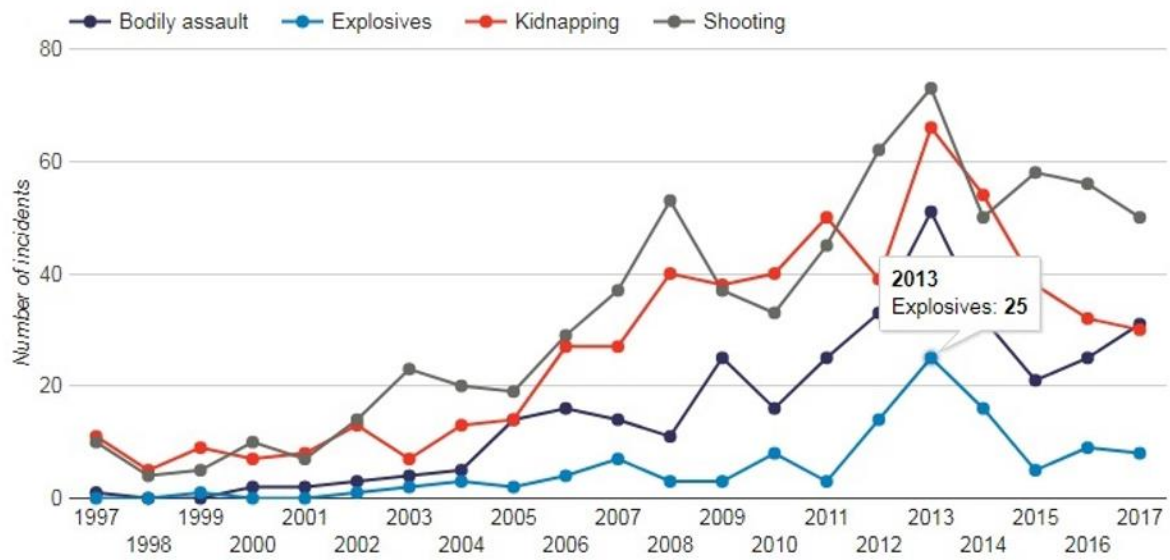

Figure 1.2: "Trends in tactics (1997-2017)"[4]

The destructive effects from IED incidences such as primary blast injuries e.g. disruption of human tissue, traumatic amputations, and collapse of buildings are caused by the shock wave which is produced in the surrounding. Explosive devices do not only damage the human body but also damage property and public infrastructure. Secondary injuries are caused by the fragments and other objects erupting from the explosion. Many commonly available materials, such as fertilizer, gunpowder, and hydrogen peroxide, can be used in conjuction with other explosive materials in IEDs. The commercial availability of the materials has led to an increase of IEDs as the weapon of choice[2]. In order to combat the scourge of these devices, reliable and quantitative methodologies are required to investigate the underlying technology used to create these devices.

An essential facet of this methodology is the ability to determine the equation of state (EOS) of existing and new energetic materials. This EOS is essential for the prediction of their performance. However, quantification of the EOS is no easy feat because the theoretical modelling of energetic materials is complex due to the extreme thermodynamic and chemical environment during and after detonation. The Council for Scientific and Industrial Research (CSIR) Landward Sciences use commercial software packages such as Ansys Autodyn, LS Dyna and EXPLO 5 computer codes for modelling explosive material and calculate detonation parameters[5,6] . The modelling of explosive material in these software packages relies on the EOS to define the relationship among the state parameters for the explosive. There are several EOS in use such as polytropic gas law equation, Lennard-Jones-Devonshire (LJD), Beker-

Kistiakowsky-Wilson (BKW), Jacobs-Cowperthwaite- Zwisler (JCZ) and Jones-Wilkins-Lee (JWL). The JWL EOS is more common in the hydrodynamic calculation domain than the other EOS because of its simplicity, relative accuracy and availability of data for most significant explosives[7]. The JWL EOS describes the relationship between the volume, pressure and energy of detonation products[7,8]. The parameters for the EOS are obtained from the cylinder expansion test[8,9]. The Lawrence Livermore National Laboratory (LLNL) is known for being the innovator of the cylinder expansion test in the world.

The cylinder test utilises an Oxygen Free High Conductivity (OFHC) copper tube, also refered to as a cylinder, confining an explosive material. The cylinder is normally 300 mm long with inner diameter of 25 mm[10–12]. The normal procedure for recording the expansion characteristics of the cylinder is that the tube is planar initiated at one end while a rotating mirror camera records the expansion via streak photography at a slit in the horizontal plane approximately 200 mm from the initiation end. The streak speed of the camera is typically in the range of 2 mm/μs to yield high spatial and temporal accuracy over the approximately 20-50 μs time duration of the event. The test is also normally performed in a helium atmosphere to reduce shock refractions.

Analysis of the wall position of the cylinder is typically attained from 500 data points and the data is fitted with a high order polynomials or specific functions. The data is complicated by the fact that the early acceleration of tube is driven by successive compression and reflective shocks and the motion is also affected by non-uniform pull-back. Due to the fact that the position data is differentiated to obtain velocity and twice differentiated to obtain acceleration, it is vital to obtain accurate recordings of the position with time during the expansion procedure.

1.2. Motivation for this study

At the CSIR DBEL testing facility, the standard infrastructure includes a Cordin ultra high speed camera (UHSC) instead of a streak photography capability. The Cordin UHSC is capable of producing framing records of up to 2 Mfps, but with a restricted number of frames (20-30) at maximum frame rate. This Cordin UHSC is mainly used to record the expanding cylinder wall during a cylinder excpansion test. The cylinder test has been perfomed only in open air. In principle, the expansion of the cylinder can be captured at different positions and time within the range of the frames and then used in a fitting routine to deduce the continuous motion of the cylinder wall. However, the accuracy of the results obtained by the Cordin UHSC becomes unsatisfactory since only 20-30 data points are obtained in comparison to the standard 500 data

points usually obtained with the streak facilitated test[13]. Furthermore, the method of extracting expansion data from the images captured by the Cordin camera is tedious and is likely to have human errors.

Therefore it is important to investigate an alternative method to UHSC. The proposed instrument, Velocity Interferometer System for Any Reflector (VISAR), gives direct velocity results, thus no differentiation of position data is required. Direct velocity measurements play an important role in dynamic compression research because it enables the determination of mechanical parameters for materials under extreme conditions when mass and momentum conservation are taken in consideration[14]. This method simplifies the experimental operation, and also reduces the system error among measured points. The VISAR can be used to measure short duration shock wave and high speed motion produced by explosives[15]. In the field of terminal ballistics, the VISAR has shown potential through four examples: 1) impact of a steel rod against a steel target plate 2) in-bore acceleration of a projectile in a two stage light gas gun 3) expansion of high explosive loaded cylinder 4) hypervelocity impact of a steel ball against an aluminium target[16].

Hence, the main aim of this study is to develop a cylinder expansion test setup that will utilize a VISAR to observe and measure the radial wall expansion and register its velocity. This approach is not new and has been previously suggested by[17] that it can measure the wall velocity of the expanding cylinder. The recorded data can later be used to determine the JWL EOS parameters. The cylinder expansion test setup is designed with the knowledge gained from many years of doing the test at the CSIR and from literature survey.

1.3. Problem statement

The goal is to investigate the use of the VISAR as measuring tool during a cylinder expansion test in order to extract the JWL EOS parameters from the measured results for different explosive compositions. The objective is to validate if the currently available VISAR tool can be effectively implemented as an alternative to the UHSC method. The application will help the CSIR in analysing the data from the same test in a much faster and easier way than in previous years.

The research hereby proposed seeks to:

- describe the theory and methodology of direct velocity measurements;
- demonstrate calculation of velocity data from experiments;

- and investigate the feasibility of the VISAR measurement at CSIR DBEL testing facility.

1.4. Dissertation outline

The chapters in this dissertation are organized as follows:

In Chapter 2, we give an overview of the cylinder expansion test, the method of obtaining the JWL parameters from the cylinder test is discussed and formula involved are presented. Chapter 3 gives a discussion on the optical velocimetry techniques that have taken over high-speed photography. In this chapter, the discussion of the VISAR is lengthened since it is the technique being used in the study. Chapter 4, presents the design of the cylinder expansion test setup and the components used in the design are explained. The laboratory and field setups are discussed including challenges that came forth with the setups. Some important steps followed during the execution of the experiment are also discussed in this section including the operation of the VISAR. In this Chapter 5, test results from the cylinder test are presented in graphs and are discussed and the methods used to analyse the experimental results are presented. Chapter 6, the last chapter, gives a general summary and presents the conclusion of the study. Recommendations of possible future work are also given.

Chapter 2

Cylinder test and JWL parameters

2.1. Introduction

In this section the cylinder expansion test is overviewed and the parametric dynamics to obtain the JWL EOS parameters from the experimental results of the cylinder test are discussed. The optical velocity interferometer techniques utilized to measure the expansion are presented in detail.

2.2. The cylinder test

The cylinder expansion test is a technique that measures the relative performance of an explosive, material deformation and at what speed the detonation products expand a confining material[18,19]. LLNL is reported to have discovered the cylinder expansion test around 1960 and developed the standard used today by 1965[20]. The cylinder expansion test is the source to a great percentage of practical and reliable information about explosives; Gurney velocities, Taylor angles and detonation velocities can all be assumed from cylinder expansion test data[12,21]. Furthermore, the cylinder test is the only test performed that measures detonation densities while the detonation is in progression[22]. According to Polk, it is among the classic experimental tools in research that are related to detonation dynamics[21].

Cylinder expansion tests consist of a high explosive casted inside an open ended copper tube[23]. The most used copper tube during experiments has geometries; 305 mm length, an outer diameter of 25.4 mm and wall thickness of 2.6 mm as shown schematically in Figure 2.1[8]. These geometries provide enough distance for the shock wave to run to a steady state. In addition, the geometries allow enough time (approximately 15μs) to complete wall motion measurement before the shock wave reaches the end of the cylinder[17].

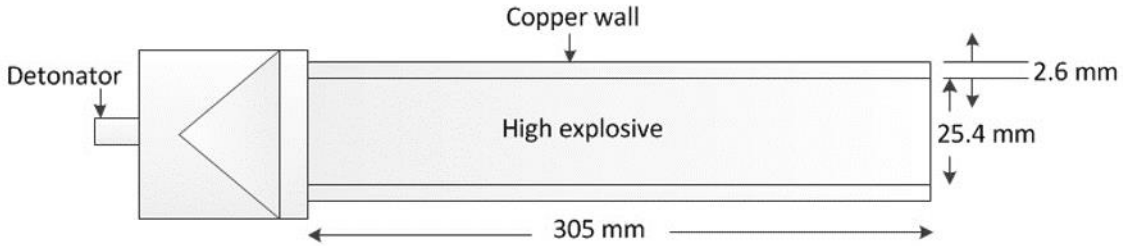

Figure 2.1: Standard experimental geometries of the cylinder test[8,10]

At 210 mm position from the point of detonation of the main charge, it is where the wall expansion is commonly observed because at this position the shock wave has reached its steady state[23]. There are also other examples of geometries that literature shows for the cylinder expansion tests. The copper tubes can also have cross-sections, from miniaturized diameters of 12.5 mm with approximately 100-120 mm lengths to larger diameters of 76.2 mm with 400 mm length and 110 mm diameter cylinders have also been tested[24]. The type of material of the standard cylinder used is an OFHC copper[9,10]. The OFHC is used because of its ductility and to avoid the spallation of the copper wall during the experiment[17]. The explosion is normally initiated at one end of the cylinder, e.g. at the top as shown in Figure 2.2, then the cylinder expands radially as the detonation wave progresses inside[23].

Figure 2.2: Photograph of a typical set cylinder. In this case a recording instrument is a Photon Doppler Velocimeter (PDV) with an optical probe as a light launching tool[25]

In cases where the cylinder expansion is determined through optical imaging, detonation wave passes through the observed segment, the cylinder wall expands outwardly and obscures backlighting provided by an artificial light source such as an argon bomb (an inflated transparent plastic bag filled with argon gas that is activated by the detonation of a secondary charge)[8,10]. The argon bomb allows the shadowgraph, an example shown in Figure 2.3, from the main explosion event to be captured without influence of the self-luminosity from the event.

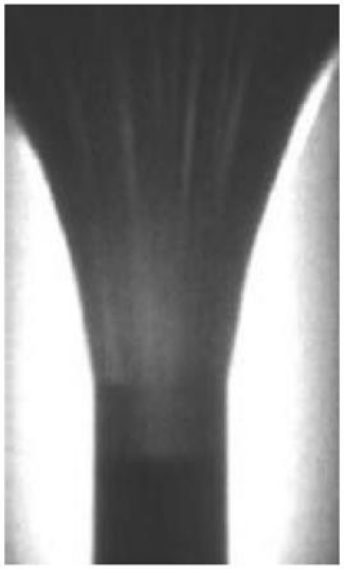

Figure 2.3: Streak camera record captured from a cylinder expansion test[26]

A sensitive explosive drives the argon bomb to ionize the gas inside the bag, eventually produce light. The intensity of the output light is sufficient enough to overpower the intensity of self-luminosity from the the main event[27,28]. This also implies that the time for the main event must suggest an effective lighting time for the argon bomb[5]. Figure 2.4 show a schematic of a typical setup of the entire cylinder expansion test with an optical imaging system and an argon bomb.

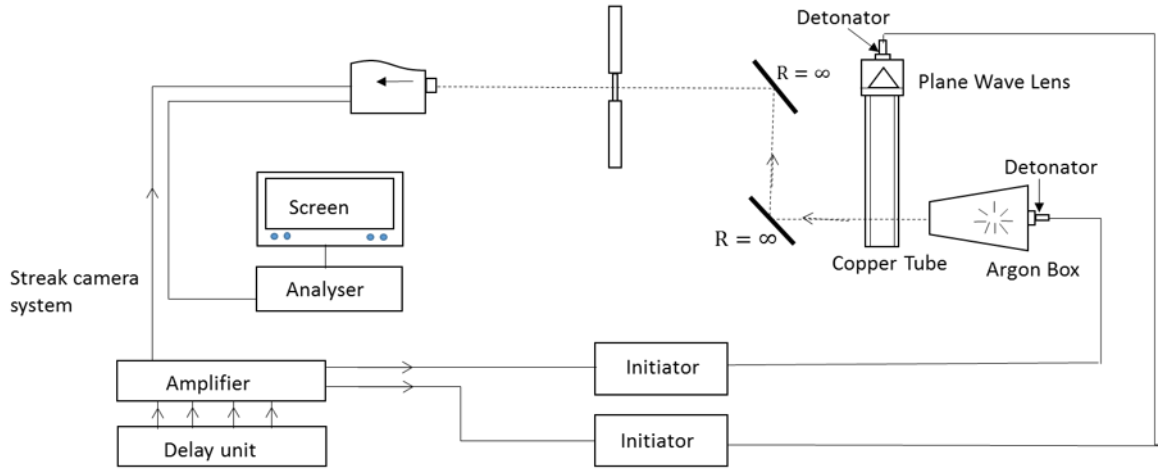

Figure 2.4: Schematic configuration of the cylinder expansion test setup- adopted from[10]

Snyman and Olivier employed a diffusing screen made from Lexan between the argon bomb and the cylinder, as shown in Figure 2.5, to reduce the direct luminosity into the recording UHSC and simultaneously providing enough contrast lighting for a complete shadow of the cylinder[5]. The detonation wave is usually assumed, without being confirmed, to have smoothed itself out by the time wall measurements are made[29]. After the detonation of the explosive, reaction products occur in a gas state. The elastic-plastic properties of the cylinder allow it to expand to three times the original diameter, with velocities of interest at radial distances, 6 mm, 12.5 mm and 19 mm[30,31]. In Figure 2.5, the frame serrated on both left and right sides functions as a metric scale for the expansion diameter[32].

Figure 2.5: Cylinder setup with diffusing Laxen screen and serrated frame. A view for the recording UHSPC[5]

A few assumptions are adopted during the derivation of the relationship between parameters of the detonation products that result from the cylinder test. It is assumed that during detonation[7,9] :

- All kinematic processes in relation to central cylinder surface are assumed to remain constant for the entire expansion phase.
- The cylinder wall is incompressible.
- The detonation wave is planar and in a steady state.
- The explosive material transforms to detonation products immediately upon arrival of the detonation wave.
- Gas products have negligible viscosity.

It is also difficult to recognize the instant initial expansion of the copper tube because the cylinder motion is unstable at the early stages of expansion[8]. Upon detonation the shock wave progresses through the cylinder at a detonation velocity "D" as indicated in Figure 2.6. The shock wave is accompanied, from behind, by a flow of gaseous detonation products "W" of extremely high pressure[9,33]. It is the gaseous products that causes the wall expansion of the cylinder[33]. In the progression of detonation, the shock wave reflects through the wall in alternating series of compression and expansion waves. The expansion waves influence the expansion of the cylinder wall[20].

During the cylinder expansion test, the employed measuring diagnostic usually observes the most favourable flow conditions, when detonation has reach its steady state[8]. The steady state occurs at the end of the reaction zone known as the Chapman Joguet (CJ)[34], where CJ condition must be considered. Since the cylinder wall is assumed to be incompressible during detonation; the stream of gas passing through the cylinder enclosed by a circle of original surface area is equal in quantity to the gas spreading out through the expanded surface area of the cylinder[9]. According to the conservation of mass this relation is expressed in Equation 1 using variables indicated in Figure 2.6 as;

$$\pi(r_e^2 - r_i^2) = \pi(r_{e0}^2 - r_{i0}^2) = \text{Area} \qquad \text{Equation 1}$$

Where r_{i0} and r_{e0} are the radial positions of the inner and outer original surface of the cylinder, respectively, and r_i and r_e are the radial positions of the expanded inner and outer cylinder wall, respectively[21].

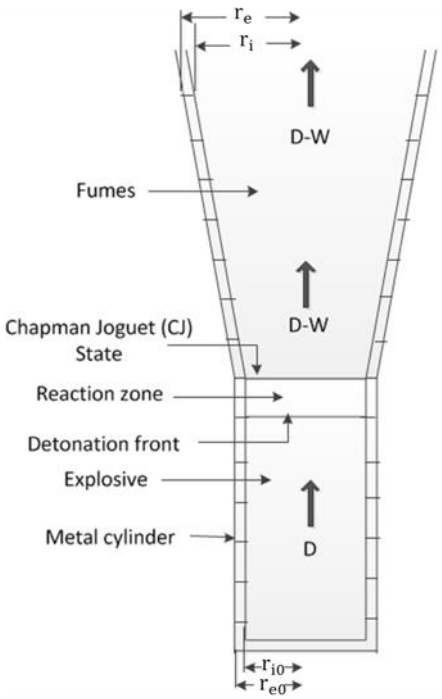

Figure 2.6: Schematic showing the flow conditions of the detonation products in an expanded cylinder- adopted from[9]

2.3. Parametric determination of the JWL EOS parameters from the cylinder test results

The results obtained from the cylinder expansion test, in practice can be used to determine the JWL EOS parameters[9,10]. Differentiation of the radii obtained from images of the expanded cylinder wall at different positions, leads to obtaining the velocity history of the expanded cylinder. Velocity at particular wall expansions is of greater interest, although the wall expansion radius is of importance in studying the effects of EOS parameters[24]. EOS of detonation products are mathematical expressions which describe particle streamlines behind the chemical reaction zone. Laboratories and research groups use these EOS to predict the flow trajectories associated with energetic materials[35]. Once the radial expansion history of the cylinder wall is obtained, a curve relating pressure to specific volume ($P = P(V)$) for the explosive detonation products can be reconstructed. The $P = P(V)$ curve describes the adiabatic expansion from the CJ state (P_{CJ}, V_{CJ}). Where, P_{CJ} and V_{CJ} are pressure and volume at CJ state conditions, respectively. The procedure leading to the $P = P(V)$ curve requires;

- double differentiation of the radial displacement to obtain acceleration;
- calculation of pressure as a fuction of acceleration;
- and determination of the density as a function of radius and gas velocity.

Once all the variables have been determined numerically, P_{CJ} and V_{CJ} can also be obtained. Another useful quantity which can be determined from pressure and volume is gamma, the ratio of the specific heat. All these variables are presented in detail by Polk[21]. Once all the variables are obtained, the JWL EOS can be fitted into the experimental data obtained. JWL EOS is used to calculate the products state as they expand from a certain high-pressure, high-density condition following the chemical reaction to some terminal state at normal pressure and gaseous density[35]. The JWL EOS is a Mie-Gruneisen based EOS formulated from experiments by Jones and Miller, Wilkins and Lee[36], hence the acronym "JWL". Jones and Miller formulated calculations for initial conditions that can be utilized as an initial point to determine the relation between pressure, volume and temperature in the detonation shock front at different loading densities during an adiabatic expansion of a material[37]. The Jones' relation is given as;

$$P = Ae^{-RV} - B - CT \qquad \text{Equation 2}$$

Subsequently to add on the equation by Jones, Wilkins developed an equation using spherical metal expansion experiment. The equation is given as;

$$P = \frac{a}{V^Q} + B\left(1 - \frac{\omega}{RV}\right)e^{-RV} + \frac{\omega E}{V} \qquad \text{Equation 3}$$

Where A, B and C [GPa] are pressure coefficients and R is the eigenvalues. E is the internal energy of detonation products per unit volume [GPa], ω is the fraction of the adiabatic exponent.

$$P(\Delta) = \frac{a}{V^Q} + Be^{-RV} + \frac{C}{V^{\omega+1}} \qquad \text{Equation 4}$$

Where;

$$a = a\frac{(Q-1)}{(Q-1-\omega)} \qquad \text{Equation 5}$$

V is the relative volume given as $V = \frac{v}{v_o}$, Δ is an abbreviation for adiabat and the pressure in megabars (Mbar). Wilkin's[36] work responded well to both hydrodynamic and experimental calculations with highlights on the initial stages of detonation products expansion. Later, Lee extended the work by Jones and Wilkins by developing an equation from cylinder metal expansion results. The equation obtained can also be used for the expansion of detonation products involving large geometries[36]. The final equation from Jones, Wilkins and Lee's work in its general form is given as;

$$P = A\left(1 - \frac{\omega}{R_1 V}\right)e^{-R_1 V} + B\left(1 - \frac{\omega}{R_2 V}\right)e^{-R_2 V} + \frac{\omega E}{V} \qquad \text{Equation 6}$$

Urtiview and Hayes[35] revisited the JWL EOS to introduce a dynamic condition to the equation. The study also provided a complete description of the principal eigenvalue "R_1" and secondary eigenvalue "R_2" that lead to a well behaved gamma profile. Equation 7 presents transformed vesion of the JWL EOS that satisfy isentropic flow conditions of detonation[35,36].

$$P = Ae^{-R_1 V} + Be^{-R_2 V} + CV^{-(\omega+1)} \qquad \text{Equation 7}$$

1st 2nd 3rd

The constants ω, R_1, R_2, A and B govern the amount of energy available to do work between early and expansion times. The complete adiabatic expansion region is controlled by the three terms making up the JWL EOS, and that control is reproduced in the shape of the gamma profile as shown in Figure 2.7[35]. The behaviour of detonation products at high pressures and low expansion ratios is defined by the first term of Equation 4[7]. The principal eigenvalue R_1 dominates the wave shape at and near the gamma profile near the CJ plane as shown in Figure 2.7. It dominates up to where velocity of the explosive gas particle becomes zero[35].

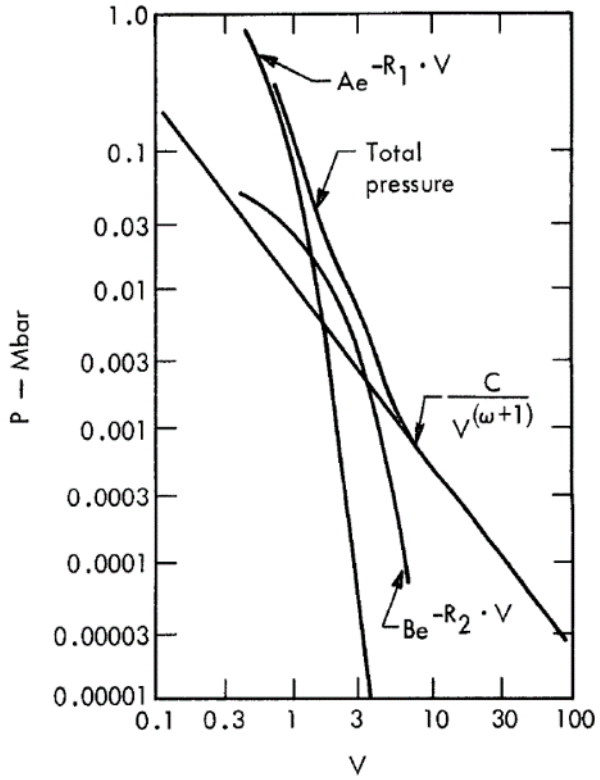

Figure 2.7: "Contributions of various terms in JWL EOS to total adiabat" (adopted from[38]).

In Figure 2.7, the intermediate pressure zone, 2nd term of Equation 4, is the isentrope in the low pressure area[7]. In this term the secondary eigenvalue R_2 along with the energy value E_0 controls the transition region before the adiabatic exponent $(\omega + 1)$ takes over[35]. And the large expansion ratio is described by the third term of Equation 4, the adiabatic expansion ratio[7]. It is a variant of the ideal gas equation where the pressure is a power function of the volume. It is necessary to have this term, since the function must approach the ideal gas equation at very large expansions. A detailed description of the variables that make up the three terms in Equation 4 is given by Urtiview and Hayes[35]. Barker et al provided a thermodynamic and mathematical background of the JWL EOS. The study also presented an analytic cylinder model as well parametrization method. Barker achieved an excellent agreement in the prediction of cylinder velocities between the diagnostic cylinder test and high rate continuum modelling[39]. One of the advantages of the JWL EOS is its practical nature and the large enough data base of experimental and popular explosives it supports[35].

Chapter 3

Optical velocity interferometer techniques

3.1. Introduction

High speed photography, for many years, led as the only method used to gather experimental data from the cylinder expansion test in order to derive the JWL EOS parameters. The velocity of the cylinder as it expands radially would be determined by differentiation of the cylinder radial expansion displacement points from the captured photographs. Later in the years a number of optical interferometer velocimeters were developed which directly measure velocity from the expanded cylinder during a cylinder expansion test. Velocity interferometers are used to obtain material properties under high pressure acceleration and shock loading conditions[40]. A homodyne-based velocimeter was verified to measure up to a maximum velocity of 12 km/s[41]. All optical velocimeters operate in the same principle regardless of their arrangement; Doppler shift of the coherent incident beam upon reflecting off a surface in motion with the aim to determine the velocity of the target[42,43].

Most interferometer techniques require the target surface to be reflective and sometimes be tilted slightly during detonation[44]. Optical fibers are utilized to send the incident light to the target and collect the light reflected off the target because of their versatile and robustness that enable remote operations[45]. In this chapter, three most popular velocimetry systems in the field of explosive research will be discussed. They are, Fabry-Perot Interferometer (FPI) developed in the 1980s by LLNL, the Photon Doppler Velocimeter (PDV) which was reported in 2006 by LLNL and Velocimetry Interferometer for Any Reflector (VISAR) developed in the late 1960s by Sandia National laboratories[46]. Both the VISAR and Fabry-Perot are based on the determination of the velocity of fast-moving surface by the Doppler Shift of reflected light. Due to their implementation they have their advantages and disadvantages[46].

3.2. Fabry-Perot Interferometer (FPI)

The Fabry-Perot system was developed at LLNL as the basic of the standard diagnostic for measuring kilometre-per-second velocities on explosive experiments[47]. It records data on streak cameras, which have limited record lengths. FPI has a simple structure, its high resolution has been verified to be a controlling tool in many of its applications[48,49]. In shock waves experiments, FPI can measure targets free surface velocity ranging from 100 to 8000

m/s with recorded durations varying from 0.2 to 100 μs[48]. Figure 3.1 shows the schematic of a FPI system.

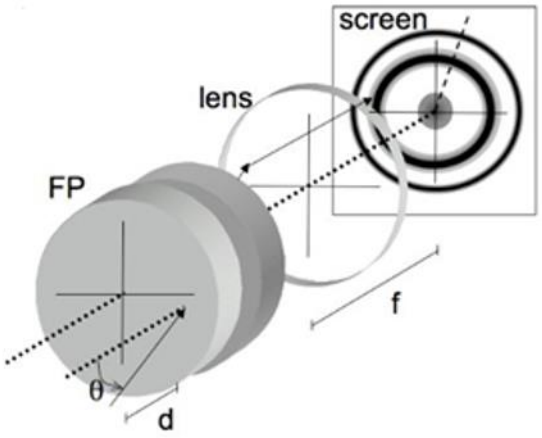

Figure 3.1: Fabry-Perot Interferometer System

FPI makes use of reflections between two closely separate glass plates which function as mirrors that partially reflect and transmit light multiple times[48]. Figure 3.2 shows the working principle of the FPI. A ray of light reflected by the target surface enters the interferometer. The light come across two mirrored plates. The two plates, M1 and M2, are parallel and separated by the distance "d" which is typically a few nanometres[49]. In the FPI light goes through the first mirror "M1", once it encounters the second plate "M2" a fraction of the light gets reflected multiple times with insignificant amount of energy escaping from each reflection[48,50]. The smaller fraction gets transmitted through "M2" and the larger fraction is reflected. For every occurrence of reflection and transmission, the wave amplitude is split into two fractions. This results in a path length difference between subsequent transmissions which produce interference patterns. The angle at which constructive interference occurs changes with frequency of the light going to the FPI, hence forming contracting or expanding rings diameter[48].

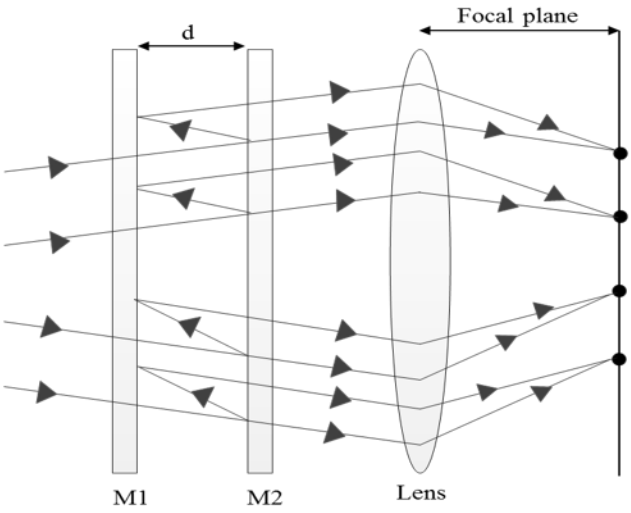

Figure 3.2: Illustration of the working principle of the FPI- adopted from[48]

As shown in Figure 3.2, at the focal point of the output lens to the detector, rays that reflected from the same ray are brought to the same point. These rays reach the detector as rays that are parallel to one another. The motion of the reflecting surface, influences the diameter of the circular fringes relative to wavelength[42]. Basically, FPI relies on the fringe position captured to obtain velocity information[51]. The main advantage of the FPI system is that it does not measure intensity vs time, rather position vs time[50]. Even if the intensity of the reflected light changes due to alterations on the surface of the target, the position recordings do not get tampered with. In addition, data is easily reduced and from analysing a single photograph, difference between acceleration and deceleration can be recognised; unlike in a case where the intensity is recorded, the fringes signal has to be in quadrature[42]. The FPI can impressively handle more than one reflected frequency of light, that is why it is regarded as reliable[50,52].

A Fabry-Perot system uses free-space interferometers and streak cameras for each data channel. The disadvantage is that components are costly, complex, require maintenance and operator setup, require a custom-built optical table and with all these components occupy quite a bigger space. The Fabry-Perot system also uses a large YAG laser whose output is doubled to 532 nm because the streak camera photocathode is insensitive in the infrared region of the spectrum. Even if the Fabry-Perot velocimeter produces excellent data, limitations in the entire channel count remain due to its size, cost, and complexity[53].

3.3. Photo Doppler Velocimetry (PDV)

PDV is a displacement interferometer that operates by telecommunications optical components of high-bandwidth[54,55]. It is a heterodyne velocimetry technique, following its development

around heterodyne detection using near infrared (1550 nm) single-mode fibre technologies[43,53]. In this technique, light fringes correspond to a displacement of the measured surface of half a wavelength of the incident laser light[55]. PDV operates by superimposing a portion of both the incident and reflected Doppler Shifted light and measuring the beat frequency which is proportional to the surface velocity of the moving target[46,47,56]. The heart of a PDV is a Mach-Zehnder Interferometer (MZI). The principle on which the MZI operates is given schematically in a PDV setup shown in

Figure 3.3. Generally, light trarvese through an optical fibre to the probe that launches it to the target in motion. The system is designed such that, a fraction of the incident light by-passes the probe and traverse straight to the detector as non-shifted beam[47].

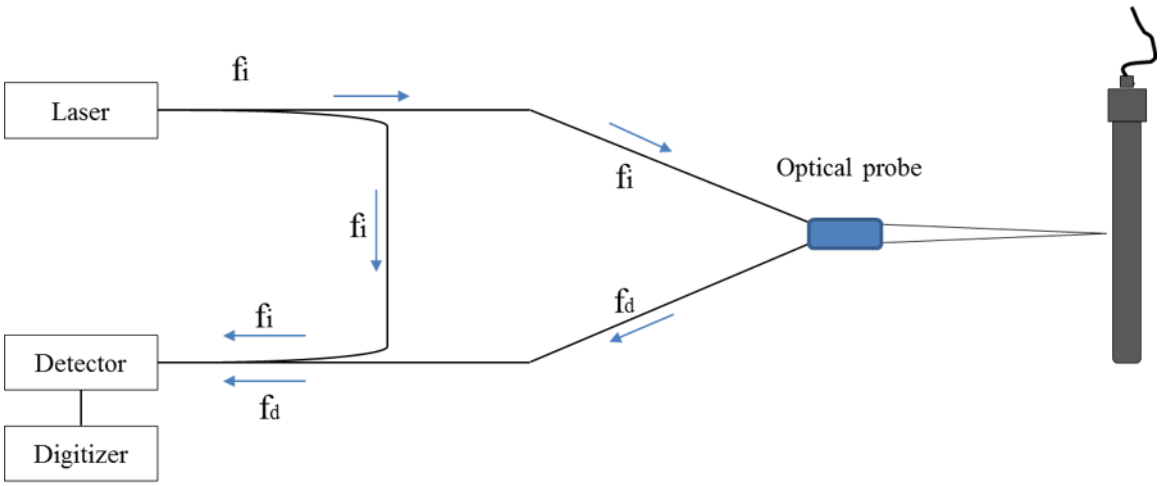

Figure 3.3: Schematic of PDV with a cylinder as target- adopted from[47]

In

Figure 3.3, the frequency of the incident beam is "f_i" and the Doppler shifted beam is "f_d". The two beams carrying varying frequencies (f_i and f_d) traverse to a detector systems with a bandwidth high enough to respond to their varying frequencies, that is the beat frequency. At visible and infrared wavelengths, the non-shifted beam frequency and the Doppler shifted frequency are higher than the detector response; and as a result appear as continuous wave components in the detector signal[51]. PDV has proved to give output signals of good quality in difficult field setups. It has replaced velocimetry diagnostics of lower quality. Hence, it is called the " velocimetry for masses"[54]. PDV system is quite simple to put together and uses components available on-shelf. Similar to the FPI, PDV can measure multiple frequencies[56].

3.4. Velocity interferometer for Any Reflector (VISAR)

Shock compression experiments using velocity interferometry has been in use for many years, but such measurements were uncommon until Barker and Hollenbanch developed a VISAR in 1972[14,44]. The VISAR optically detects fast motion of a reflective or diffuse target surface and converts the detected motion into velocity measurements by Doppler-shifting the light upon reflection[44]. It is built on a Wide Angle Michelson Interferometer (WAMI), which is described to demonstrate a feasible interferometry system for velocity measurements[14,57]. Literature describes the WAMI as early as 1941[44]. WAMI is a modified Michelson interferometer in which light propagating through one of its two paths (or sometimes referred to as legs) is delayed by an etalon glass of specific length and refractive index. The configuration of the WAMI is such that, both paths are equal in length but light is delayed in time on the path with an etalon due to the optical path difference. Figure 3.4 shows a schematic of a WAMI configuration.

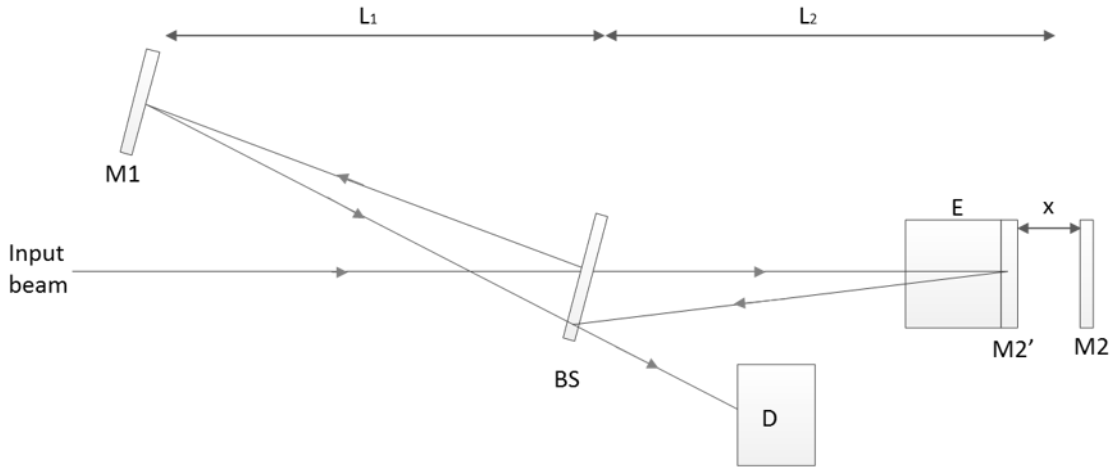

Figure 3.4: Schematic of the WAMI (Joshi, Rav et al. 2011)

In Figure 3.4, the virtual length of "$\mathbf{L_2}$" is equal to "$\mathbf{L_2 - x}$" which must be equal to the actual length of "$\mathbf{L_2}$" for interference to occur[57]. Therefore the distance "**x**" between the M2' and M2 is given as[44,57]:

$$x = h(1 - \frac{1}{n}) \qquad \text{Equation 8}$$

Where h is the length of the etalon and n its refractive index.

If the actual length of the leg with etalon is L_2, it means that the laser light travels a distance of $L_2 - h$ in air and h in etalon. The derivation of this delay time in the etalon is as follows;

$$\tau = 2[\left(\frac{L_2 - h}{c} + n\frac{h}{c}\right) - \left(\frac{L_1}{c}\right)]; \quad \text{Equation 9}$$

$$= 2[\left(\frac{L_2 - h}{c} + n\frac{h}{c}\right) - \left(\frac{L_2 - x}{c}\right); \quad \text{Equation 10}$$

Substituting Equation 7 in Equation 9 results in the following expressions;

$$2[\left(\frac{L_2 - h}{c} + n\frac{h}{c}\right) - \left\{\left(\frac{L_2}{c}\right) - \frac{h}{c}\left(1 - \frac{1}{n}\right)\right\}]; \quad \text{Equation 11}$$

$$2[\left(\frac{L_2 - h}{c} + n\frac{h}{c}\right) - \left(\frac{L_2}{c}\right) + \frac{h}{c} - \frac{h}{nc}]; \quad \text{Equation 12}$$

$$2\left[\frac{nh}{c} - \frac{h}{nc}\right]; \quad \text{Equation 13}$$

Therefore, light is delayed on one path by τ equating to;

$$\tau = 2\frac{h}{c}\left[n - \frac{1}{n}\right] \quad \text{Equation 14}$$

When "$L_2 - x$" is equal to "L_2", good fringe contrast can be obtained even with lighted reflected off a diffuse surface, hence spatial coherence of the light is not required. Unlike in a Michelson Interferometer (no etalon used), the long path length difference in the interferometer requires a good mirrored target surface in order to maintain spatial coherence on the reflected beam. This reflected beam is an incident beam on the VISAR interferometer[44]. The delay time brings a difference in the times at which the Doppler shifted light transit through the two paths so that not only good fringes are obtained but also the motion of the target surface is detected[44]. In addition to the etalon, another slight delay is brought by a retardation plate (1/8 wave-plate) whose function is described below under the discussion on Push-Pull VISAR. Similarly to other FPI and PDV, the VISAR make use of a fibre optical arrangement to direct the laser light to the target and collects the reflected back scattered light signal into the interferometer. The VISAR has been improved through out the years to be a more effective velocimetry interferometer. For the purpose of this study, in this section only a Push-Pull VISAR will be discussed.

3.4.1. Push- Pull VISAR Theory

The Push-Pull VISAR is a significant improvement of the previous VISAR (Conventional VISAR), mainly in experiments with minimal laser power where incoherent light is strong

(Dolan gives a detailed description of a conventional VISAR)[14]. Basically, the Push-Pull VISAR uses the interferometer signal normally wasted in a conventional VISAR to improve signal[58]. Figure 3.5 shows an oscillograph of the signals from the two VISAR systems mentioned above.

The first signal in Figure 3.5 is one of the two interferering quadrature coded signal recorded in the conventional VISAR since it has a single polarizing beam splitter. The quadrature signal in the middle was previously wasted in the conventional VISAR because light, upon recombination at the beam splitter traverse two different directions. In a Push-Push VISAR both light signals are retained and traverse to two built-in polarizing beam splitters. The third signal shown in Figure 3.5 is two quadrature coded signals from a one of the two Push-Pull VISAR polarizing beam splitters after they have been differentially amplified. The "zero interference" line indicates the non-interefering fraction of the signal which in the photodetectors, the amplification factors cancels out and hence results in no interference[58].

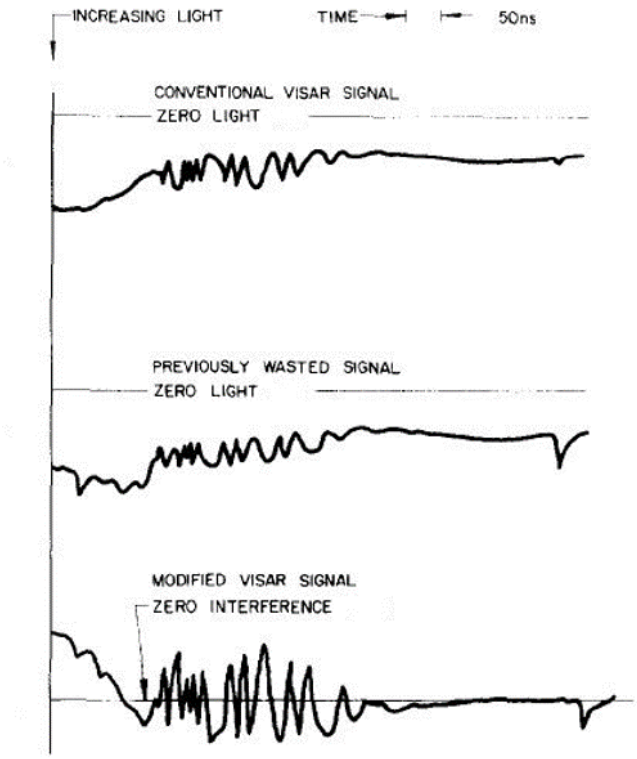

Figure 3.5: Comparison of simultaneously obtained conventional and Push-Pull VISAR signals- adopted from[58]

Push-Pull VISAR is created through subtraction of appropriate pairs of signal coming from two polarizing beam splitters[14]. The pairs of signals are doubled and subtracted to remove the noise embedded in the incoherent signal, a noninterfering signal[59]. This subtraction is

performed by the differential amplifiers[14]. The fringe shift resulting from the surface target can be recorded by streak camera. However, oscilloscopes are more common available since the streak camera is more expensive. Figure 3.6 shows a schematic of the "heart" of a Push-Pull VISAR system.

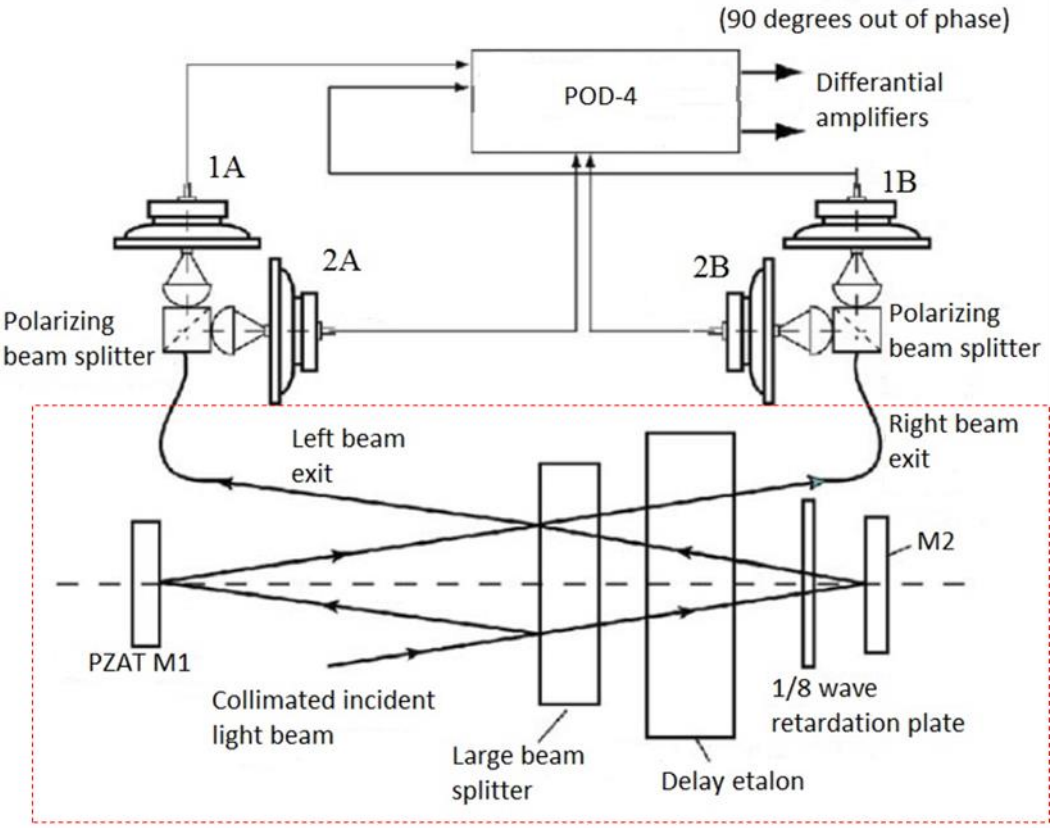

Figure 3.6: Configuration of the "heart" of a Push-Pull VISAR- adopted from[60]

In Figure 3.6, the dashed red rectangle demarcates the VISAR's WAMI. In this study, the description of how the light transit the VISAR is based on the Valyn VISAR module shown in Figure 3.7. Valyn VISAR is a multi-beam Push-Pull VISAR. The description takes into account the optical components, which come already installed as shown in Figure 3.7, directing the light to the interferometer and to the signal processing system.

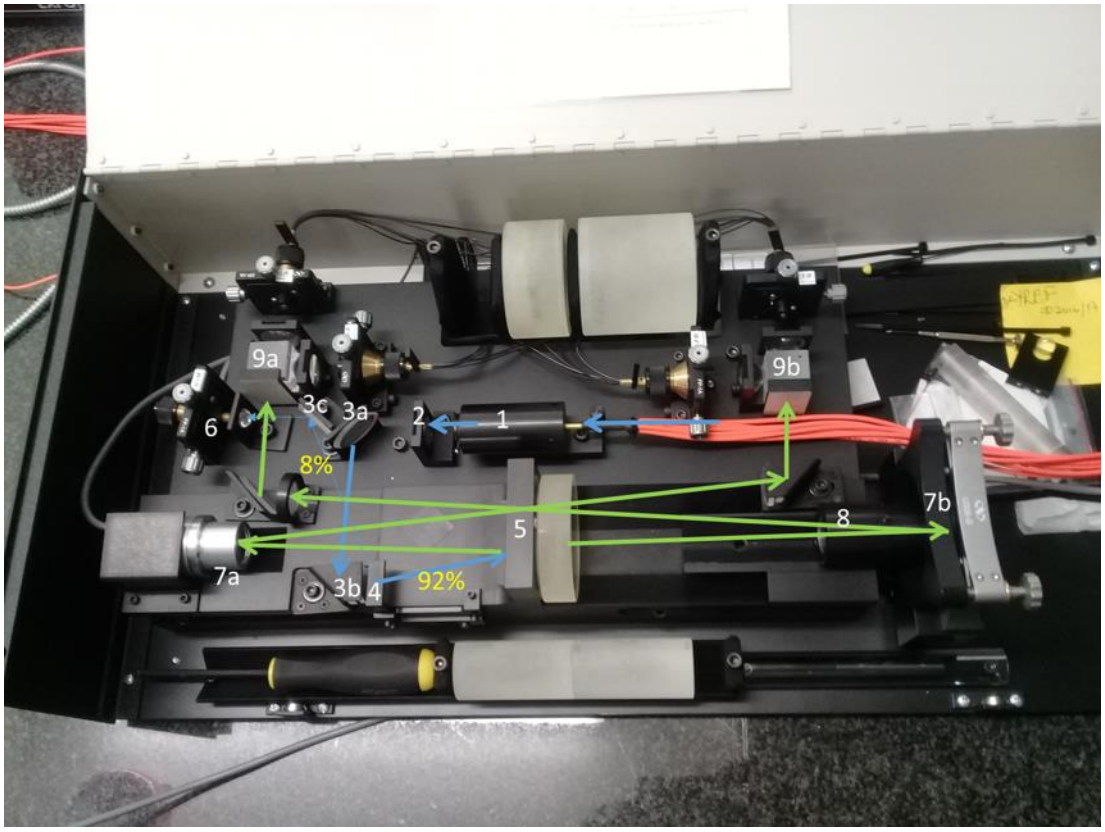

Figure 3.7: Valyn VISAR module showing the light path

The VISAR module contains the interferometer (WAMI) and relevant optical components which are fixed in a box like housing as shown in Figure 3.7. Inside the module, the Doppler shifted light first encounters a collimator where it gets collimated before it is further transmitted. The collimator consists of a plastic Flexalign assembly **(1)** in an aluminium housing. In front of the Flexalign is an iris diaphragm which allows for easy attenuation of the light signal by decreasing the beam diameter coming through the collimator. The light signal from the collimator encounters the Utra-Narrow Bandpass (UNBP) filter **(2)**.

UNBP filter passes only light within about +/- 0.5 nm of the 532 nm laser wavelength. It passes only 40% of the laser light. Its purpose is to minimize white light from the event which could unfavourably affect the outputs from the VISAR's fringe signal recording photodetectors. After the UNBP filter, light goes to two high-efficiency oval mirrors **3a** and another mirror in **3b** fitting. The two mirrors are coated to reflect over 99% of 532 nm wavelength light when the angle of incident is 45^0. The mirrors position the beam to enter the interferometer. After the light passes the second mirror in **3b**, it passes through a 500 mm focal length lens also in 3b fitting which keeps the beam as small as possible when traversing into the interferometer. The

interferometer optics are nearly perfect for the small optics than for larger one which is crucial for the beam size to be small.

From the lens, light encounters a BIM beam splitter assembly **(4)** where a small amount, about 8%, from the Doppler shifted light is split for the BIM photomultiplier unit via the mirror **(3c)** to the BIM fibre optic pick-up lens **(6)**. The BIM beam splitter is oriented and tilted for precise centering of the reflected light on the BIM fibre optic pick-up lens enroute to its own PMT. The BIM detects any change in the intensity of the light reflected off the target surface. Intensity changes result mainly from shock-induced changes in reflectance of the surface [44].The rest of the light split by the BIM beam splitter goes to the interferometer beam splitter **(5)**.

The 50/50 interferometer beam splitter is the first component of the VISAR's interferometer (WAMI) components. It is coated to split the beam with 50% transmission and 50% reflection on one surface and the other surface is anti-reflection (AR) coated for less than ¼ % reflection at 532 nm wavelength. This beam splitter splits light to traverse through the two interferometer paths and gets reflected back by the two high-efficiency interferometer mirrors **(7a and 7b)** in the paths. One mirror **(7a)** is mounted on a piezoelectric translator. By varying the voltage to the translator through BIAS potentiometers, varies the path length towards **(7a)** of the interferometer by a few wavelengths of light. Variation in the potentiometer setting allows for a production of a few fringes, a feature which allows for the alignment of the interferometer, for checking of the alignment and fringe contrast, and for setting the refraction sensitivities of the recording oscilloscopes[44]. Mirror **(7b)** is held by a metal tube which mounts a one-eighth wave-plate **(8)**. The one-eighth wave plate retards the *P* component of the light by a phase angle of 90^0 with respect to the S component of the same transmitted light. Thus, at the point of recombination on the beam splitter, the S and *P* components form two fringe patterns that are 90^0 out-of-phase[44].

Afterwards, The light carrying 90^0 out of phase fringes get separated from each other by the pair of polarizing beam splitter **(9a and 9b)**. The polarizing beam splitters separate the horizontal polarized light fringes from the vertical polarized light. The polarizing beam splitters utilize a Bouricious and Clifford method where half-S and half-P polarized light signals are obtained by polarizing the incident Doppler shifted light at 45^0 to the vertical[44].
The four signals carrying fringe information are directed through pick-up lenses (1A-1B and 2A-2B in Figure 3.8) to their individual photomultiplier tubes (PMTs) housed in a unit referred to as a POD-4 inside the signal recording system (beam module) as two pairs of 180^0 out of

phase signals. The PMTs transform the fringe signals into voltage signals. The low-noise PMT unit from Valyn has a high voltage range of -700 to -1000 V with a 1.0 rise time. The two differential amplifiers shown in Figure 3.8 amplify the four voltage signal from the four PMTs. The 90^0 phase difference is accomplished by the pair of differential amplifiers between 1A-2A and 2A-2B quadrature output signals from the PMTs. Each differential amplifier subtracts each pair of signal with respect to 90^0 relationship phase of the two signals. Thereafter the resulting voltage signal is amplified by a factor of 10^{61}.

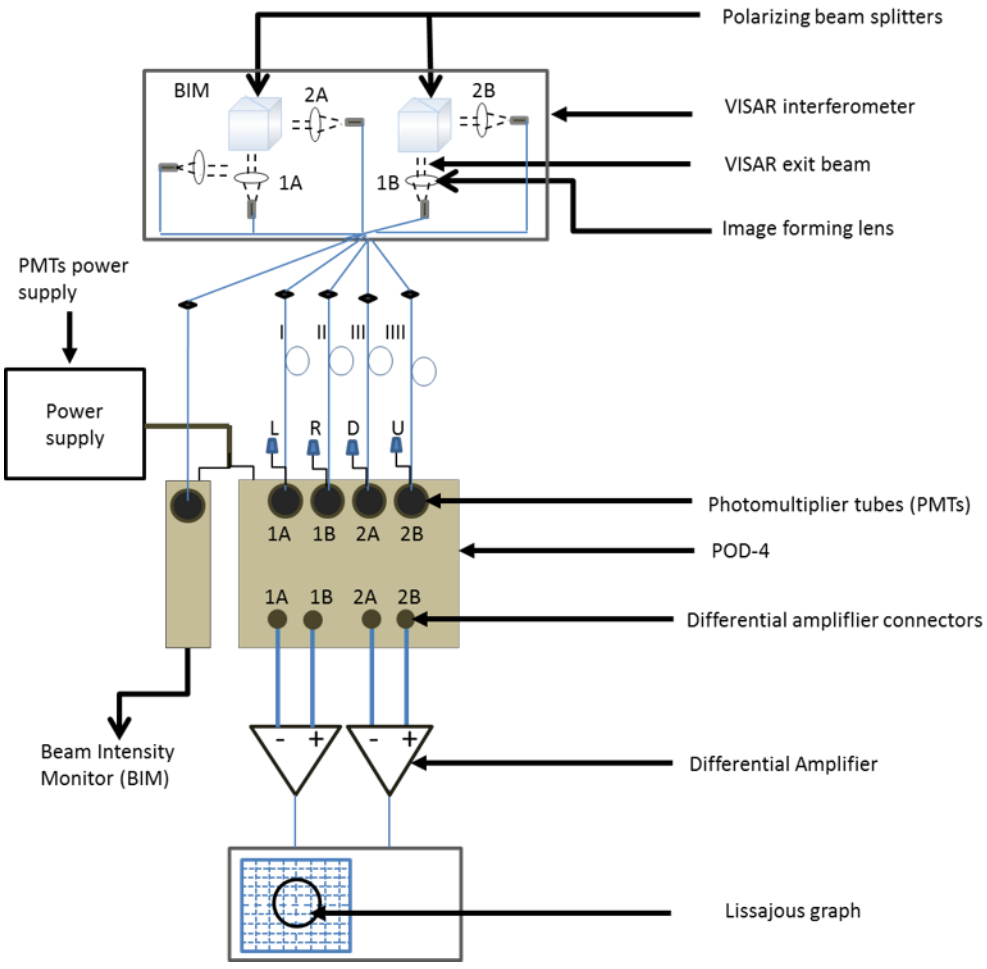

Figure 3.8: Light signals from photomultiplier tubes to differential amplifiers- adopted from[61]

The amplified pair of voltage signals gets plotted on the amplified monitoring oscilloscope (AMO) as a Lissajous graph. Steady Lissajous figure can be achieved by optimizing alignment in the interferometer by using two of the three BIAS potentiometers on the ramp generator, which vary the voltages to the three piezoelectric elements in the PZAT. A 2 s duration setting on the ramp generator is important to get visible fringes but can be ramped up to 100 ms once

the Lissajous has been obtained. The ramp generator's ramp capability produces fringes at speeds from very low to about 1 kHz.

A steady Lissajous graph is important since it indicates that the entire setup is ready for measurement. It indicates a number of things going on; (1) the laser is on (2) target surface is well prepared (3) light is going into the VISAR module (4) light is coming out of the VISAR module and (5) the photomultiplier tubes in the beam module are well functioning. The recording oscilloscopes track the voltage signal from the AMO in the beam module in the form of sine waves, which results from the changes happening on the detonation driven target. The entire VISAR system consists of a laser, optical probe, VISAR interferometer module, signal processing system known as the beam module, recording oscilloscope. Figure 3.9 presents a schematic of the entire VISAR system instrumentation, where a spectral reflecting cylinder is assumed.

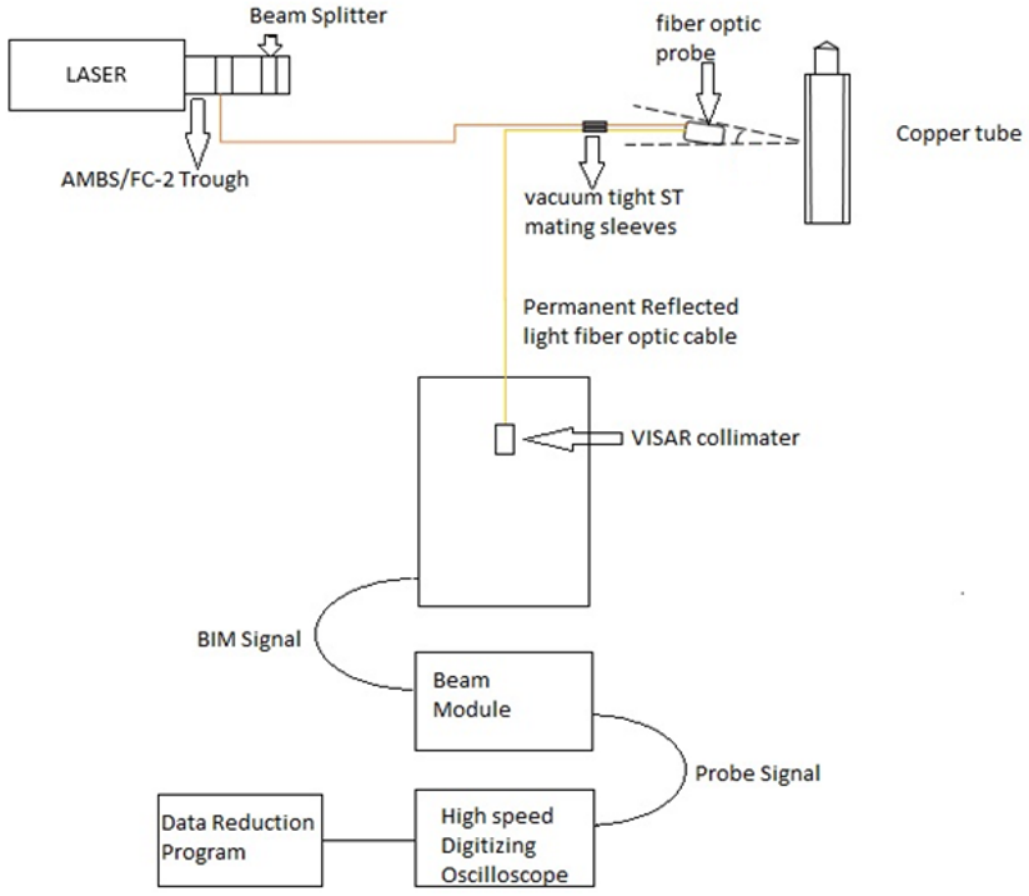

Figure 3.9: VALYN VISAR complete set-up- adopted from[61]

One of the great advantages of the Push-Pull VISAR is the four quadrature outputs with a distinct phase it provides that enables it to provide a level of accuracy in velocity measurements[59]. The quadrature fringe recording, not only makes the determination of the fringe count, very accurate, but also distinguishes acceleration from deceleration automatically. This is mainly useful when the velocity history is complicated, which occurs when a target under detonation vibrates due to internal reflections of a single or many waves[55].

3.4.2. Applications of VISAR

The main application of VISAR has been in the measurements of free surface velocity histories of shocked plates in impact arrangement. This work has reported also a study that describes application of VISAR laser interferometer in the field of terminal ballistics[16]. The study highlighted examples in which the potential of this instrument could be presented; that is "impact of a steel rod against a steel target plate, acceleration of a projectile in a two stage light gas gun, expansion of high explosive loaded cylinder and hypervelocity impact of a ball against an aluminium target"[16]. Hongliang et al[59] reported on the application of the Push-Pull type VISAR for measuring the ablative acceleration of strong pulsed laser beam driven foil plates. They employed an electronic streak camera to record the fringe pattern. The optical system developed in the study indicated all the advantages of the Push-Pull type VISAR with a time resolution much higher than the conventional type VISAR[59].

VISAR is also applicable in window interferometry for getting information about either compressive or rarefaction shock wave profiles. This can be done by fastening an appropriate optical transparent window at the rear surface of the target and record velocity history at the interface between target and window[57]. VISAR's leading advantages are the nanoseconds rise time, approximately l% to 2% accuracy and its capability to monitor both a specular and diffuse reflecting surface[16]. Resnyansky et al[62] used a numerical analysis that confirmed the VISAR's ability to resolve processes on the nanosecond time scale. They used a gas gun system where a VISAR records the free surface velocity of an aluminium target plate exposed to high velocity impact by a steel flyer plate at impact velocity. Joshi[63] used the VISAR to determine spall strength of two industrially important materials, Al2024-T4 and SS304 with a gas gun system as the projectile.

This VISAR has gained popularity over the years as the standard tool for measuring velocity history in shock studies[59]. Push-Pull VISAR system is particularly effective in obtaining

velocity measurements with target's surface exposed to more than a single wavelength of light because it can distinguish its required wavelength from other sources such as bright flashes[58]. VISAR can be powered entirely by a single standard generator, making remote field applications a realistic effort[15].

3.4.3. Push-Pull VISAR data reduction program

The VISAR detector and a WAMI system have similar outputs with the addition of an extra subscript to indicate which polarization is being measured[14], horizontal polarization represented with subscript x and vertical with subscript y. Output signals from the four detectors (PMTs) are given as follows:

$$D_{1A}(t) = \hat{a}_{11}^2(t)I_O(t-t_1) + \hat{a}_{21}^2 I_O(t-t_2) + 2\hat{a}_{11}\hat{a}_{21}\sqrt{I_c(t-t_1)I_c(t-t_2)}\cos\varphi\,(t)$$

Equation 15

Where $\hat{a}_1, \hat{a}_2$ are coupling constants, I_c denotes the coherent input intensity, t_1, t_2represents the transit time of the beam through the reference path anddelayed path, respectively and $\varphi(t)$ denotes the phase difference

$$D_{2A}(t) = \hat{a}_{12}^2(t)I_O(t-t_1) + \hat{a}_{22}^2 I_O(t-t_2) + 2\hat{a}_{12}\hat{a}_{22}\sqrt{I_c(t-t_1)I_c(t-t_2)}\cos\varphi_2\,(t)$$

Equation 16

$$D_{1B}(t) = \hat{b}_{11}^2(t)I_O(t-t_1) + \hat{b}_{21}^2 I_O(t-t_2) + 2\hat{b}_{11}\hat{b}_{21}\sqrt{I_c(t-t_1)I_c(t-t_2)}\cos\varphi\,(t)$$

Equation 17

$$D_{2B}(t) = \hat{b}_{12}^2(t)I_O(t-t_1) + \hat{b}_{22}^2 I_O(t-t_2) + 2\hat{b}_{12}\hat{a}_{22}\sqrt{I_c(t-t_1)I_c(t-t_2)}\cos\varphi_2\,(t)$$

Equation 18

$\varphi_2(t)$ is the phase difference function that accounts for the round trip travelled by the Doppler shifted beam through the one-eighth wave plate. The delay difference between polarizations is associated with a relative phase delay β;

$$\varphi_2(t) = [\varphi(t-t_2) - \beta] - \varphi(t-t_1) = \varphi(t) - \beta \qquad \text{Equation 19}$$

Since the beam passes through the one-eighth wave plate twice, the phase shift ranges between zero and a quarter of a wave. The pairs of the detector signals are said to be in perfect quadrature when $\beta = \frac{\pi}{2}$. The phase delay, β, for convenience, is expressed in terms of quadrature error ε, which describes the off-set of the VISAR system from being in perfect quadrature[14]. Hence, is $\varphi_2(t)$ given as;

$$\varphi_2(t) = \varphi(t) - {}^{\pi}/_{2} - \varepsilon \qquad \text{Equation 20}$$

Combining the definition in Equation 20 with Equation 16 and Equation 18 converts the cosine factor to a sine and the resulting detector outputs are given as;

$$D_{1A}(t) = \hat{a}_{11}^2(t)I_O(t-t_1) + \hat{a}_{21}^2 I_O(t-t_2) + 2\hat{a}_{11}\hat{a}_{21}\sqrt{I_c(t-t_1)I_c(t-t_2)}\cos\varphi\,(t)$$

Equation 21

$$D_{2A}(t) = \hat{a}_{12}^2(t)I_O(t-t_1) + \hat{a}_{22}^2 I_O(t-t_2) + 2\hat{a}_{12}\hat{a}_{22}\sqrt{I_c(t-t_1)I_c(t-t_2)}\sin(\varphi(t)-\varepsilon)$$

Equation 22

$$D_{1B}(t) = \hat{b}_{11}^2(t)I_O(t-t_1) + \hat{b}_{21}^2 I_O(t-t_2) + 2\hat{b}_{11}\hat{b}_{21}\sqrt{I_c(t-t_1)I_c(t-t_2)}\cos\varphi\,(t)$$

Equation 23

$$D_{2B}(t) = \hat{b}_{12}^2(t)I_O(t-t_1) + \hat{b}_{22}^2 I_O(t-t_2) + 2\hat{b}_{12}\hat{a}_{22}\sqrt{I_c(t-t_1)I_c(t-t_2)}\sin(\varphi(t)-\varepsilon)$$

Equation 24

The two signals in pairs are subtracted and result in two signals:

$$D_x(t) \equiv \eta_{1A}D_{1A}(t) - \eta_{1B}D_{1B}(t)$$

$$= \left[\eta_{1A}(\hat{a}_{11}^2 + \hat{a}_{21}^2) - \eta_{1B}\left(\hat{b}_{11}^2 + \hat{b}_{21}^2\right)\right]I_O(t) - 2\left[\eta_{1A}\hat{a}_{11}\hat{a}_{21} + \eta_{1B}\hat{b}_{11}\hat{b}_{21}\right]I_c(t)\cos\varphi(t) = x_o(t) - A_x(t)\cos\varphi(t) \qquad \text{Equation 25}$$

Where η is a scaling facto for each signal

$$D_y(t) \equiv \eta_{2A}D_{2A}(t) - \eta_{2B}D_{2B}(t) = \left[\eta_{2A}(\hat{a}_{12}^2 + \hat{a}_{22}^2) - \eta_{2B}\left(\hat{b}_{12}^2 + \hat{b}_{22}^2\right)\right]I_O(t) - 2\left[\eta_{2A}\hat{a}_{12}\hat{a}_{22} + \eta_{2B}\hat{b}_{12}\hat{b}_{22}\right]I_c(t)\sin(\varphi(t)-\varepsilon) = y_o(t) - A_y(t)\sin(\varphi(t)-\varepsilon)$$

Equation 26

Where $A_x(t)$ and $A_y(t)$ correspond to the time dependant amplitude respectively. The two signals describe a Lissajous. After scaling, the signal fix the Lissajous center at the origin with the output signals:

$$D_x(t) = A_x(t)\cos\varphi\,(t) \qquad \text{Equation 27}$$

$$D_y(t) = A_y(t)\sin(\varphi(t)-\varepsilon) \qquad \text{Equation 28}$$

The equation used by the reduction program to estimate $\varphi(t)$ from $D_x(t)$ and $D_y(t)$, is given by the ratio of the two output signals:

$$\tan\varphi(t) = \tan\varepsilon + \frac{y(t)A_x(t)}{x(t)A_y(t)}\sec\varepsilon \qquad \text{Equation 29}$$

After getting the phase shift from the tangent equation above, the velocity history of the moving surface can be determined using the fringe count[14,64].

$$v(t - \tau/2) = VPF \times F(t) \qquad \text{Equation 30}$$

Where $F(t)$ equates to;

$$F(t) = \frac{\varphi(t)}{2\pi} \qquad \text{Equation 31}$$

VISAR can measure velocities greater than one km/s at large velocity[7]. A successful VISAR data acquisition results from attaining good fringe contrast during the experiment. In order to get good fringes, the interferometer must receive sufficient coherent light. In the same way a continuous apparent loss of contrast may result in low electronic amplification[58].

3.4.4. Processing the recorded data

The program performs the calculations on the fringe data. Firstly, it requires to load the two quadrature fringe signals. In general, the oscilloscope saves the data in the .WFM file extension known as the Waveform Data File, therefore it is important to keep the files with the signals in the same format as this reduction program only accepts the same format. The next step after loading files to be processed is to select "VISAR" on the submenu and specify the procedure it will follow, in this case "fringe to velocity". After this step, one has to select each fringe data in the two dialog boxes Data 1 and Data 2 to have the two data files loaded and ready for processing.

After loading the data into the software, there are other important functions to consider, such as smoothing the data, adding an appropriate VPF constant and phase angle before obtaining the desired results. Smoothing assist with removing noise from the data. The phase angle is added as 90^0 phase. The VPF knob adjusts the velocity per fringe for the beam loaded. It is important to put in a VPF constant that corresponds to the etalon used during the experiment so the program produces appropriate results. The 90^0 phase shift of the two loaded signals must

also be added. Figure 3.10 shows the three knobs to , for smoothing, adding the VPF and phase angle.

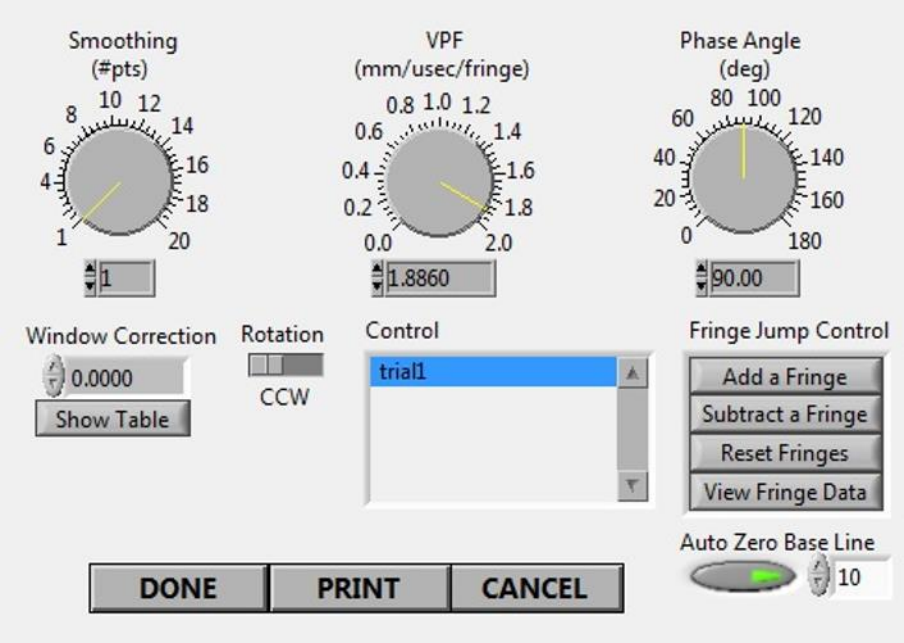

Figure 3.10: Velocity plot adjusting knobs

The three plots in Figure 3.11 would then be produced immediately after all the relative functions are considered, a plot of the fringe data (top left), circular plot (top right) and the velocity plot (bottom right). The first plot presents the fringe data, the Doppler shifted signal reflected off the reflective surface which got split into two upon entering the VISAR interferometer and shifted in phase. The second plot is the circular plot, a representation of the Lissajous graph. A plot of the two sinusoidal signal on the x and y axis that are out of phase by 90^0. The resulting velocity plot is a product of the fringe shift, a normalized difference of the phase before any shifting and the phase after shift, and the VPF constant. Upon producing the plots, the program will allow you to save the velocity information in a csv format.

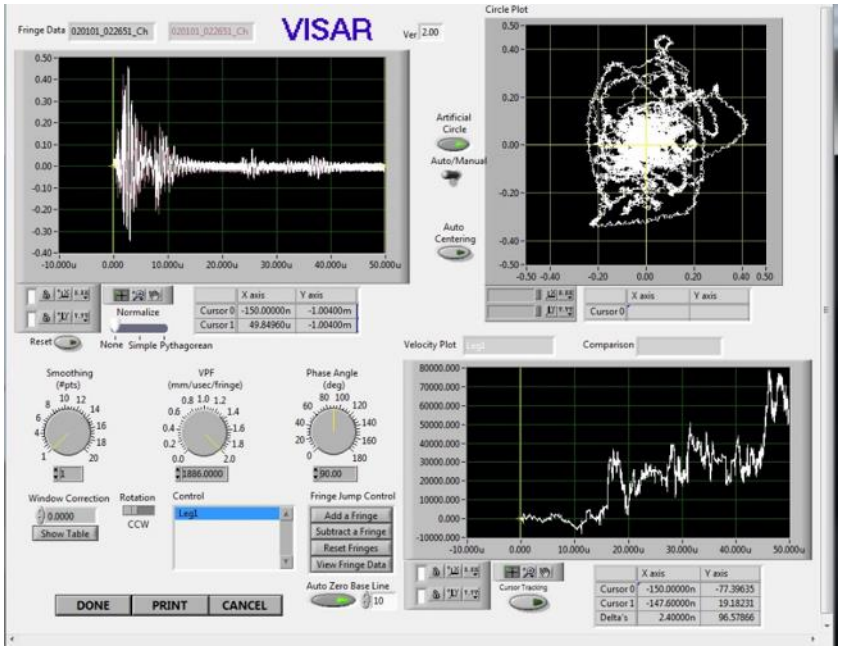

Figure 3.11: Plots obtained by the reduction program after manipulating the waveform data

In this study, only the optical velocity interferometers are discussed. However, other common diagnostics that can used to measure the expansion of the detonation driven cylinder are; high speed photography and contact pins. The high speed photography methods vary in the number of point they can gather, with the streak photography method recording 500 points and Cordin UHSC recording about 30 points. With the optical velocity interferometers, there is no need to postprocess the images after the test, a method prone to human error[13]. Hence, this is one of advantanges that the lead the VISAR to be used as the diagnostic to measure the expansion of the detonation driven cylinder during the test for this study.

Chapter 4

Methodology

4.1. Introduction

This chapter mainly describes the laboratory experiment and components that made up the entire setup in the field. The setup and execution of the cylinder tests instrumented with a VISAR at DBEL testing range are also presented.

4.2. Proof of concept experiment

The schematic of the laboratory setup is shown in Figure 4.1 . The setup consisted of the multi-beam Valyn VISAR system; that is a laser source and head, beam module, ramp generator, VISAR module and an optical probe (which launches the incident light and collects the reflected light), Tektronix DPO 7354C recording oscilloscope and a cylinder as a target as shown in Figure 4.1. The laser utilized during the laboratory test , and for the entire study, was a Verdi V-8/V10. A compact solid-state diode-pumped, frequency doubled Nd-Vanadate (Nd-YVO_4) laser that provides coherent 532 nm coherent continuous wave signal output. The power of this laser can go up to 6.5 W maximum power.

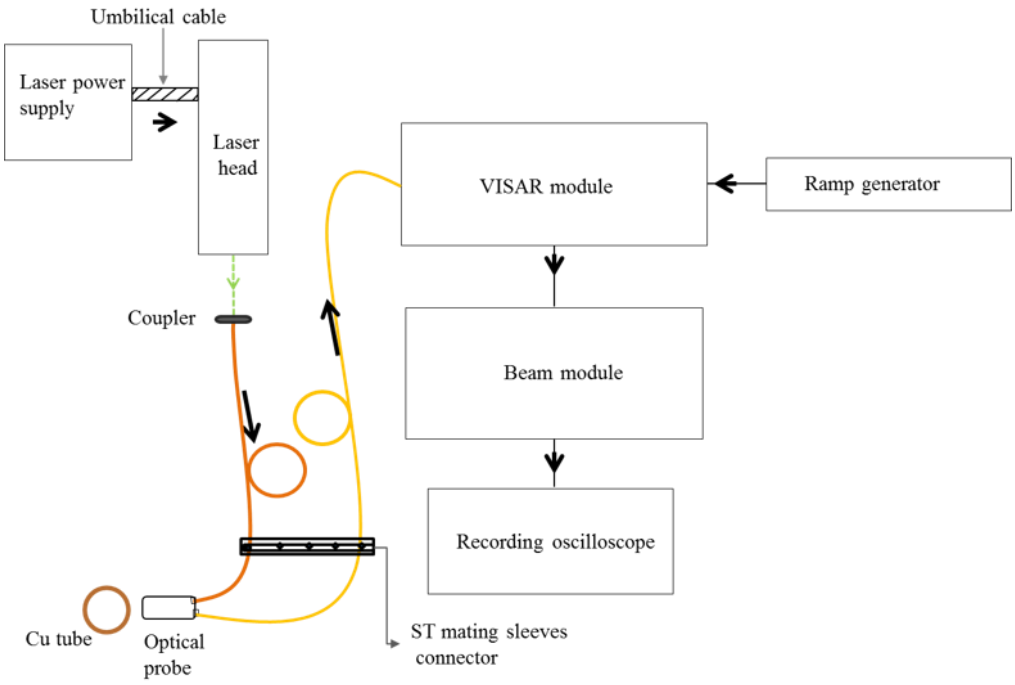

Figure 4.1: Schematic diagram of the laboratory VISAR setup (top view)

An open ended empty plumbing copper pipe (cylinder), 300 mm long and 22 mm outer diameter, was used as the target. This cylinder obviously was not an OFHC copper, however

properties of the copper were not critical at this stage since it was not going to be detonated. More importantly, the cylinder was polished so it had a reflective surface. A retort stand with a rotator was used to hold the cylinder within 30 mm or at 150 mm, depending on the probe used, from the optical probe fixed on the optical table. With the rotator we were able to tilt the cylinder left and right with respect to the opticasl probe, aiming for the correct angle at which most of the light would be reflected straight to probe. The mechanism was effective to some level. The reflected light would sometimes be intense and this was observed through an increase in intensity of the light as observed by looking at the viewing screens on the VISAR module.

At first attempt of directing the light to the cylinder, the incident light was misaligned with the cylinder, hence the probe could not collect enough light to form fringes in the interferometer. Many adjustments to the alignment were performed, simultaneously regulating the input power until a high intensity light signal was reflected to the VISAR module. When a good alignment was achieved, the beam module would display a Lissajous graph with 200 mV. This is how it was determined that the copper tube and optical probe were in alignment.. The etalon VPF constant was not important during this part of the setup. An investigation of possible signal losses within the setup was done by measuring the power of the incident beam at various points. This exercise also served as a test whether the vertical angle of polarization of the laser from the laser head was perpendicular to the lateral polarization axis of the AMBS/FC as required for a high amount of light to be split off. Incident beam with input power "P_i" was directed to the power meter detector throught three exits as shown in Figure 4.2 and measurements of output power "P_O" were taken.

In Figure 4.2, the first arrangement "A" indicates power measurement from the laser head directly. The beam was directed straight to the power meter detector. This arrangement resulted in no power losses. In "B" the beam enters to via the AMBS/FC where about 40% of the light is lost when it enters the fibre coupler according to the manufacturer, and then travels down the optical fibre which is not attached to the opticl probe. This is where output power of 'B" was measured. And lastly in arrangement "C", the beam traverse through the AMBS/FC, fibre and the optical probe which directs it into the power meter detector. The power measurements were done while improving alignment on the AMBS/FC, with the aim of reaching a typical 350 mW output power or more for an input of 1W. With adequate alignment, well defined fringes can be formed with a signal of 350 mW striking the cylinder.

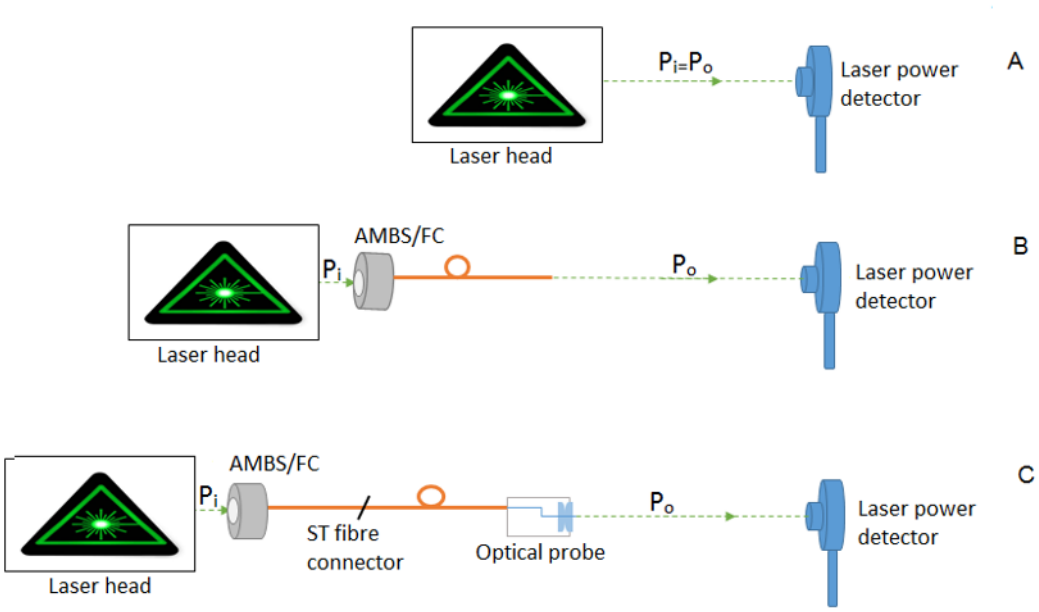

Figure 4.2: Arrangement of measuring laser light power outputs at light paths A, B and C.

The results obtained for the above arrangement are collated in Table 4.1. Table 4.1 indicates that at "A" the light had not yet entered the AMBS/FC or fibre, hence there were no losses. At "B", the losses were high at about 67% of the input power. The huge difference between the output power at "A" and "B" is due to the misalignment of the AMBS/FC with the incoming beam. The vertical axis of the incoming beam must be perpendicular to the lateral axis of the AMBS/FC in order for the beamsplitter inside the coupler to split-off as much light to the fibre directing light to the cylinder. Carrying on to "C", the power losses obtained were about 66% which is not far from the percentage losses at "B". Total losses were around 93% and were obtained by considering the input at "A" and output at "C". These measurements implied that there could still be improvement in aligning the polarization angle of the AMBS/FC in order for the high percentage of light to be split off. After improving the alignment of the coupler, the total losses could be taken down to 65% whereby an input of 1 W resulted in an output of 350 mW.

Table 4.1: Results of power measurements at different positions in the light path (see Figure 4.2)

Input power P_i (W)	**A** Output power P_O (W)	**B** Input power P_i (W) 60% of **A***	**B** Output power P_O (W)	**B** P_i-P_o (W)	**B Loss (%)**	**C** Input power P_i (W) (difference @ **B**)	**C** Output power P_O (W)	**C** P_i-P_o (W)	**C Loss (%)**	**Total Loss (%)**
1.00	1.00	0.60	0.19	0.41	**68**	0.19	0.06	0.13	**68**	**90**
1.50	1.50	0.90	0.29	0.61	**68**	0.29	0.09	0.2	**69**	**90**
2.00	2.00	1.20	0.41	0.79	**66**	0.41	0.16	0.25	**61**	**87**

* The VISAR manual reports 60-45% gain into the AMBS/FC

Combined with alignment of the cylinder, this setup yielded high intensity light that was able to produce a Lissajous plot. Even though it took some time to get sufficient reflected signal from a curved surface we took the decision to take the VISAR on site to perform a cylinder expansion test. In preparing for the cylinder expansion test, a guide-line document was written for the CSIR with a document number GLZM00-18-001 TIN Rev 1[65]. Components required for the test were designed and are explained in the next section.

4.3. Preparation of the cylinders

Six cylinders were prepared for the study. The idea with six cylinders was to compare expansion measured at different positions on the surface were a planar wave was fully developed. One of the requirements for the VISAR system to produce high intensity fringe signal is that the target must have a reflective surface. Therefore, the cylinder surfaces prepared for this study were polished to mirror-like surfaces using Brasso. The cylinders were weighed before they were filled with explosive. It is important to know the masses of the cylinders because the it is used to determine their density which is used when calculating pressure. The masses obtained are presented in Table 4.2. The cylinders were slightly different in dimensions, hence the variation in their masses. Cylinders with smaller inner diameters weighed more than the ones with larger inner diameter because of the amount of copper material extruded from them. Although all the cylinders had slightly different dimensions, they held the same properties hence behave the same way during detonation. Table 4.2 also lists other design

parameters of the cylinders. Composition B charge, commonly referred to as comp B, was casted into the six OFHC cylinders individually. Comp B is made up of 60% RDX, 40% TNT and 1% wax. After casting, the cylinders were weighed again. The net weights are also tabulated in Table 4.2.

Table 4.2: Important design parameters for the cylinders

Parameter	**Copper Tubes**					
	#1	**#2**	**#3**	**#4**	**#5**	**#6**
Inner diameter (mm)	18.00	18.80	18.97	18.86	18.87	19.00
Outer diameter/side (mm)	25.50	25.56	25.48	25.40	25.46	25.47
Wall thickness (mm)	3.75 At thinnest points	3.38	3.26	3.27	3.29	3.24
Length (mm)	300.00	308.62	305.67	305.60	307.05	307.05
Material type	OFHCH 99.992 % Cu	OFHCH 99.95% Cu	OFHCH 99.95% Cu	OFHCH 99.95% Cu	OFHCH 99.95% Cu	OFHCH 99.95% Cu
Charge shape	Square prism	Cylindrical	Cylindrical	Cylindrical	Cylindrical	Cylindrical
Empty weight (g)	950	633	623	630	628	631
Full weight (g)	1080	776	665	770	770	770

The explosive filled cylinders were examined under the X-ray machine to detect possible voids that may have formed during casting. X-ray examination was necessary before detonating the cylinders because inconsistences such as voids in the explosive can affect its performance. The cylinder was much longer than could be captured in one piece by the X-ray machine. Hence,

the entire cylinder length could not be captured at once, it was captured from the center to one end (Side A) and from the center to the other end (Side B), the X-ray combined images are shown in Figure 4.3.

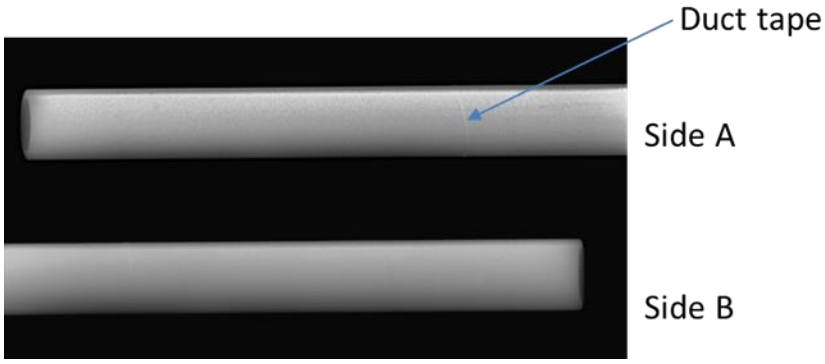

Figure 4.3: X-ray photographs of an explosive filled cylinder

The X-ray also show the duct tape which was wrapped around the cylinder surface. The X-ray confirmed no voids or any inclusions, as shown in Figure 4.3. Only one cylinder is shown since the rest of the five X-rays were similar.

4.4. Important components for the field setup

In the test setup at DBEL testing range, there were additional components that contributed to the feasibility of the main components as per the test plan. These components included wooden stand assemblies, optical probe protective assembly, cylinder holder made from plastic, protective metal plate and a steel drum “vlip”,

4.4.1. Wooden stand assembly

The design of the four legged wooden stands built to hold the cylinder was from the previous cylinder tests using Cordin UHSC. The top of the stand was modified, it had a base plug on which a plastic cylindrical holder was screwed in order to hold the cylinder steady. The inner diameter of the cylindrical holder could fit all five cylinders prepared because on the side it had a grub screw that would be tightened after putting in a cylinder. The base of the cylindrical holder and the wooden base plug were the same in diameter. These dimensions of the cylinder are already mentioned above (Table 4.2). The cylindrical holder, when screwed on the surface of the stand top, could be moved in a crosswise direction. The main idea behind this design was to make adjustments of cylinder position when aligning it with the incoming beam without the risk of losing the standoff distance. A computer aided diagram (CAD) of the stand top assembly is shown in Figure 4.4.

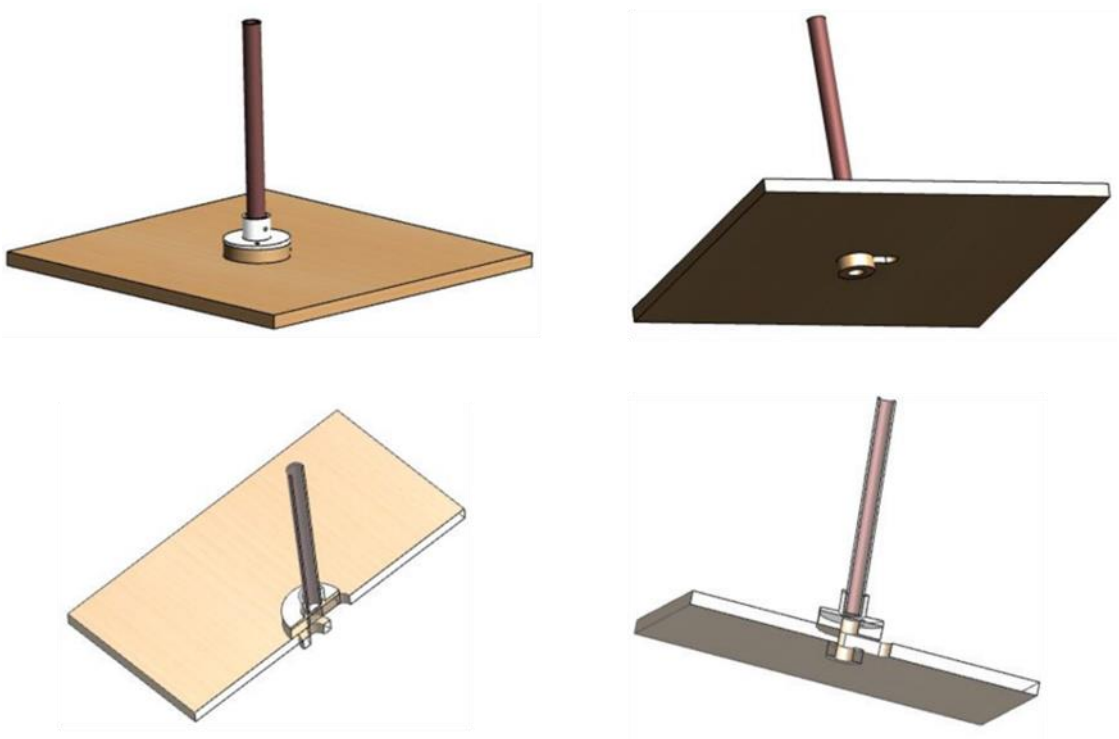

Figure 4.4: Design of the cylinder holder

4.4.2. Optical probe assembly

The VISAR system utilizes a plug-and-play optical probe to launch the incident beam to the target and the same optical probe collects the beam reflected off the surface of the target. Only three of these were available for this test while a total of six cylinders were prepared to be shot. Hence, protective measure for the optical probes was designed to save them from the blast or at least get destroyed only after they have collected the reflected light. The components of the protective optical probe assembly were, metal cylinder, polyvinylchloride (PVC) probe holder, a BK 7 glass window and its holder and a mild steel disc as shown in Figure 4.5.

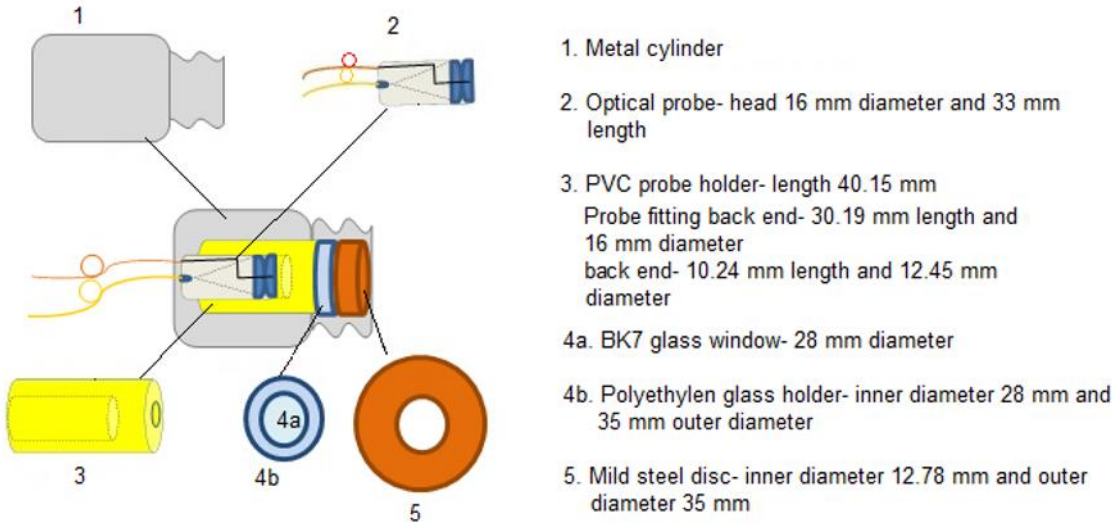

Figure 4.5: Optical probe protective assembly

In Figure 4.5 the metal cylinder (component 1) houses all the other components. Inside the PVC holder the optical probe was placed behind a BK 7 glass window which in turn was placed behind a mild steel disc. The protecting optical probe assembly was built in such a way that should the BK 7 glass window get damaged; it can be easily replaced with another one. All the components were sacrificial including the plug-and-play optical probe used.

4.4.3. Protective metal plate

A metal plate was also prepared and placed between the cylinder and the "vlip" in front of the optical probe assembly for further protection of the optical probe from possible fragments erupting towards its direction from the event.

4.4.4. The "vlip"

The "vlip" is a cylindrical steel drum, with legs of the same material, with 1525 mm length, 1500 mm internal diameter and 40 mm thickness. It is open on both ends and has been used as a semi-enclosed environment for explosion performances. In the center of its wall, there are four equally spaced openings of the same diameter. These openings normally hold pressure assemblys during explosive tests aiming at measuring detonation pressure. One of the openings, during our experiment was used to hold the optical probe assembly. The "vlip" not only served as the optical probe holder during the experiment but also protected the fibres against shock wave produced during the event. Knowledge from previous explosive tests performed inside the "vlip" gave us confidence that it was also explosive proof to the net weight of explosive used in the cylinder test. The "vlip"- cylinder setup is shown in Figure 4.6.

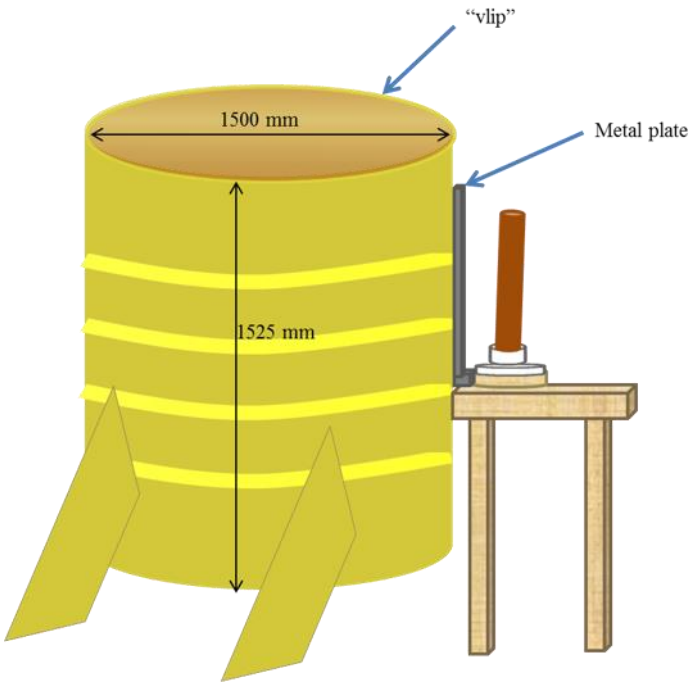

Figure 4.6: Side view of the "vlip" setup

4.5. Field experimental setup

The test was executed at CSIR DBEL testing range according to the Standard Operating Procedure (SOP) from previous years of perfoming the cylinder expansion test at the DBEL, together with the SOP of the VISAR system as used in the laser laboratory at the CSIR National Laser Cetre (NLC). A conceptual layout of the test is shown in Figure 4.7. The test was performed at T7 shelter which housed two recording oscilloscopes and the VISAR system. Outside the shelter was the optical probe with 150 mm working distance, cylinder and supporting components as shown in Figure 4.7.

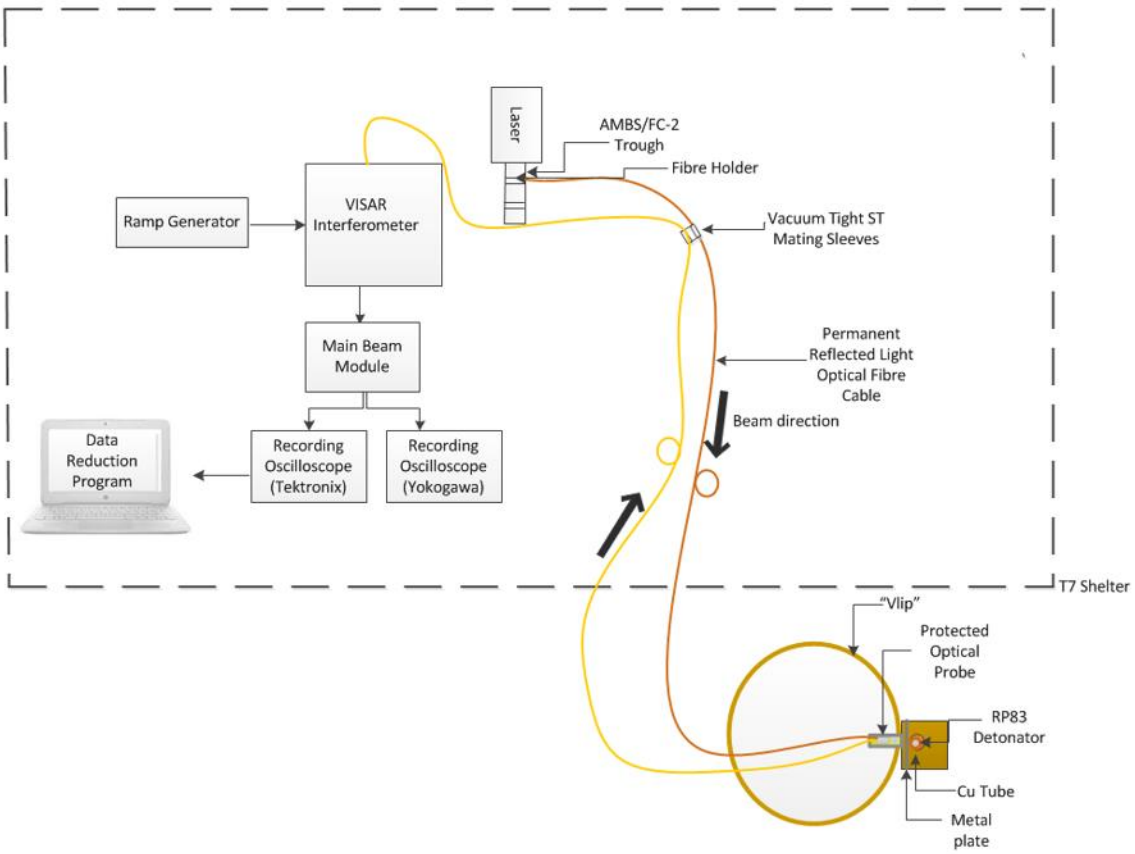

Figure 4.7: Instrumentation set-up with the VISAR

The incident light was launched from the laser head through optical fibres to the optical probe and eventually to the cylinder. Similarly the reflected light was collected from the cylinder surface by the same optical probe to the VISAR module through optical fibres. The fibre cables were running on the floor between the two end connections with over half of its length lying on the ground outside the shelter. These fibre cables (incident and reflected fibre cables) were covered by sand bags as protection against the shock wave from the explosion. The optical probe assembly, with the probe assembled, was mounted on the “vlip” from the inside at 1515 mm height from the ground, with the probe lens facing outside as shown in Figure 4.8.

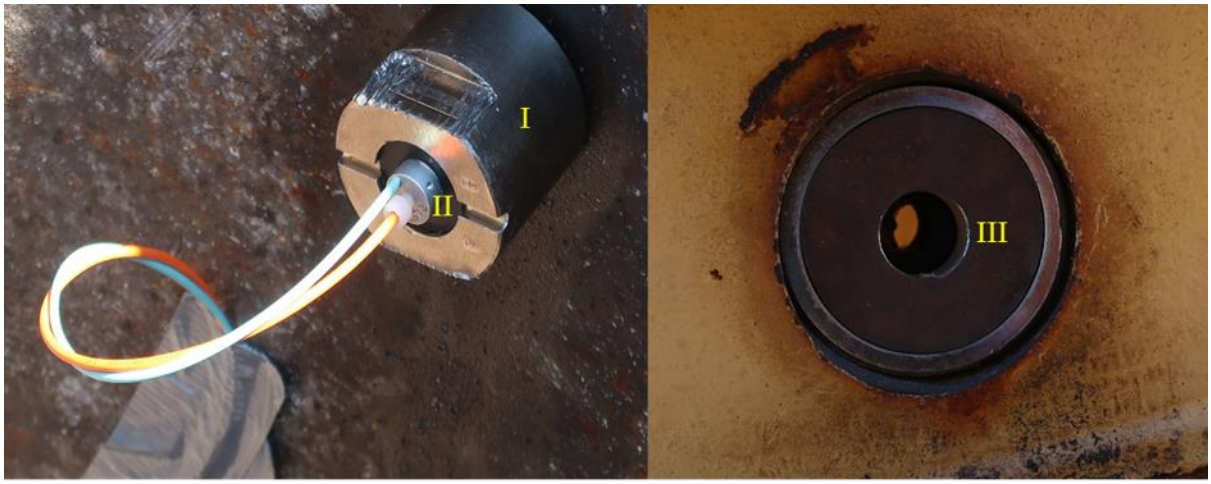

Figure 4.8: (a) Optical probe assembly inside the "vlip" showing the metal cylinder confining other components I and an optical probe II , (b) Optical probe assembly on opposite side of the "vlip" wall, showing the mild steel disc in front of the BK 7 window III.

In front of the “vlip” wall where the probe was facing there was a wooden stand assembly. A metal plate with a circular opening of the same diameter as the steel disc at the centre was placed against the “vlip” wall on the wooden stand between the probe and plugged cylinder holder. This plate was constructed to enhance protection for the probe against fragments. An example of the above mentioned arrangement is shown in Figure 4.9 before the cylinder was placed.

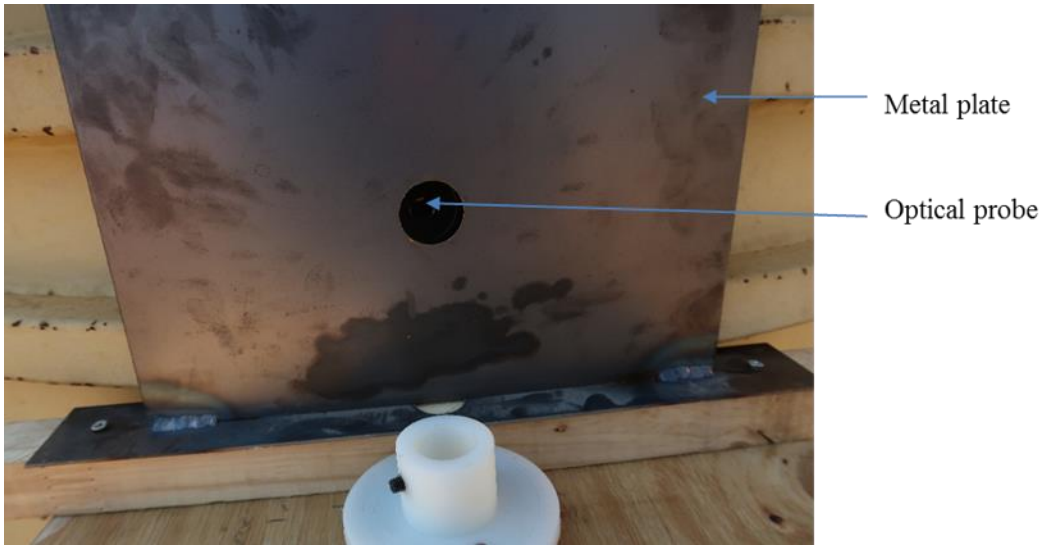

Figure 4.9: View of the optical probe outside the "vlip"

Pre-test calculations were done to determine the time of arrival of the shock wave at the point of interest on the cylinder surface. The shock arrival times between the distances specified in Figure 4.10 were determined using theoretical velocity of detonation of both booster and comp B charge and the distance from the detonator to the observed position on the cylinder. That is, T0 to T3 in Figure 4.10.

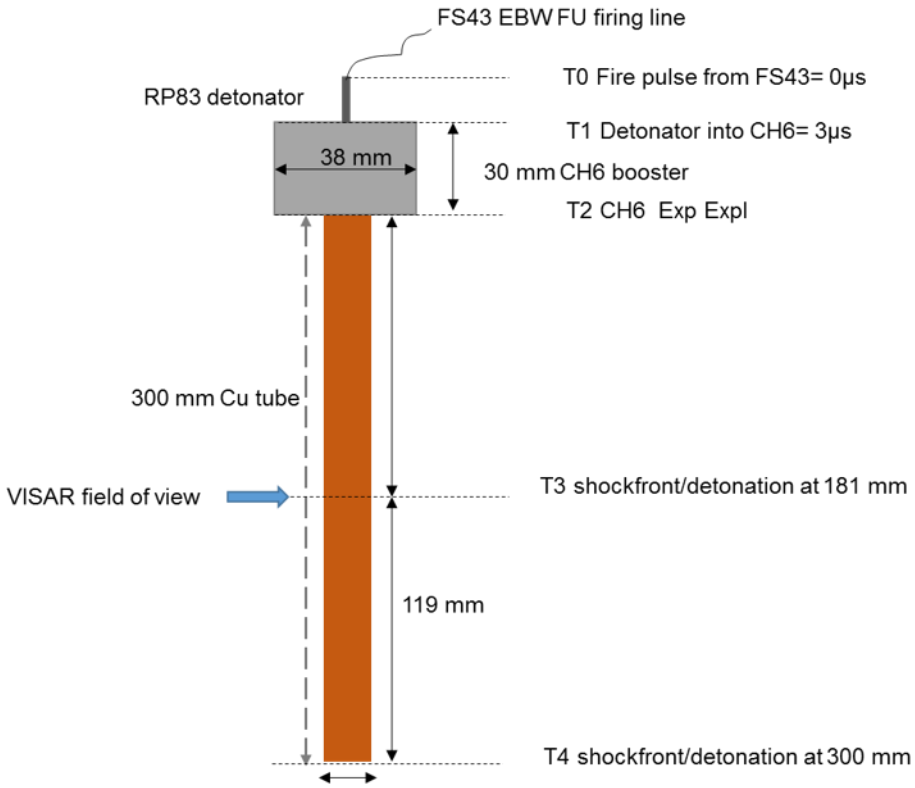

Figure 4.10: Shock front arrival times

$$T1 = 3\ \mu s \qquad \text{Equation 32}$$

$$T2 = \frac{L}{VOD\ (CH6)} = \frac{30\ mm}{8.3\ mm/\mu s} = 3.6\ \mu s \qquad \text{Equation 33}$$

$$T3 = \frac{L}{VOD\ (Comp\ B)} = \frac{181\ mm}{7.9\ mm/\mu s} = 22.9\ \mu s \qquad \text{Equation 34}$$

Therefore, the expected arrival time of the shock 181 mm from the point of detonation was given by the summation,

$$T1 + T2 + T3 = 29.6\ \mu s \qquad \text{Equation 35}$$

Data recording diagnostic that made available for the test were two recording oscilloscopes, a Tektronix DPO 7354C and Yokogawa DL850. The Tektronix has a sampling rate of 3.5G S/s and samples at 40G Hz frequency. The Yokogawa has a sampling rate of 100 MS/s and samples at 500 MHz frequency. Due to the absence of a delay generator during testing day, both oscilloscopes were set to record the entire event, from the point of detonation to the end for 50 µs. This duration time for the cylinder expansion test was recorded from previous cylinder tests perfomed at DBEL. Although both oscilloscopes recorded the entire event for the same duration, their recording length varied because they were sampling at different rates. Tektronix was sampling at 3.5 GS/s and Yokogawa at 100 MS/s. Hence, theoretical record length for the Tektronix was calculated to be 175000 samples and 5000 samples for Yokogawa as follows:

$$\text{record length}(S) = \frac{\text{measured duration (s)}}{\text{sampling rate (S/s)}} \qquad \text{Equation 36}$$

$$\text{Tektronix:record length } (S) = \frac{50\ \mu s}{3.5\ GS/s} = 175000\ S \qquad \text{Equation 37}$$

$$\text{Yokogawa:record length } (S) = \frac{50\ \mu s}{100\ MS/s} = 5000\ S \qquad \text{Equation 38}$$

4.5.1. Cylindrical copper tube expansion experimental setup

A cylindrical tube filled with comp B charge with dimensions 308.62 mm length and 25.56 mm outer diameter was set on the wooden stand in the cylindrical plastic holder. The cylinder was at 150 mm distance away from the optical probe. Like in the laboratory, the main obstacle with this setup was alignment. Alignment was more difficult than in the laboratory because of sunlight glare entering the probe. As much as we worked with the lights on in the laboratory, we had an option of switching them off to best align the cylinder. In the field there was high glare of sunlight on the cylinder and we did not have proper measures to block it.

This setup ended up not succeeding because it required a lot of time to align the incident beam with the cylinder in the sunlight. Since time was a factor in this study, we had to abandon the cylinder and rather used the flat surface. The square prism OFHC copper tube was filled with the same comp B. The extrusion in the square prism was cylindrical with the same average diameter as the rest of the cylindrical OFHC copper tubes. As mentioned before, it was much easier to align a flat surface than a curved surface.

4.5.2. Square prism tube expansion test

Figure 4.11 shows an explosively filled square prism tube made from copper, set on a wooden stand against the “vlip”. In this section, unless stated otherwise when referring to “tube”, an alternative to “cylinder”, it is always meant square prism tube.

Figure 4.11: Setup of the copper tube against “vlip” wall

On the top open end, the tube was overlaid with a CH6 booster which is a mixture of 97.5% RDX, 1.5% calcium stearate, 0.5% polyisobutylene and 0.5% graphite. An RP83 detonator was inserted through the booster cap. A close-up schematic representation of a booster-detonator on a square prism tube is shown in Figure 4.12.

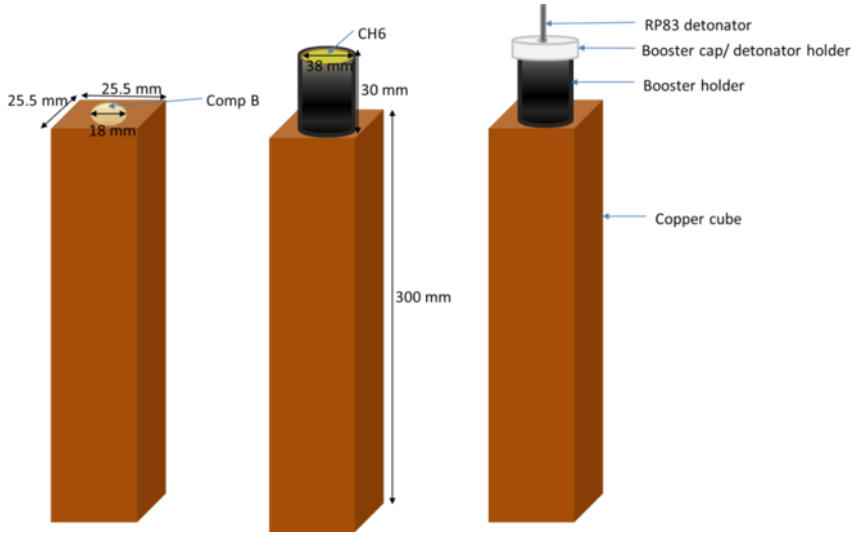

Figure 4.12: Setup of the copper tube with booster and detonator

A booster gets initiated by the detonator which eventually initiates the main charge in the cylinder. The use of a booster also assists in obtaining a planar shock front rather than a curved front when it fully develops inside the cylinder. The overlaid tube was set on the wooden stand to prepare for detonation. There was no holder designed for the tube, only for cylinders. A piece of plank that was used to lift the metal plate so that the circular opening was inline with the optical probe, also served as a platform on which the tube was laid. Inside the shelter the VISAR system together with the two recording oscilloscopes were set. To improve sensitivity, an etalon is chosen according to the principle that the VPF constant of the etalon must be equal to about half the total velocity being measured from the event. As the square prism was non-standard, no etalon was used. The plan was to compare the results obtained from the first shot (square prism) with the second shot of standard parameters (cylinder) in which an etalon was going to be used. Unfortunately there was no second shot.

Even with the square prism the intensity of the reflected light was weak, because no Lissajous graph could be plotted at first. Manual adjustment of the tube with the incident light was required to optimize the intensity of the signal. Even some little misalignment could not be tolerated because the signal had to be strong enough to produce a Lissajous plot. However, after considerable adjustments and makeshift screening of sunlight a signal confirming the VISAR system was ready was achieved and a Lissajous plot was finally produced. An FS43 firing system was used to trigger the oscilloscopes. The same system also initiated the detonator. Both oscilloscopes were connected to the FS43 firing system through a trigger box. In both oscilloscopes used, one channel was responsible for the trigger signal and two channels recorded the data. A trigger box connection is standard at DBEL test range for the safety of electronic components in the same line of connection. Between the FS43 firing system and the RP83 detonator was a firing module. The firing module allows long distance and remote firings. The schematic presenting the firing system is given in Figure 4.13.

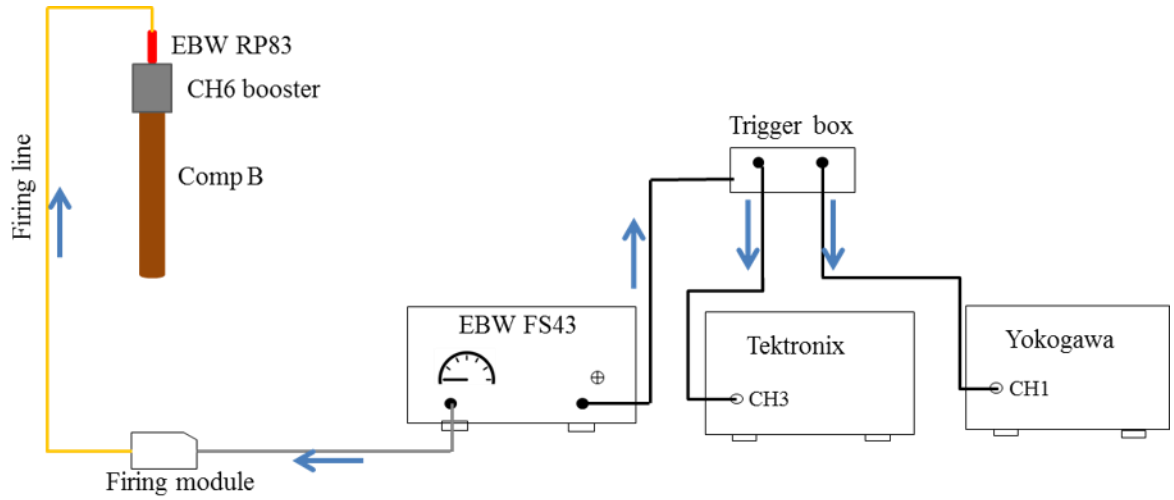

Figure 4.13: Firing sequence

At a firing voltage of 3500 V of the FS43, the detonator initiated the booster and eventually initiated the main charge in the tube; oscilloscopes were triggered and started measuring. Results were saved in a computer drive. Both the oscilloscopes were set to record the entire event, from the point of detonation to the end at 50 µs. Tektronix oscilloscope, which was the primary oscilloscope of the event recorded 125000 points of 2,5 GS/s at 0.4 ns sampling interval. The second oscilloscope, Yokogawa, samples at a rate of 100 MS/s and at 200 MHz frequency. This oscilloscope recorded 5005 points in total for he entire event.

4.6. Alignment of the cylinder expansion test

The cylinder expansion test with the VISAR as the measuring tool was setup at DBEL testing range. As mentioned in section 4.5, the optical probe together with the cylinder were outside the shelter. The tube that was used in the beginning of the setup was cylindrical (see section 4.5.1). Two factors that created challenges with aligning the cylinder with this geometry were incoherent light coming from the surrounding and the mechanism used for positioning the cylinder on the prepared stand. The challenges with alignment resulted in much time being spent on the cylinder-probe setup in a hope of collecting enough reflected signal. However, the alignment was not successful and this resulted to the use of a square prism.

Several efforts were made to improve the light signal reflected off the cylinder, such as increasing the power of the incident beam and disconnected the optical probe fibre and the fibre permanently connected to the VISAR module. During the exercise of improving the intensity of light reflected off, the connection between the reflected-light fibre of the probe and the fibre going to the VISAR module was disconnected. The light reflected off the cylinder was shone

on the white paper and with bare eyes, it was observed that the colour of the light reflected was the 532 nm green light. Light observed was more of whitish in colour, which showed that there was incoherent light on the way of the green desired light. This was an indication that the optical probe was misaligned with the cylinder and as a result the glare of sunlight bouncing off other objects in the surrounding was interfering with the laser light.

As the reflected light was shone into the white paper, the cylinder-probe alignment was being improved while maintaing the working distance 150 mm between the probe and the cylinder until more of a green light was observed on the paper. The fibres were connected back and the reflected light was directed to the VISAR module again. Another challenge encountered was with the intensity of light not increasing as the input power was being increased. This was also observed on the screens in the VISAR module. When the laser was still warming up, there was power cut-off which unexpectedly stopped the process of warming up. During the test there was no power conditioner nor voltage regulator connected to the laser. The laser was not protected from any voltage spikes. Hence it was suspected that might be the reason for no response in the intensity of the light as power was increased.

Since, the intensity of laser light to the cylinder could not be increased the only option was to improve the alignment in order to capture as much reflected light as possible. This aligning exercise was very tedious because there was no proper mechanism for shifting the copper tube in extremely small amounts and there was too much sunlight which made alignment to be difficult. After some time of alignment adjustments, the cylinder eventually reflected acceptable intensity of the laser light using power output of 3 W. The formed light fringes were also tuned before removing screens to check for the Lissajous graph on the AMO. The Lissajous graph was plotted using 20 mV voltage setting per division on the AMO was as shown in Figure 4.14. This signal was 20% of the typical 100 mV signal achieved during proof of concept in the laboratory.

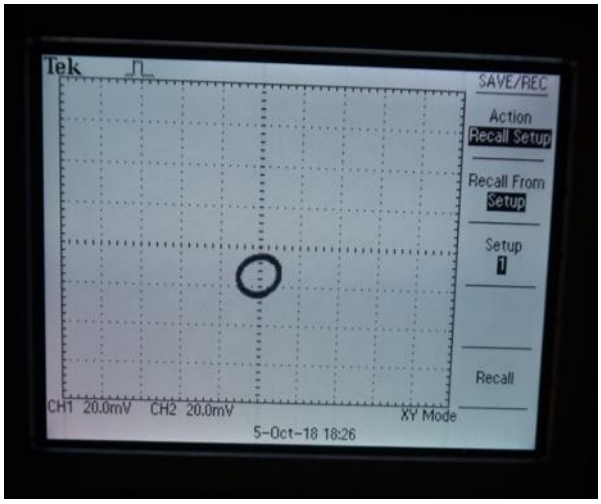

Figure 4.14: Lissajous graph observed at 3W power output

Adjustments on the Lissajous were also challenging to keep it at the centre. When there was zero voltage displayed on the AMO, the center point would remain at the center. The moment voltage adds in the form of a Lissajous, it would shift down below the x-axis. This behaviour showed that the vertical control of the Differential Amplifiers was unstable. As soon as the Lissajous was formed, the explosive engineer went on to cap the cylinder with both the booster and detonator. The slight movements made on the cylinder during overlaying resulted in the Lissajous being unstable and reducing in size. Overlaying the booster did not have much effect on the signal but inserting the detonator reduced the signal in great amounts. The insertion of the detonator into the booster needed to be done with care and precision so the detonator transfers all the energy to the booster and the booster does the same to excite the Comp B main charge. Figure 4.15 shows the Lissajous graph that resulted after inserting the detonator.

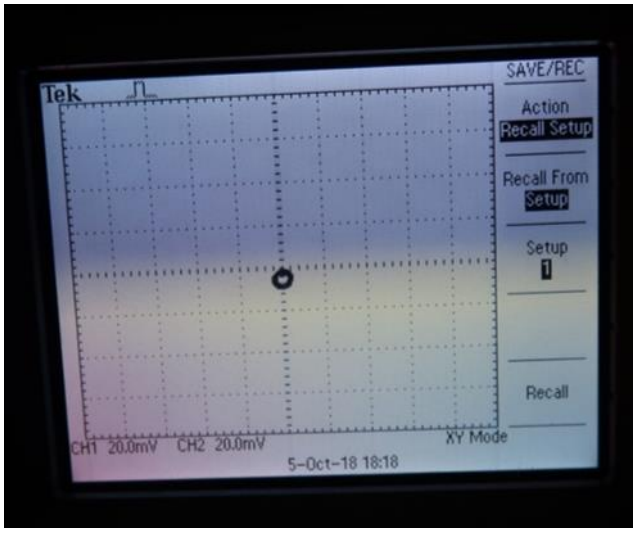

Figure 4.15: Lissajous graph after over-laying booster and detonator

The operating procedure of the VISAR suggests that, the test should not continue if the Lissajous is not stable. However, after the insertion of the detonator the Lissajous had reduced drastically, and there was no chance to go back and improve the alignment as it was highly risk to do so. Also, there was no remote method to correct the alignment. Hence, as much as the Lissajous showed non-optimal behaviour, it was almost stable and it was decided to fire the first shot despite this. The oscilloscopes were triggered and recorded the first set of data. On the following day of the test, the same setup was used to resume the cylinder expansion test. This time, a signal conditioner was connected between the generator and laser power supply.

A blank black plastic tent was brought along to cover the setup outside the T7 shelter from sunlight glare. The setup consisted of a cylindrical tube as the target. The procedure for aligning the incoming beam with the cylinder was repeated while the cylinder- probe setup outside the shelter was covered from possible incoherent light around the setup. While the alignment was improved compared to the initial cylindrical tube alignment but unfortunately the beam module was not responding at all. Several attempts at troubleshooting the setup and in the VISAR beam module were done, but with no success. The planned second cylinder expansion test was aborted which resulted in having only one set of data. The VISAR system was brought back to the laboratory for thorough evaluation and to allow the PMTs to recover. Within the scope of this study, it was not possible to schedule another test.

Chapter 5

Results and discussions

5.1. Introduction

In this study, only one shot was effectively performed. Only the square prism tube was shot. As mentioned in the methodology, the square prism used had a cylindrical extrusion which was filled with comp B explosive. This chapter presents and discusses the test results. Furthermore, the challenges related to the test and analysis of the results are also addressed.

5.2. Results

5.2.1. Software Analysis of the Recorded Results

Figure 5.1 (a) shows the fringe signals recorded by the Tektronix oscilloscope from the cylinder expansion test. The total number of points recorded that produced each fringe signal was 125000 for 50 μs. the time interval between each point was 0.4 ns. These fringe signals were loaded in the data reduction programme which produced the velocity plot in Figure 5.1 (b) by computing the velocity using the relation;

$$v(t - \tau/2) = VPF \times F(t) \qquad \text{Equation 39}$$

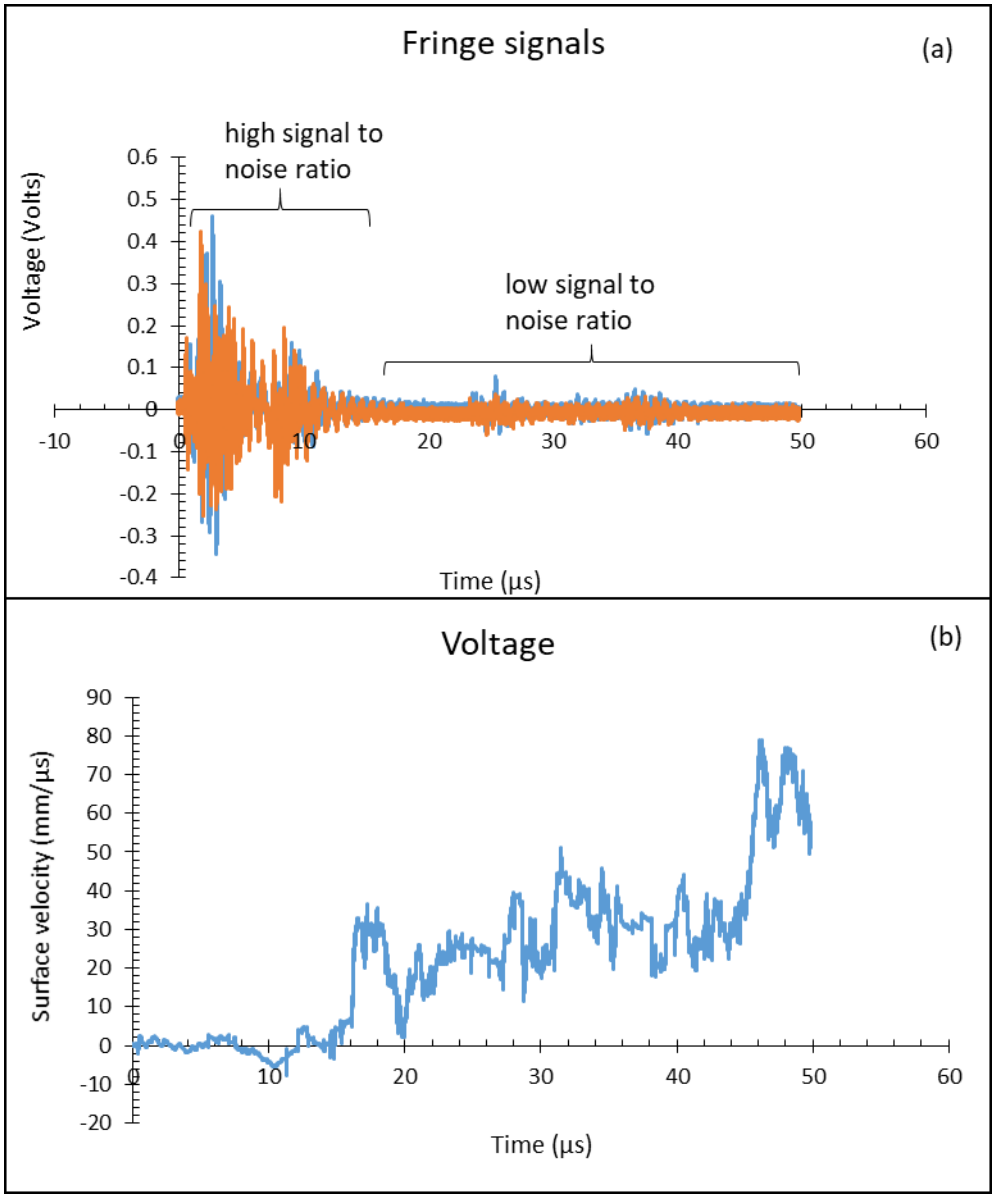

Figure 5.1: (a) Fringe data and (b) Velocity time graph produced by the VISAR Push-Pull Reduction program from the fringe data

The velocity data from the cylinder expansion test is showing many rapid changes as observed in the profile shown in Figure 5.1 (b). It can also be seen that the velocity profile has very small values for the first 0.5 µs as shown in Figure 5.2 (a). After this time, it starts to increase slightly. At about 9 µs the curve goes down to the negative velocity and it picks up again at about 12 µs after detonation. Figure 5.2 (b) is showing a sharp increase in the velocity around 16 µs. Also, this sharp increase goes up to 3800 m/s, whereas the expected maximum velocity for the comp B charge used during the cylinder expansion test is 3000 m/s. For longer times the velocity increases but at unreal values.

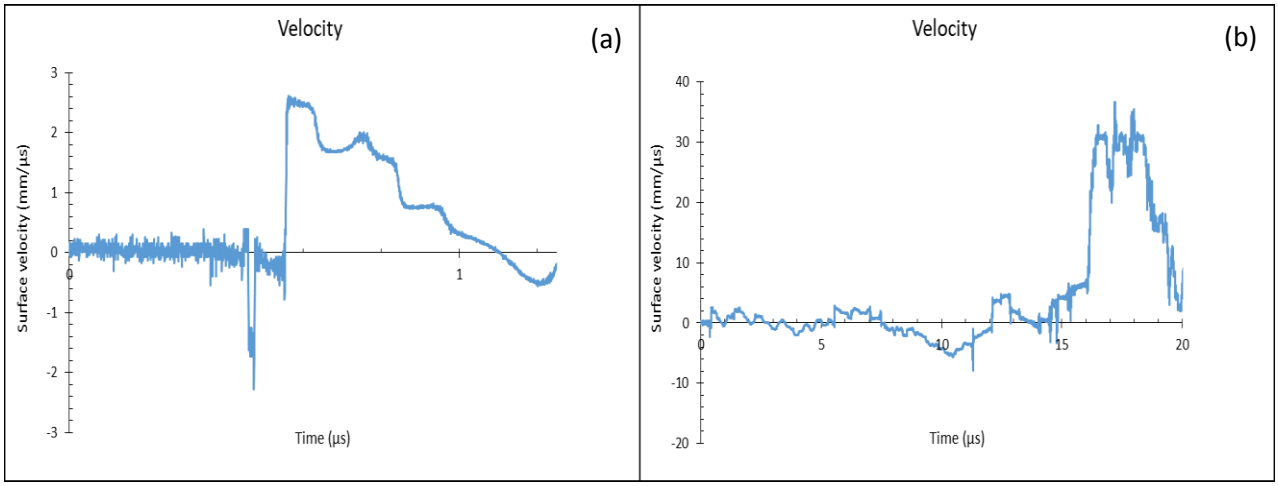

Figure 5.2: (a) surface velocity of the cylinder in the first 0.5 µs of the cylinder test (b) surface velocity of the cylinder in the first 10 µs of the cylinder test

The displacement graph of the expanding cylinder was also obtained from the data reduction program (see Figure 5.3). Displacement profile shown remains around zero values for the first 16 µs, beyond this time it increases monotonically. The displacement value beyond 150 mm are unphysical as the space between the optical probe and the cylinder was 150 mm. Hence, it was not possible for the optical probe to collect reflected laser light beyond this distance and this data has to be considered unreliable for the magnitude of velocity and displacement. As it is observed, the cuve is not perfectly smooth, it has small bumps that imply some rapid changes in the expansion. It also shows a change of slope at about 48 µs in expansion, beyond this time the slope is steeper. Another slight change variation in the slope is observed between 18 µs and 20 µs. The time calculated for the arrival of the shock wave at the point of interest was about 30 µs (see Equation 38) and as observed on the curve, the increase in the expansion started as early as 16 µs. The shock wave inside the cylinder was about two times faster than expected but offsets of a 15 µs are not totally unexpected.

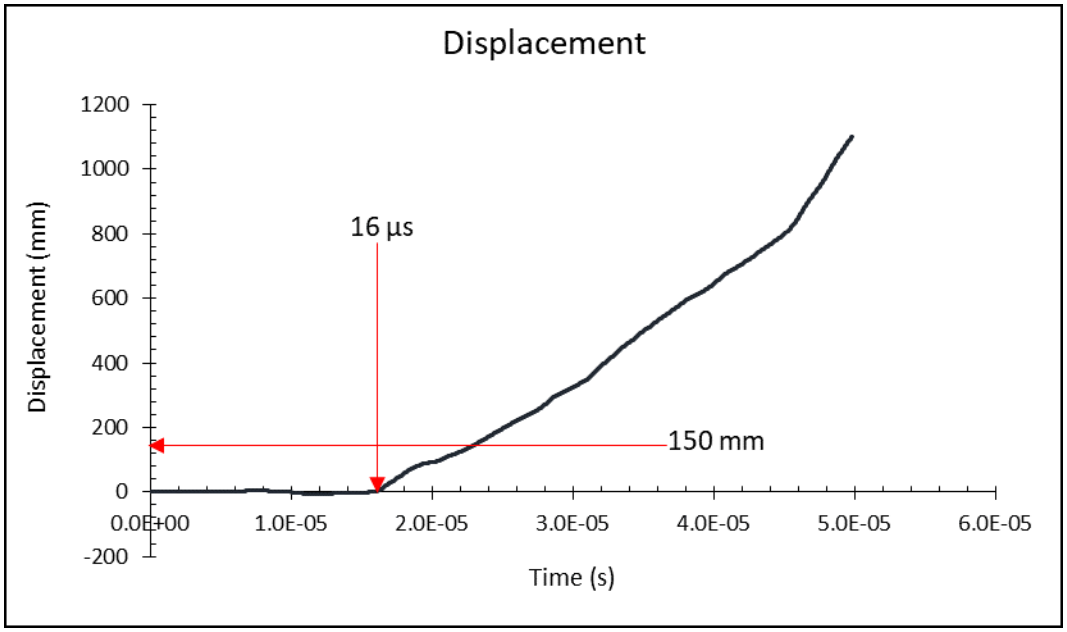

Figure 5.3: Cylinder wall expansion results for 50 µs obtained from the reduction program

The displacement profile produced was compared to the reported displacement profiles (Peter et al[6] and Polk[21]). Based on our own intuitive observation, these two displacement profiles from literature are normalized such that the expansions look like it began at zero and the starting points in the expansion that were plotted are about 1 and 2 µs, respectively. According to Figure 5.3, the arrival time for the shock wave is estimated to be 16 µs. Using this value as the beginning of the expansion, the VISAR data is featured in Figure 5.4 with the results of Peter[6] and Polk[21] displacement curves. The displacement profiles are showing a similar behaviour which implies a similar behaviour of a shock wave traversing inside the cylinders. The CSIR UHSC and the LLNL streak photography results are showing a similar rising time while the VISAR is much faster than the two photography methods.

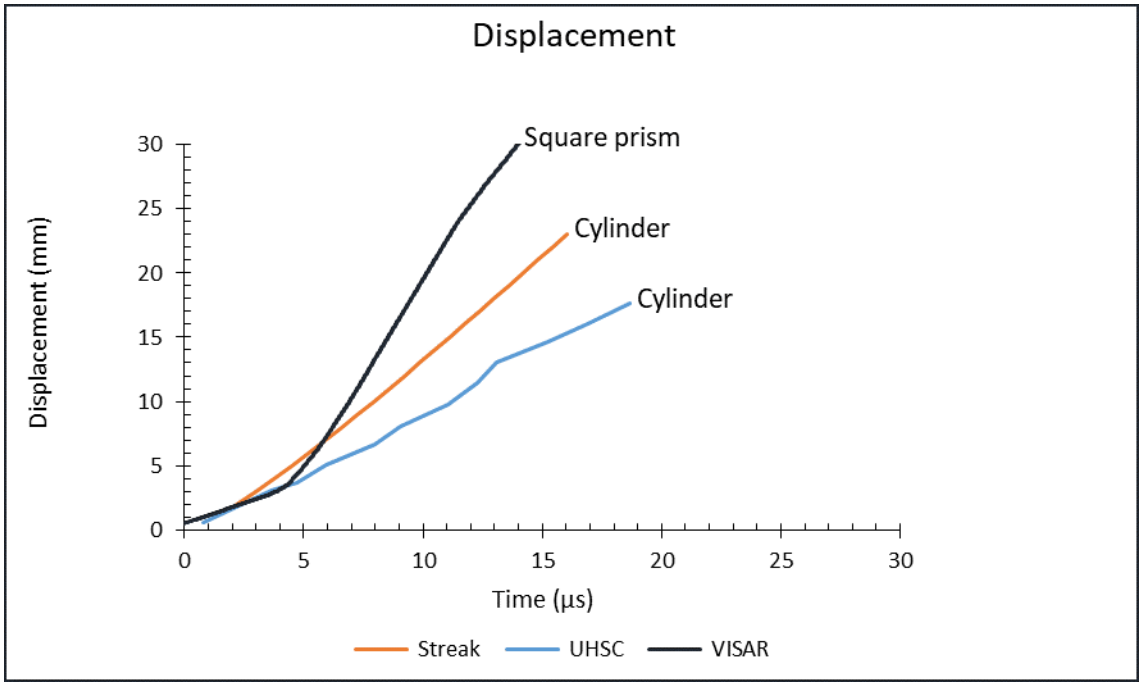

Figure 5.4: Cylinder expansion test wall displacement results extracted from LLNL[21] and CSIR images and displacement obtained from the reduced velocity results of the VISAR

Since the velocity values of the cylinder expansion test result presented are extremely high, especially at low signal to noise ratio and also the displacement values obtained are unphysical; it was necessary to understand the calculations behind the Push-Pull VISAR in detail. This motivated us to perform the calculations independently. The equations that were used to manually calculate the velocity were adopted from the work of Dolan[14] and Amit et al[64].

5.2.2. Hands-on Analysis of the recorded data

The VISAR Push-Pull data reduction program is based on a set of mathematical equations. As mentioned in chapter two, these equations basically represent the fringe shift and VPF constant related to the etalon used during the experiment. And also contain the equations that represents the signal of the PMTs. In this study, hands-on calculations were first performed to reproduce the data set presented in literature by Amit et al[64] and the aluminium square discs experimental results obtained in the laboratory at the CSIR. The work by Amit et al[64] demonstrated the fundamental equations that lead to obtaining the surface velocity signal using Equation 30 mentioned in section 5.2. In addition, the study also presented the quadrature fringe signals and the the resulting free surface velocity signal.

Amit et al's work did not have the data set tabulated, only the plots shown in Figure 5.5 were published. In the interest of this study, a digitiser was used to extract data from the fringe graph

in the study. The points were extracted by mouse clicks, hence the time intervals were not equally spaced as they are in the original plot. Furthermore, the two data sets needed to be based on a common sampling rate. Therefore another program was used to extrapolate points that fixed the gap in the time intervals. The extracted data (see Figure 5.6) was fitted in the hands-on calculations to produce the velocity time graph shown in Figure 5.7.

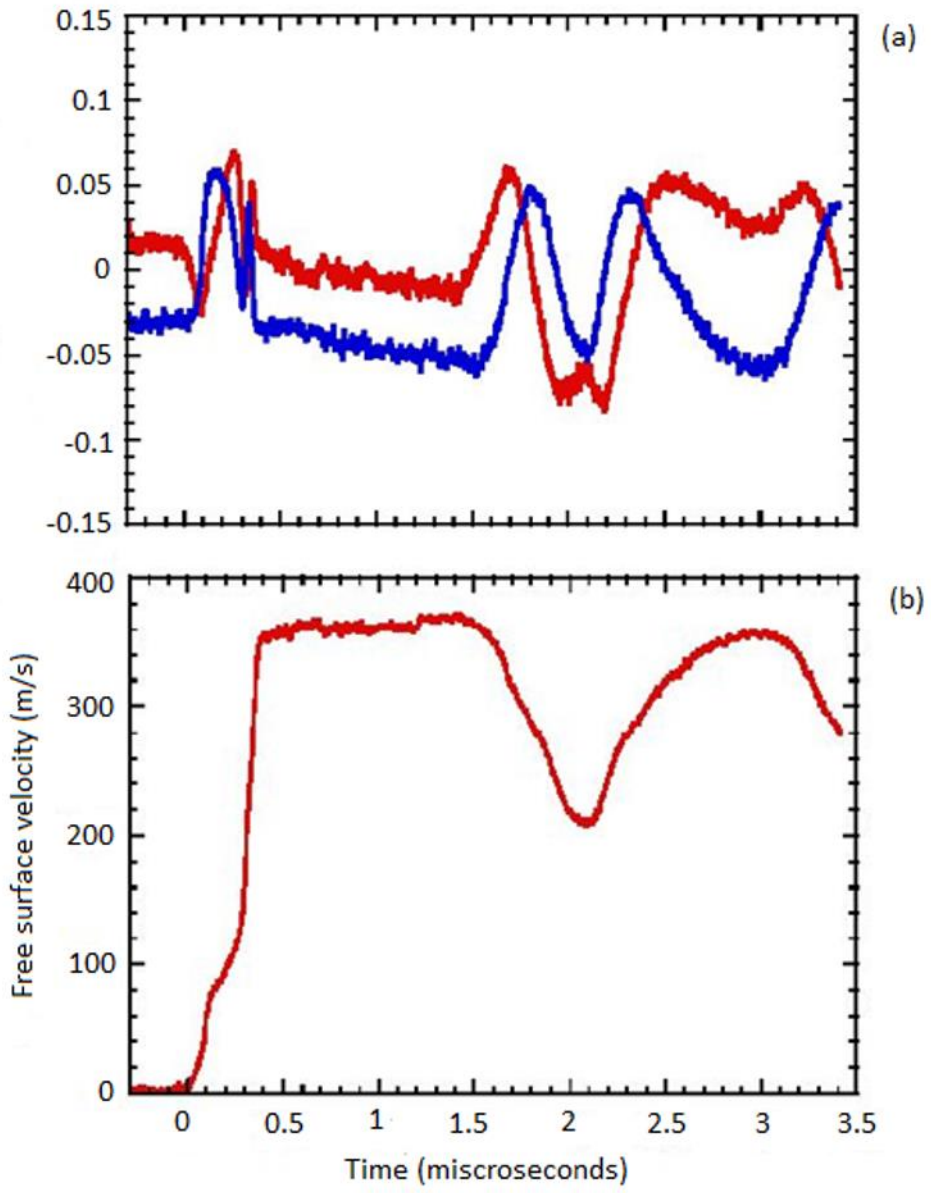

Figure 5.5: Original curves from the work of Amit et al (a) quadrature fringe signals (b) velocity results (Adopted from[64])

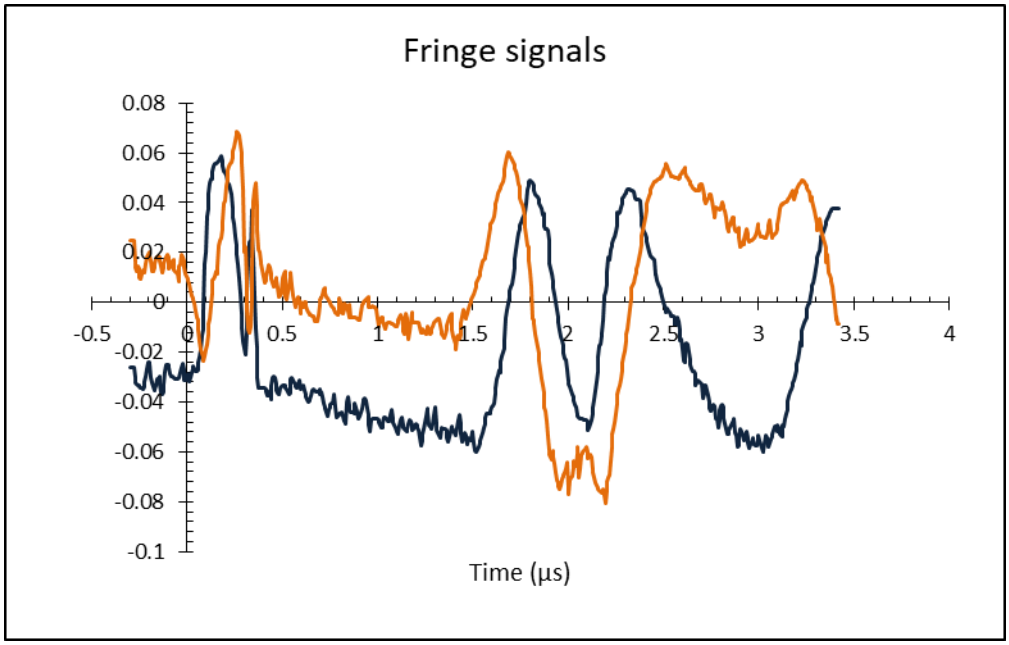

Figure 5.6: Quadrature fringe signals extracted from the work of Amit et al

The fringe signals amplitude in the original curve (Figure 5.5 (a)) lies below 0.1 and above 0.05; the extracted fringe signals (Figure 5.6) also show similar amplitude as well as matching time scales were achieved. In the equations for quadrature fringe signals, there is a variable called quadrature error (ε). Quadrature error basically describes how imperfect is the Lissajous figure and how far it is from π/2 phase difference formed by the two quadrature signals. For this data the quadrature error was assumed. After performing the calculations on Amit's data, the first velocity graph obtained (see **Figure 5.7** (a)) gave the impression that there could be a possibility of what is called the "2π ambiguity" in the fringe signals.

This occurs when there is a jump after a fringe cycle and 2π is added resulting in wrapped ϕ phases. A situation where by the phases obtained have a range of π radians in the 2ϕ integer, therefore the value of ϕ integer is off by some multiple of π/2 radians. Since the data point were not as many, it was easy to spot the jumps and correct them by making adjustments on the phases. After the correcting the jumps, both the original curve and the one obtained from hands-on calculations (**Figure 5.5** (b) and Figure 5.7 (b)), gave similar velocity profiles. These surface velocity curves show a flat ringing steep just above 350 m/s from 0.4 µs to 1.6 µs. The velocity from this time decreases and picks up again at 2.1 µs.

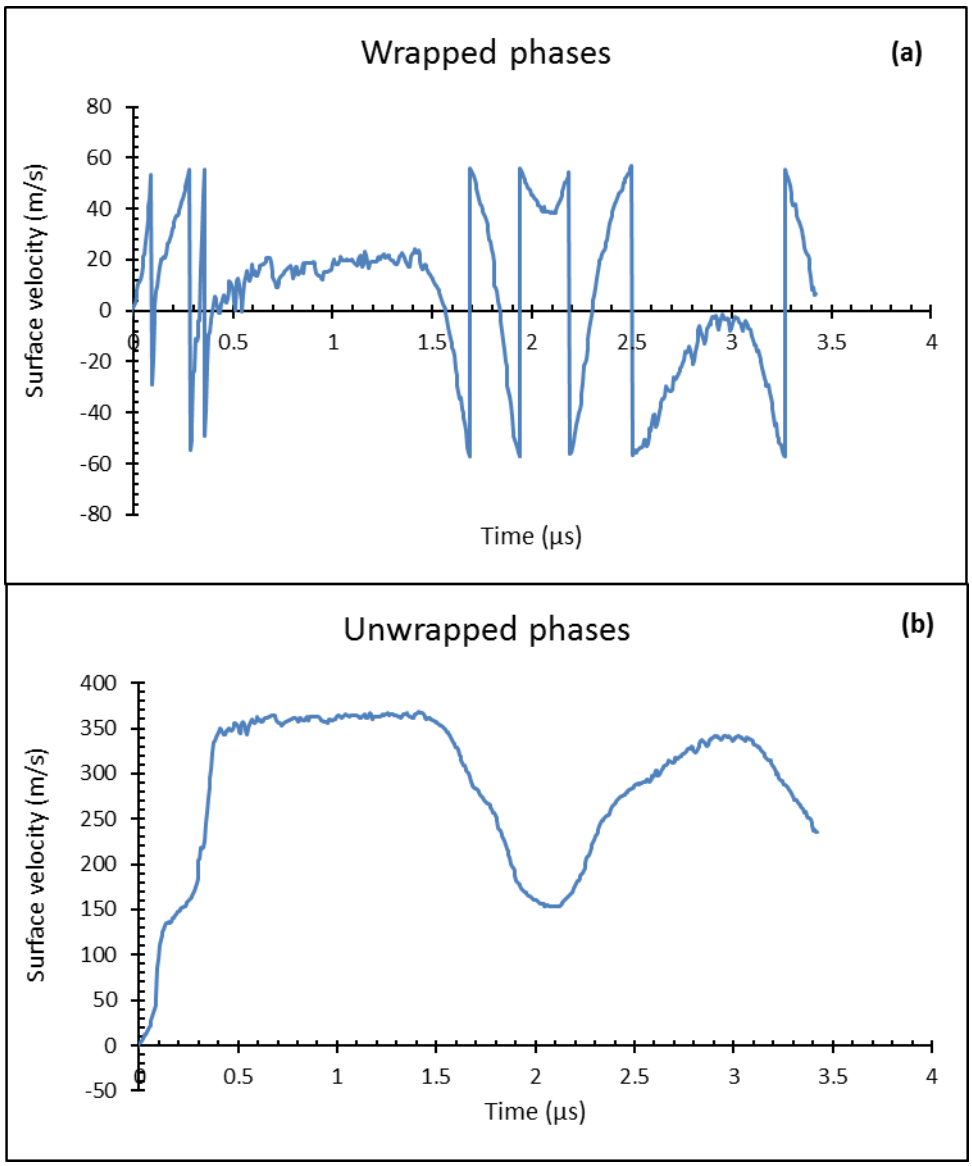

Figure 5.7: Results obtained from performing the hands-on calculations on the quadrature fringe signals extracted from the work of Amit et al (a) velocity when phases are wrapped (b) velocity after unwrapping the phases

Furthermore, the same calculations were performed on a set of fringe data shown in Figure 5.8 that was obtained during aluminium square discs experiments in the laboratory. The hands-on calculated and reduction softwave velocity curves for this data are shown in Figure 5.9. The two curves show a shift in velocity values, with the hands-on calculated velocity appearing more on the negative axis. The time on both these curves came out completely matching.

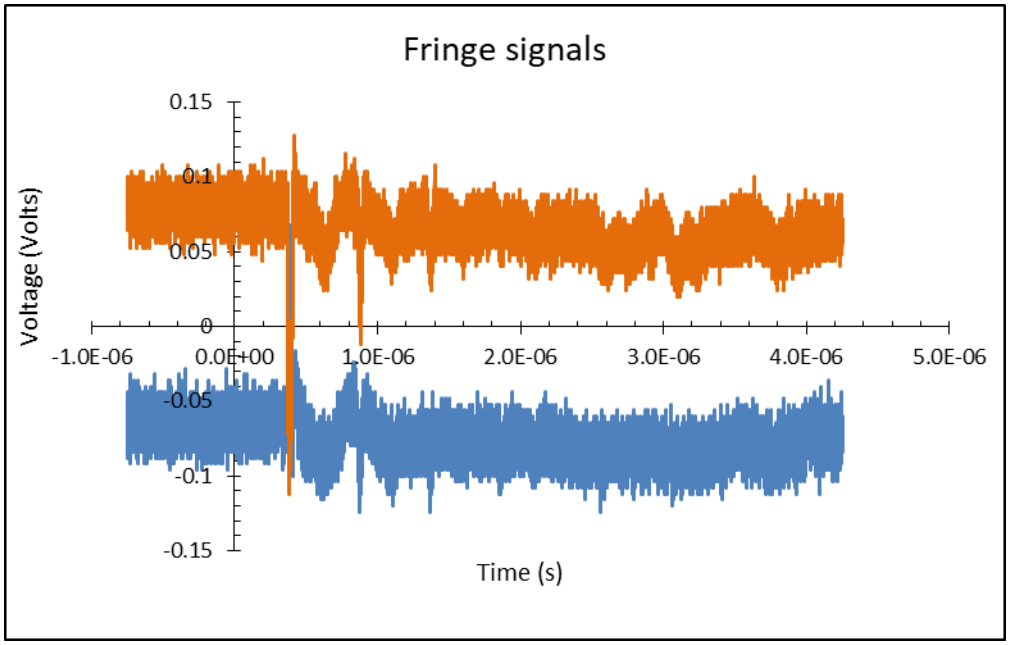

Figure 5.8: Fringe signals recorded during the aluminium discs experiment in the laser laboratory

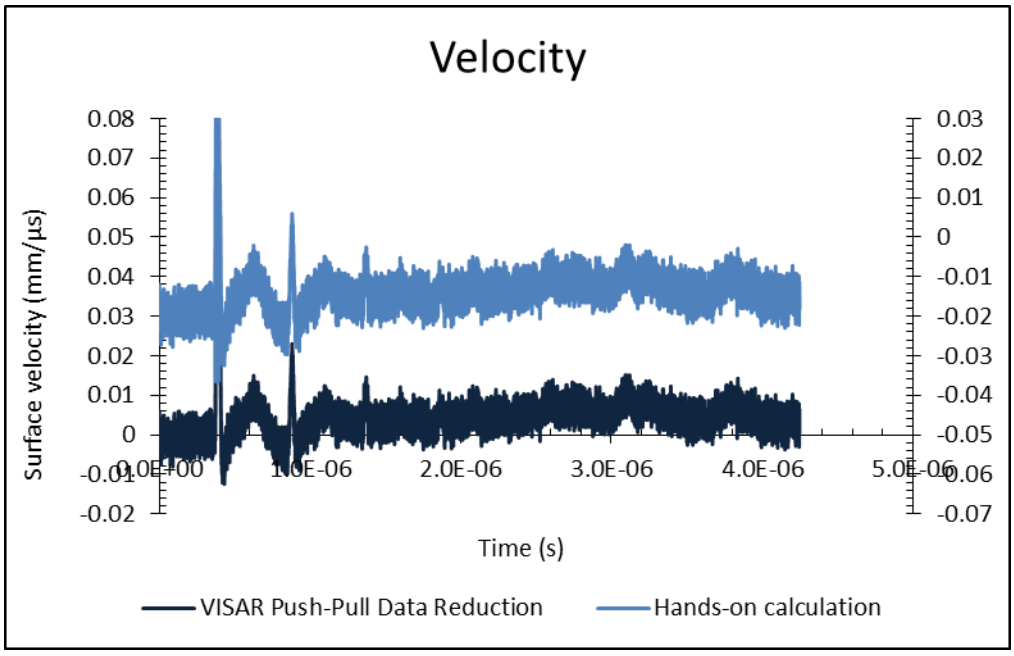

Figure 5.9: Comparison of the velocity profiles produce from aluminium discs fringe signals by VISAR Push-Pull data reduction program with results obtained by hands-on calculations

The hands-on calculation were successful on both literature work and laboratory results, and gave confidence to proceed to the square prism cylinder results. The same fringe signals in Figure 5.1 (a) were manually fitted into the mathematical equations to produce the velocity time information. The reduction program is sensitive to which signal gets loaded first. Hence,

it is cruicial to know before hand the arrangement in DATA 1 and DATA 2 signal outputs to the channels on the beam module and to the recording channels of the oscilloscope during the experiment. This means that, if DATA 1 was carrying the signal on the x-axis and DATA 2 was carrying the signal on the y-axis forming the Lissajous figure, the signal arrangement should remain the same when analysing the data on the program in order to get the results corresponding to exactly what was measured.

Similarly, it was noted that when perfoming the mathematical equations to reduce the velocity, the signal arrangement is equally important to the arrangement in the reduction program. In this case, the value of ε was determined by fitting points in the image of the Lissajous figure taken just before the shot was fired. It was noticed that the value and mostly the sign, of the quadrant on which ε lies has a huge impact on the velocity results. If the quadrature error is not precisely determined can give a totally different result from the software's. Therefore, it is best to obtain the best alignment in the VISAR and achieve a more circular Lissajous graph with minimal quadrature error.

The value of the quadrature error used by the VISAR reduction program is incorporated in the algorithm hence it is not accessible to the user. As determined from point fitting, the value of the quadrature error obtained in this study was -0.11 rad and was used in the calculation of velocity. The first velocity curve obtained from the square prism cylinder data had fringe jumps, also referred to as wrapped phases. The velocity appeared to be constrained within the same value of 0.47 mm/μs for the entire 50 μs in detonation and when this curve was zoomed

out (see Figure 5.10). Although the phase uncertainty in a Push-Pull VISAR has been reduced by the use of quadrature, however, the 2π ambiguity still remains.

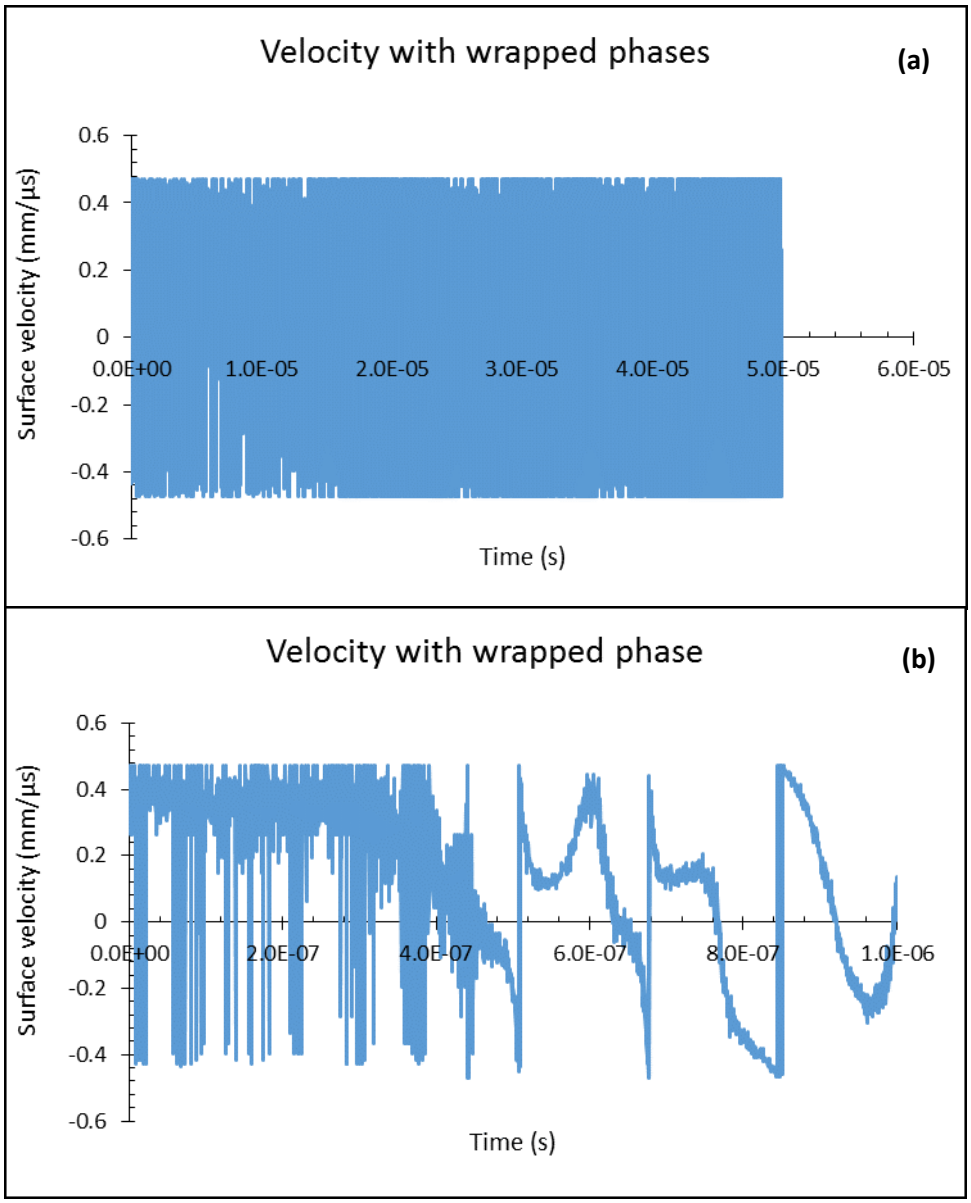

Figure 5.10: Velocity results obtained from performing hands-on calculations on the fringe signals (a) velocity in the entire period of detonation (b) velocity within the first 1.0 μs into detonation.

A tangent function was determined first from which the function of ϕ was reduced, hence, it was possible to plot the function of ϕ first and solve the wrapping problem. Literature[66] also does not really give an automated algorithim for this problem. The methods presented in literature always come down to modifying the equation to the specific requirements of your own data or one must know exactly where to add the integer of 2π next. Since there was no

common method figured out from literature that is tailored to satisfy every unwrapping problem during the analysis in this study, a semi-automated unwrapping method was formulated. The semi-automated formular was constructed in an excel spreadsheet by nested IF statements expressing that each calculated phase at time index i (ϕ_i) should be kept unchanged (ϕ_{i0}) or added – π rad (ϕ_{i-}) or π rad (ϕ_{i+}) to it and all subsequent points. ϕ_i was automatically changed to the value which was closest to the previous phase (ϕ_{i-1}).

However, the algorithm was not effective for every point in the data. By inspection it was clear that when the data was noisy, it sometimes was possible to get a 'better' result by taking the second closest value to (ϕ_{i-1}) and not the best. Since this had to be done manually this approach is "semi-automated". Figure 5.11 shows the case where the automatic algorithm worked fine for the unwrapping of phases. Figure 5.11 (a) shows the unwrapped original data, while the result of the automatic unwrapping is shown in Figure 5.11 (b).

It was mostly tricky to unfold wrapped phases that were in the noisy parts of the data such as the jumps preceding the phases that were very close to the phase jump being corrected it or if the π rad phases were following each other. Therefore, it was also necessary to go back to the graph and observe which points were jumped by the algorithm and perform the necessary corrections manually. Not all automatic corrected points were checked, only those where the second best option was close to the best option were considered. With the second best being used, there was still randomness/noise observed in the data where the jump was corrected. Figure 5.12 (a) shows an example of the automatically unwrapped data and (b) shows the same data after they were manually corrected. This type of correction occurred more in the noisy parts of the velocity results.

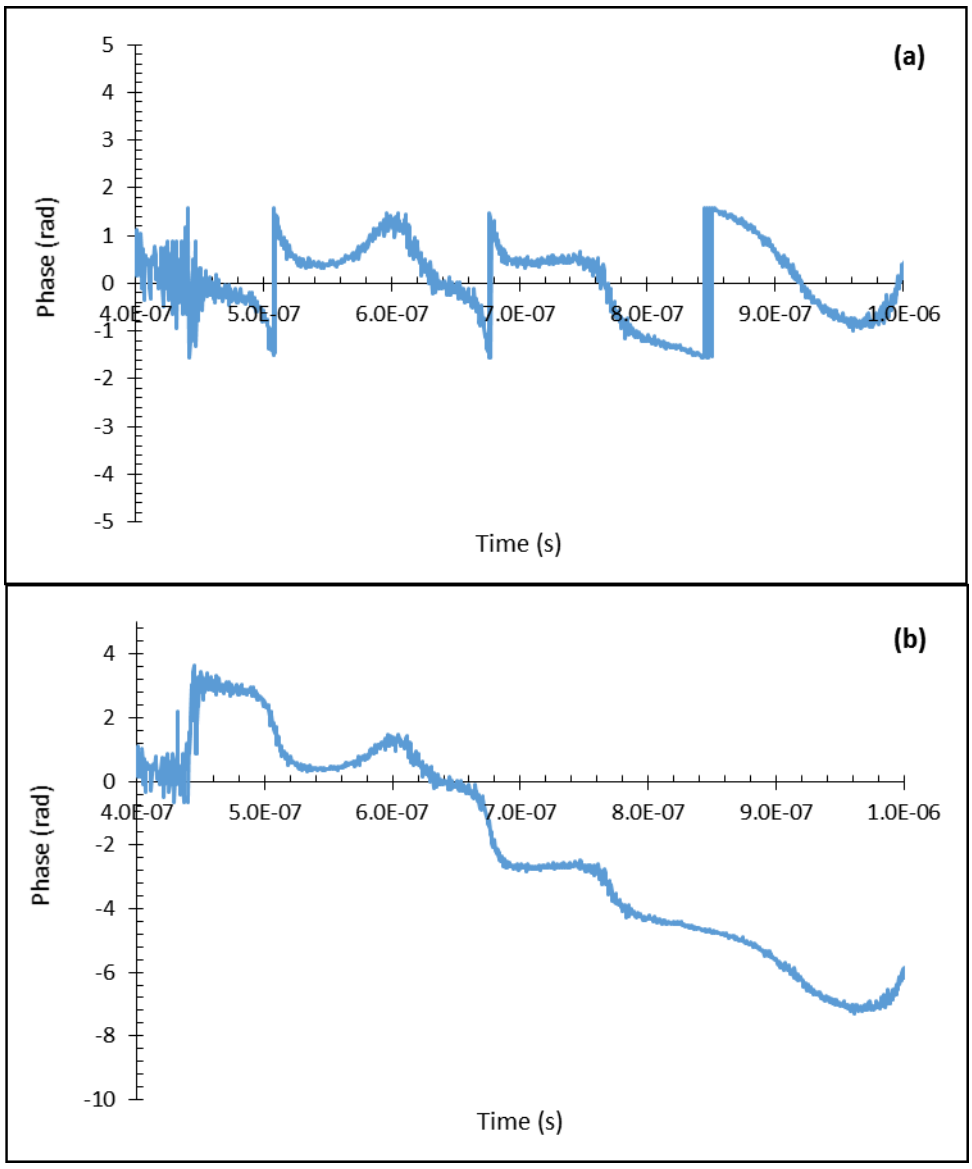

Figure 5.11: Results of the semi-automated method formulated in excel spreadsheet (a) wrapped phases (b) unwrapped phases

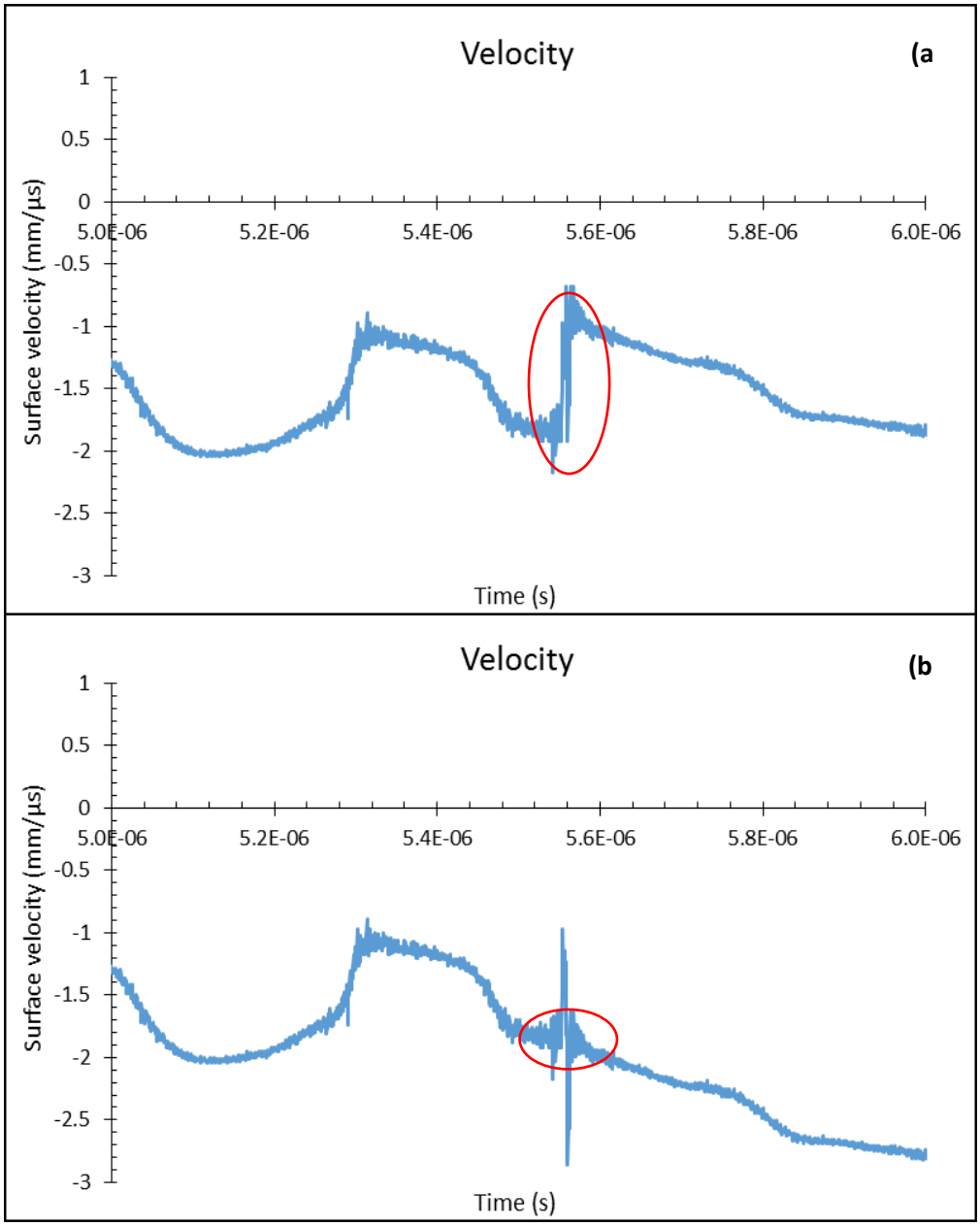

Figure 5.12: Velocity results with traces of noise in around unwrapped phases (a) wrapped phases (b) unwrapped phases or corrected jump

After completing the uwrapping exercise, velocity results were obtained formed compared to the velocity curve obtained through the reduction program (see Figure 5.13 (a)). The velocity profile obtained through hands-on calculations is low in the parts where the intensity of the signal is low. This really leaves a question mark on which algorithm works well with a low intensity noise saturated data. The trend in the two signals is similar in the first 15 µs to the curve obtained by the software but shifted in the y-axis (Figure 5.13 (b)). The process of

correcting the jumps used in this study was suspected to be intense than in the reduction hence in Figure 5.14 there are still traces of jumps in the results from the reduction program.

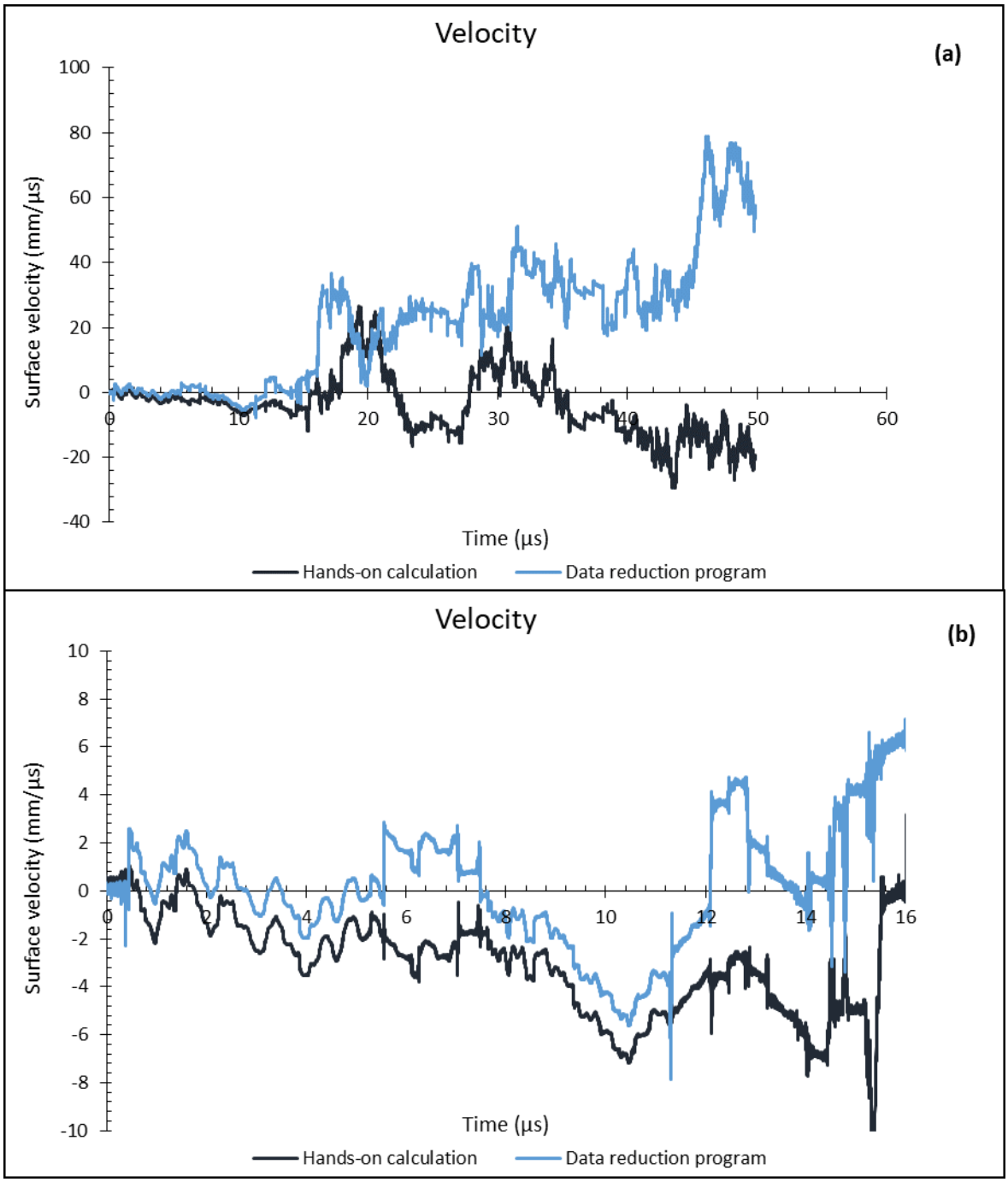

Figure 5.13: Surface velocity extracted using software and hands-on equations for the entire 50 µs

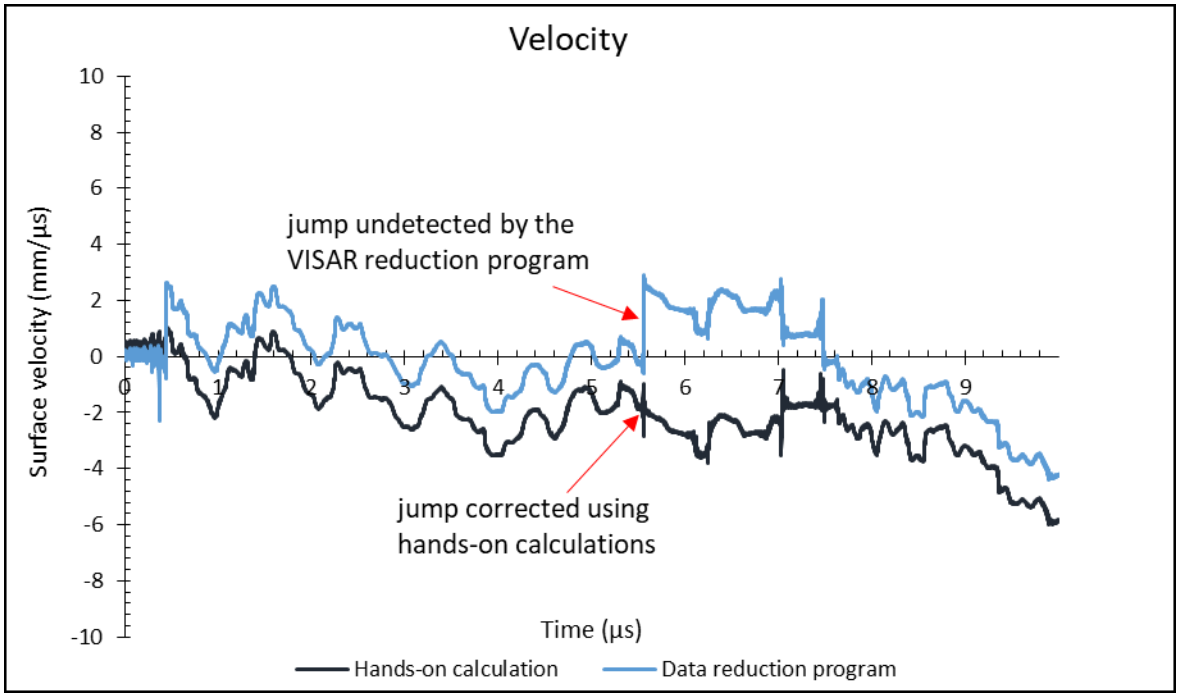

Figure 5.14: Surface velocity showing undetected jump by the reduction program and randomness over a corrected jump by hands-on calculations

The curve shown in Figure 5.15 is a repitation of Figure 5.3. It is brought again in this section to compare with the displacement curve obtained through hands-on calculations (see Figure 5.16). The hands-on calculated displacement curve shows reasonable values except it is rotated over 180 degrees compared to Figure 5.15. With the difference in the velocity results, an exact match of the two curves was not possible. The hands-on calculated displacement is reduced from a velocity curve in which fringe jumps were comprehensively corrected. As mentioned in section 5.2.1, the expansion seem like it began as early as 16 µs. However, looking at Figure 5.16, an increase began later than this time, around 29 µs which is the arrival time of the shock wave calculated in the study although the direction is opposite represents a compression instead of an expansion. Figure 5.17 shows a close-up of the two displacement curves, highlighting the difference in their initial expansion.

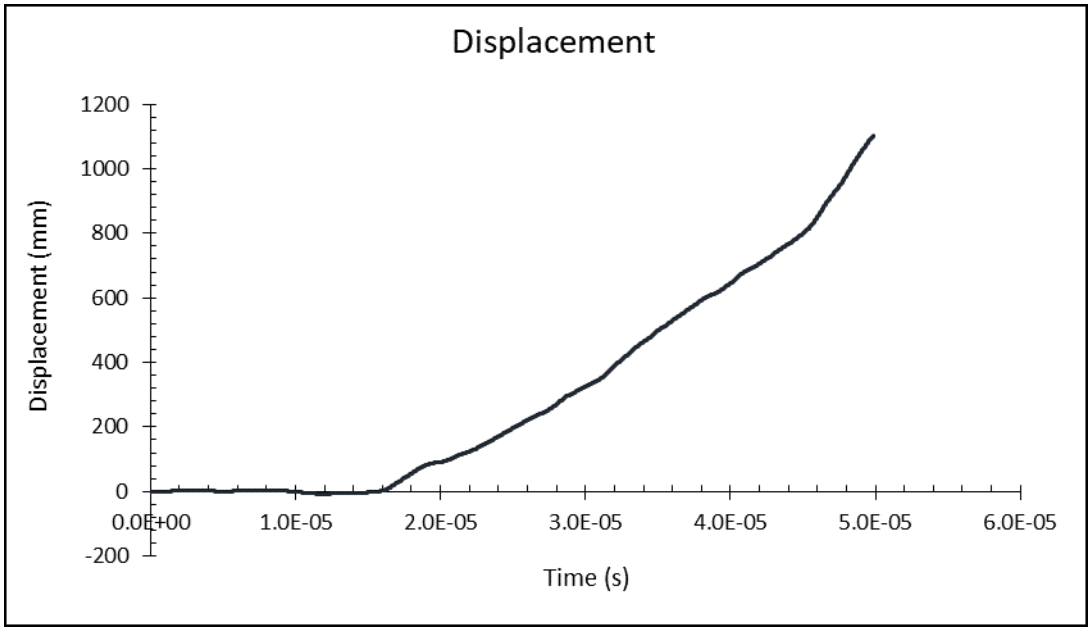

Figure 5.15: Displacement curve obtained from the reduction program

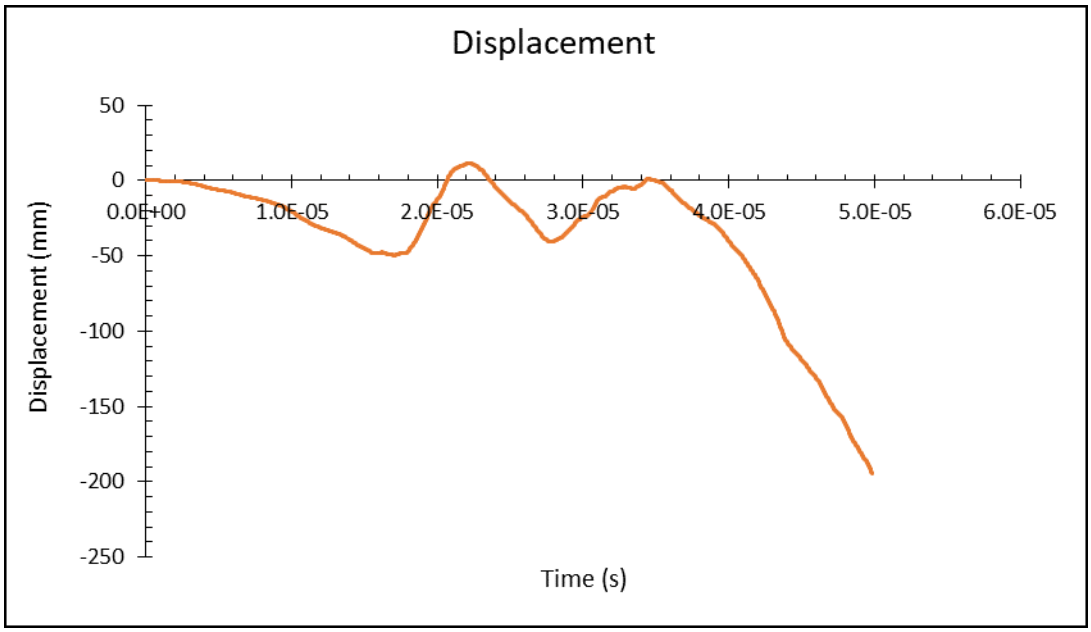

Figure 5.16: Displacement curve obtained from the hands-on calculated velocity

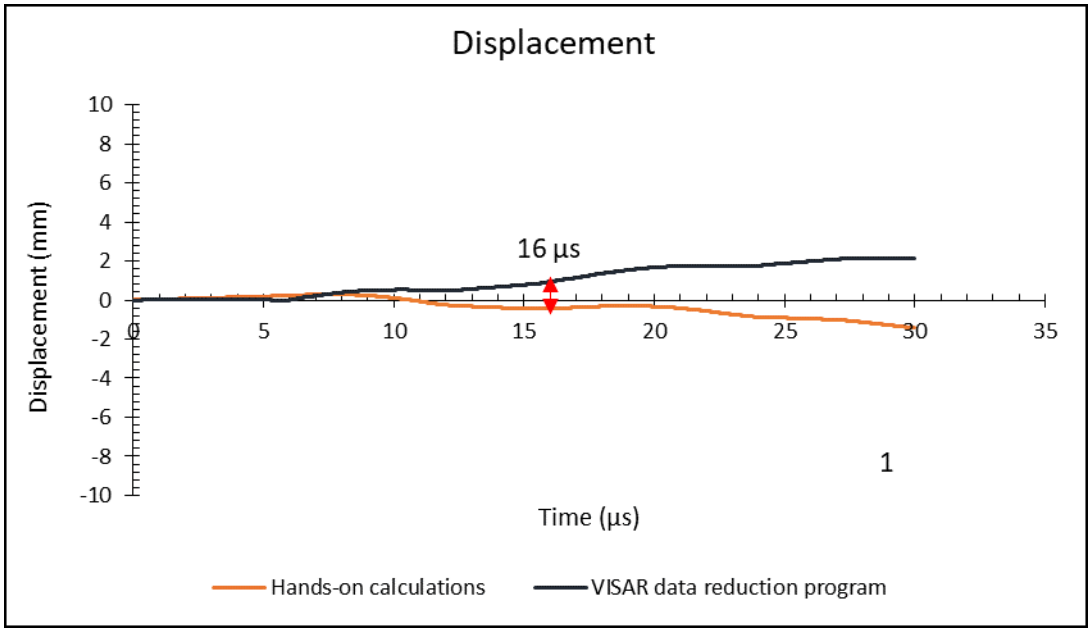

Figure 5.17: Displacement curves reduced with the two methods presented in the study both higlighting the first 16 µs after detonation

5.3. Discussion

5.3.1. Software Analysis of the Recorded Results

The set of fringe data saved from the cylinder test was analysed using the Push-Pull data reduction program. The total recording time for the cylinder test was 50 µs. As observed on the velocity graph produced by the program, meaningful results extracted from the fringe information seem to be in the first 16 µs only (see Figure 5.1) and the velocity beyond this time is extremely high to be significant for this test. The results do not explain the reaction starting at very high pressure which decrease and eventually dies as the shock wave losses its energy as it appears on the UHSC images of the standard cylinder expansion test. The profile also does not show a constant velocity towards the completion of the detonation event. Normally, at about 48 µs the velocity is expected to be constant[67], but in our case it is showed an increase. The velocity values of the test were found to be extremely high and very difficult to explain. Hence, this velocity profile was not expected and difficult to draw conclusions.

Although the geometry of the cylinder tube (square prism) utilized in the study was different from the standard cylinder used to perform a cylinder expansion test ; its extrusion which confined comp B charge was cylindrical. Hence, the behaviour during expansion was expected to be more or less the same as the behaviour of a cylindrical tube as seen in Figure 5.13. It was also noted that the differences in the results of the two tubes (cylinder and square prism) were bound to be present because of the variation in their wall thicknesses which imply varying

strengths in their structures. The standard cylindrical tube has a uniform wall thickness whereas the square prism is thicker on the corners and thinner on the sides. Images taken post test show signs of rupture of the square prism. A trace of the square prism wall was observed on the "vlip", as shown in Figure 5.18. Therefore, as much as similar results to the standard cylinder were hoped for in a square prism expansion, their geometries did not behave the same under detonation hence there are variations in the expansion results. It is also uncertain when the rupture occurred during the event.

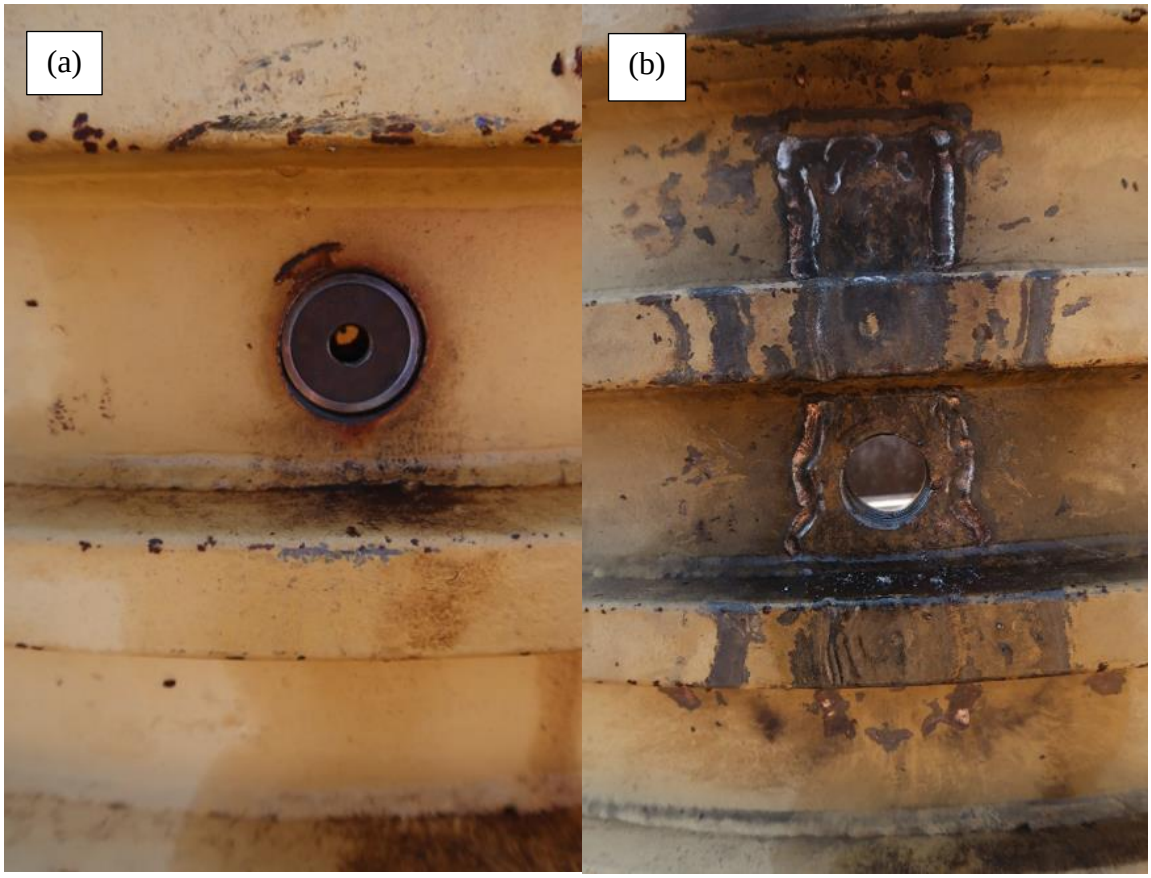

Figure 5.18: (a) "vlip" wall before the shot (b) Traces of the ruptured cylinder on the "vlip" wall after the shot

5.3.2. Hands-on Analysis of the recorded data

Amit et al's data fitted well into the hands-on equations. The velocity-time profile in Figure 5.7 correspond very well with the published graph. The only difference between the two data sets was the maximum value of the velocity. The unwrapping in Amit et al's data set was quite easy because of the few points extracted. The data set from aluminium discs experiment did not require any phase unwrapping, the 2π ambiguity was not applicable. The initial surface velocity curve from the reduction program is almost zero while hands-on calculations show a

small offset velocity. But the two graphs have exactly the same features. As it is evident from Figure 5.16, the displacement graph reduced by hands-on calculations give more realistic velocity values, except they are negative. The recorded changes of the cylinder surface are within 150 mm working distance between the optical probe and cylinder. Furthermore, the continuous increase is observed at almost approximately 30 μs which was calculated as the arrival time of the shock wave where the probe was observing. A fine structure is also observed in the velocity curve (see Figure 5.13), which implies that the jump correction algorithm was effective although it became quite difficult where the signal to noise ratio (SNR) was low.

Factors that may have affected the expansion of the cylinder are as follows:

- Firstly, as mentioned in section 4.6 sunlight glare had a tremendous effect on the setup. Although the sole purpose of UNBP filter in the VISAR module is to minimise the white "self light" collected with the green 532 nm light from the cylinder, this experiment had too much sunlight glare. Hence, the 40% of the 532 nm light that was allowed to pass through the filter, according to the manufacturer, could have been a fraction of an already small percent collected from the cylinder. For this reason the Lissajous for this experiment symbolised a very small amount of light signal collected to the VISAR module because it was too tiny. This size was last observed before leaving the room for the safety of our ears from the explosion noise during the firing of the shot. During the countdown to the shot, there was no mechanism set to observe what happened to the already achieved Lissajous graph.
- Since the booster and detonator were already put over the cylinder, we took the risk and went on to detonate with that small signal. Hence, this lack of optimization of the VISAR system during our test may have affected its accuracy.
- Another factor could be the use of an inappropriate etalon; we may have added to or subtracted from the time delay required for the cylinder test. An inaccuracy in required delay time may result in some or most of the data in a fast event to be lost [15].
- The BNC cables that were used to connect the beam module to the recording oscilloscopes were long, 50 Ω extended to another of unknown impedance. This implies that there is a possibility that there was impedance mismatch of the cables. Therefore it is highly possible that there were reflections that resulted in power loss or bad signal.
- Also, there were a number of human errors on site as the VISAR instrumented test was done for the first time at DBEL testing range. The fact that it worked the first time and

one shot was done, it is clear that it can be taken to the test range again for the cylinder tests that will have improved setup and components such as stand design.

All the factors mentioned above had an effect mainly in the intensity of the laser light carrying the information about the behaviour of the cylinder wall. However, the fact that the test did not produce expected results does not despise the advantages of using the VISAR during a cylinder expansion test. The cylinder expansion test instrumented with the VISAR has less costs compared to the one instrumented with a Cordin UHSC. Firstly, the Cordin UHSC time resolution is not as high as the VISAR's. The Cordin UHSC requires more gas for every test planned. The higher the frame rate, the faster it depletes the gas. The gas used is a balloon grade helium which much expensive per tank because of its lower 99.99% purity. The VISAR can be used for a couple of years with the same PMTs and produces data points more than the UHSC. Unlike the VISAR which is portable, the Cordin camera is quite special, it can only be operated where it is installed.

Chapter 6

Conclusion and recommendations

6.1. Conclusion

A cylinder expansion test with a square prism tube as target, instrumented with a VISAR system was carried out. This confirmed that, despite certain difficulties the VISAR system can be used at DBEL testing range, although this study did not prove the accuracy and flexibility of the system in such an environment. Due to the unrealistic velocity values, the interpretation of the results was not ideal and the results were inconclusive. Nonetheless, the analysis provided in this study will be invaluable in the design and execution of future VISAR test.

More than one method was used to retrieved the velocity information from fringe data; using the data reduction program, also hands-on calculations were used to obtain velocity information from fringe data on three sets of data; (1) data from literature by Amit[64], (2) aluminium square discs experiment and (3) data obtained from the square prism cylinder. The hands-on calculations were successful in all three data sets. The process of solving the the fringe jumps or in other terms wrapped phases was a challenge. A semi-automated unwrapping method was accomplished and used in performing the calculations. The unwrapping of the phases resulted in some profile although it is difficult to be confident, because of the low SNR values.

It is however clear that the technique is sensitive to events happening at very shot time scales. It is of importance to mention that understanding the two approaches of analysing the fringe data was quite a success and huge achievement in this study. However, due to the uncertainties of the square prism cylinder velocity results further processing of the results to obtain the JWL EOS parameters could not be carried out as planned for later. A new experiment has to be conducted to achieve better SNR that makes certain and that could result into correct velocity history of the cylinder. This also means that if the test fails in having high intensity, one has to come up with an optimal process of correcting the fringe jumps.

6.2. Recommendations

Based on the experiences from this work, the following recommendations are made:

i. The cylinder expansion test instrumented with a VISAR must be conducted under the shade. Since DBEL testing range operates during the day while the sun is still up, it is highly recommended that an object covering the optical probe-cylinder setup be designed.

ii. A proper design of the cylinder holder that is firmly fixed on the table to avoid the misalignment during the insertion of the detonator. The holder must be able to hold the cylinder at the bottom and at the top, mm away from the booster and must not interfere with the expansion of the wall.

iii. A camera setup that will enable the person aligning the cylinder with the incoming beam to see the light intensity changes on the viewing screens in the VISAR module.

iv. A camera setup that will enable the explosive engineer to be able to see any changes happening to the Lissajous as he/she gets ready to detonate the cylinder.

v. A delay generator must be connected to the recording oscilloscope to set and achieve meaningful time scales.

vi. A signal conditioner or voltage regulator that can keep the VISAR system and recording oscilloscopes running for a minimum of 20 minutes must be connected to the setup to allow enough time for backup generator to be connected in cases of power failure and to avoid voltage spikes affecting the VISAR system.

vii. The BIM must be connected to the VISAR to monitor any self-light entering the VISAR module. Through this signal, the variations occurring in the average light intensity would be observed.

viii. The BNC cables used for connecting the VISAR beam module with the recording oscilloscopes must be short, about 1 m long. This create a short path travelled by the signal and therefore avoides incidents such as delayed trigger.

References

1. Council, N. R. Countering the Threat of Improvised Explosive Devices: Basic Research Opportunities. *The National Academies Press* 20 (2007). doi:10.17226/11953

2. Wilkinson, E., Turns, D., McAteer, D., Johnson, S. & Cleary, L. Written evidence into the use of Improvised Explosive Devices and their impact on the Humanitarian Space. Report to the All Party Parliamentary Group (APPG) on Explosive Weapons. (2017).

3. The Aid Worker Security Database: Location of attacks (1997 - 2017). **2019**,

4. The Aid Worker Security Database: Trends in tactics (1997 - 2017). **2019**,

5. Snyman, I. M. & Olivier, M. Using an ultra-high speed camera to capture a tube expansion test. (2016).

6. Peter, X., Jiba, Z., Snyman, I. M. & Mostert, F J Sono, T. J. Prediction of Detonation and JWL EOS Parameters of Energetic Materials using EXPLO5 Computer Code. (2016).

7. Elek, P. M., Dzingalasevic, V. V, Jaramaz, S. S. & Mickovic, D. M. Determination of detonation products equation of state from cylinder test: Analytical model and numerical analysis. *Therm. Sci.* **19**, 35–48 (2015).

8. Chen, C. ., Shiuan, J. H. & Lan, I. F. The Equation of State of Detonation Products obtained from cylinder expansion test. *Propellants, Explos. Pyrotech.* **19**, 9–14 (1994).

9. Hornberg, H. Determination of Fume State Parameters from Expansion Measurements of Metal Tubes. *Propellants, Explos. Pyrotech.* **11**, 23–31 (1986).

10. Lan, I. F., Hung, S. C., Chen, C. Y., Niu, Y. M. & Shiuan, J. H. An Improved Simple Method of Deducing JWL Parameters from cylinder expansion test. *Propellants, Explos. Pyrotech.* **18**, 18–24 (1993).

11. Volk, H. & Hornberg, F. The cylinder test in the context of physical detonation measurement methods. *Propellants, Explos. Pyrotech.* **14**, 199–211 (1989).

12. Hansson, H. *Determination of properties for emulsion explosives using cylinder expansion tests and numerical simulation*. (Swedish Blasting Research Centre och Lule tekniska universitet, 2009).

13. Mostert, F. J. Copper Cylinder Expansion Tests for NTO/TNT Based Explosive Charge Mixture. 1–32 (2015).

14. Dolan, D. H. *Foundations of VISAR analysis*. (2006). doi:10.2172/886901

15. Fleming, K. J. & Broyles, T. A. *Shock Analysis Using The Multi Point Velocimeter (VISAR)*. (2003).

16. Hereil, P. L., Loupias, C. & Bergues, D. European Forum on Ballistics of Projectiles. in 511–515 (2000).

17. Menikoff, R., Scovel, C. A. & Shaw, M. S. Cylinder Test Wall Velocity: Experimental and Simulated Data. *Cylind. test wall Veloc. Exp. simulated data* (2013).

18. Hodgson, A. N. & Handley, C. A. DSD/WBL-consistent JWL equations of state for EDC35. in *AIP Conference Proceedings* **1426**, 247–250 (AIP, 2012).

19. Jackson, S. I. An analytic method for two-dimensional wall motion and product isentrope from the detonation cylinder test. *Proc. Combust. Inst.* **35**, 1–8 (2014).

20. Hill, L. G. Detonation Product Equation-Of-State Directly from the Cylinder Test. *Off. Sci. Tech. Inf. U.S Dep. Energy* 1–9 (1997).

21. Polk, F. *Determination of the Equation of State of Explosive Detonation Products from the Cylinder Expansion Test*. (1984).

22. Souers, P. C. & Vitello, P. A. *Detonation Energy Densities from the Cylinder Test*. (2015).

23. Sutton, B. D., Ferguson, J. W. & Hodgson, A. N. An analytical approach to obtaining JWL parameters from cylinder tests. in *AIP Conference Proceedings* **1793**, 30032 (AIP Publishing, 2017).

24. Kerley, G. I. & Christian-Frear, T. L. *Prediction of explosive cylinder tests using equations of state from the PANDA code*. (1993).

25. Kunzel, M., Selesovsky, J. & Pachman, J. First attempts in cylinder expansion testing. *New Trends Res. Energ. Mater.* 1–7 (2017).

26. Elek, P. D. V & Jaramaz, S. M. D. Cylinder test: Analytical and numerical modeling. *A A* **1**, 2 (2011).

27. Vogler, T. J. *et al.* Using the line-VISAR to study multi-dimensional and mesoscale impact phenomena. *Int. J. Impact Eng.* **35**, 1844–1852 (2008).

28. Meyer, R., Kohler, J. & Homburg, A. *Explosives*. (Wiley. VCH Verlag GmbH & Co. KGaA, 2007).

29. Souers, P. C., Wu, B. & Haselman, L. C. J. *Detonation Equation of State at LLNL, 1995*. (1995).

30. Souers, P. C. & Kury, J. W. Comparison of Cylinder Data and Code Calculations for Homogeneous Explosives. 1–9 (1993).

31. Sućeska, M. Evaluation of Detonation Energy from EXPLO5 Computer Code Results. *Propellants, Explos. Pyrotech.* **24**, 280–285 (1999).

32. Peter, X. & Snyman, I. M. Determination of JWL Parameters of TNT, Composition B and NTO/TNT from the Expansion Data of the Cylinder Test. 1–55 (2016).

33. Hill, L. G., Mier, R. & Briggs, M. E. PBX 9404 Detonation Copper Cylinder Tests: A Comparison of New Aged Material. *AIP Conf. Proc.* 1–5 (2009).

34. Cooper, W. P. & Kurowski, S. R. *Introduction to Technology of Explosives*. (WILEY VCH, 1996).

35. Urtiew, P. A. & Hayes, B. Parametric study of the dynamic JWL-EOS for detonation products. *Combust. Explos. Shock Waves* **27**, 505–514 (1991).

36. Lee, E. L., Hornig, H. C. & Kury, J. W. Adiabatic Expansion of High Explosive *Adiabatic expansion of high explosive detonation products* (1968).

37. Jones, H. & Miller, A. R. The Detonation of Solid Explosives; The Equilibrium Conditions in the Wave-front and the Adiabatic Expansion of the Products of Detonation. *R. Soc. London Publ.* **194**, 480–507 (1948).

38. Lee, E. L., Hornig, H. C. & Kury, J. W. ADIABATIC EXPANSION OF HIGH EXPLOSIVE DETONATION PRODUCTS. *Adiabatic Expans. high Explos. detonation Prod.* (1968).

39. Barker, E. L., Murphy, D., Stiel, L. I. & Wrobel, E. Theory and calibration of JWL and JWLB thermodynamic equation of state. *WIT Trans. State Art Sci. Eng.* **60**, 12 (2010).

40. Valyn VIP Inc. *A/V A to Z: An Encyclopedic Dictionary of Media, Entertainment and Other Audiovisual Terms* (2014).

41. Souers, P. C. & Vitello, P. A. *Detonation Energy Densities from the Cylinder Test*. (2015).

42. Durand, M. *et al.* Interferometric laser technique for accurate velocity measurements in shock wave physics. *AIP Rev. Sci. Instruments* **48**, 5 (1977).

43. Krauter, K. G., Jacobson, G. F., Patterson, J. R., Nguyen, J. H. & Ambrose, W. P. Single-mode fiber, velocity interferometry. *US Libr. Med. Natl. Inst. Heal. Sci. Instruments* **82**, 16 (2011).

44. Barker, L. M. & Hollenbach, R. E. Laser interferometer for measuring high velocities of any reflecting surface. *Appl. Phys.* **43**, 1–8 (1972).

45. Rao, Y. J. & Jackson, D. A. Principles of Fiber-Optic Interferometry. in 1–2 (Springer, 2000).

46. Kuznetsov Valerian A., B. S. P. *Development of Photon Doppler Velocimeter for Explosives Research*. (2013).

47. Strand, O. T. *et al.* Velocimetry Using Heterodyne Techniques. *Present. Velocim. Using Heterodyne Tech. Alexandria, VA, United States, Sep 20 - Sep 23, 2004* **5580**, 593–600 (2005).

48. Frank, L. P. Optical Interferometry. in 215–217 (Person Addison Wesley, 2006).

49. Monzon, J. J. & Sanchez-Soto, L. L. Amplitude response of a Fabry-Perot interferometer. European Journal of Physics (2015).

50. McMillan, C. F. *et al.* Velocity of fast surfaces using Fabry-perot interferometry. *AIP Rev. Sci. Instruments* **59**, 22 (1988).

51. Strand, O. T., Goosman, D. R., Martinez, C., Whitworth, T. L. & Kuhlow, W. W. Compact system for high-speed velocimetry using heterodyne techniques. *AIP Rev. Sci. Instruments* **77**, 9 (2006).

52. Ao, T. & Dolan, D. H. *SIRHEN : a data reduction program for photonic Doppler velocimetry measurements*. (2010). doi:10.2172/989357

53. Sargis, P. D., Molau, N. E., Sweider, D., Lowry, M. E. & Strand, O. T. Photonic doppler velocimetry. *United States* 1–6 (1999).

54. Briggs, M., Hill, L. G., Hull, L. M., Shinas, M. A. & Dolan, D. H. Applications and principles of photon-Doppler velocimetry for explosive testing. in *Proceedings of 14th International Detonation Symposium* (2010).

55. Barker, L. M. VISAR vs PDV. *Valyn Int.* (1976).

56. Jensen, B. J., Holtkamp, D. B., Rigg, P. A. & Dolan, D. H. Accuracy limits and

window corrections for Photon Doppler Velocimetry. *AIP Rev. Sci. Instruments* **101**, 11 (2007).

57. Joshi, K. D., Rav, A. S. & Gupta, S. C. *Development velocity Interferometer system for any reflector for measurement of mechanical properties of materials during high strain-rate compression and decompression process*. (2011).

58. Hemsing, W. F. Velocity sensing interferometer (VISAR) modification. **50**, 1–7 (1979).

59. Hongliang, He Takamichi, K. & Sekine, T. Accurate measurements of the velocity history of a laser-driven foil plate with a push-pull-type VISAR. **40**, 6327–6333 (2001).

60. Li, Z., Ma, R., Chen, G., Liu, J. & Yao, J. Multipoint velocity interferometer system for any reflector. *Rev. Sci. Instrum.* **70**, 3872–3876 (1999).

61. Barker, L. M. *VALYN VISARS USER`S HANDBOOK*. (2009).

62. Resnyansky, A. D., Weckert, S. A., Foord, A. & Skibinski, C. Establishment of a VISAR Measurement System for Material Model Validation in DSTO. *Establ. a VISAR Meas. Syst. Mater. Model Valid. DSTO* (2013).

63. Rav, A., Joshi, K. D., Singh, K. & Kaushik, T. C. Characterization of Signal Recording System for accurate velocity estimation using VISAR. (Bhabha Atomic Research Centre, 2018).

64. Rav, A., Joshi, K. D., Singh, K. & Kaushik, T. C. Characterization of a signal recording system for accurate velocity estimation using a VISAR. *Meas. Sci. Technol.* **29**, 25205 (2018).

65. Thunyiswa, N. Copper Cylinder Expansion Tests for Comp B Explosive Charge with VISAR as the expansion measurement instrument. 34 (2018).

66. Kazuyoshi, I. Analysis of the phase unwrapping algorithm. *Appl. Opt.* **21**, 1 (1982).

67. Jackson, S. I. Scaled Cylinder Test Experiments with Insensitive PBX 9502 Explosive. in *15th International Symposium on Detonation* 10 (2014).